DTIC® DEFENSE TECHNICAL INFORMATION CENTER

Information for the Defense Community

DTIC® has determined on 1/12/2010 that this Technical Document has the Distribution Statement checked below. The current distribution for this document can be found in the DTIC® Technical Report Database.

☒ **DISTRIBUTION STATEMENT A.** Approved for public release; distribution is unlimited.

☐ **© COPYRIGHTED**; U.S. Government or Federal Rights License. All other rights and uses except those permitted by copyright law are reserved by the copyright owner.

☐ **DISTRIBUTION STATEMENT B.** Distribution authorized to U.S. Government agencies only (fill in reason) (date of determination). Other requests for this document shall be referred to (insert controlling DoD office)

☐ **DISTRIBUTION STATEMENT C.** Distribution authorized to U.S. Government Agencies and their contractors (fill in reason) (date of determination). Other requests for this document shall be referred to (insert controlling DoD office)

☐ **DISTRIBUTION STATEMENT D.** Distribution authorized to the Department of Defense and U.S. DoD contractors only (fill in reason) (date of determination). Other requests shall be referred to (insert controlling DoD office).

☐ **DISTRIBUTION STATEMENT E.** Distribution authorized to DoD Components only (fill in reason) (date of determination). Other requests shall be referred to (insert controlling DoD office).

☐ **DISTRIBUTION STATEMENT F.** Further dissemination only as directed by (inserting controlling DoD office) (date of determination) or higher DoD authority.

Distribution Statement F is also used when a document does not contain a distribution statement and no distribution statement can be determined.

☐ **DISTRIBUTION STATEMENT X.** Distribution authorized to U.S. Government Agencies and private individuals or enterprises eligible to obtain export-controlled technical data in accordance with DoDD 5230.25; (date of determination). DoD Controlling Office is (insert controlling DoD office).

UNIVERSITY OF CALIFORNIA

Los Angeles

Neutralization of Bacterial Aerosols by Aerodynamic Shocks in a Novel Impactor System: An Integrated Computational and Experimental Study

Final Technical Report

HDTRA1-07-1-0012

by

Patrick R. Sislian

and

Panagiotis D. Christofides

October 15, 2010

REPORT DOCUMENTATION PAGE

Form Approved
OMB No. 0704-0188

1. REPORT DATE *(DD-MM-YYYY)*
10/15/2010

2. REPORT TYPE
Final Technical Report

3. DATES COVERED *(From - To)*
Jan. 2007 - Oct. 2010

4. TITLE AND SUBTITLE
Neutralization of Bacterial Aerosols by Aerodynamic Shocks in a Novel Impactor System: An Integrated Computational and Experimental Study

5a. CONTRACT NUMBER

5b. GRANT NUMBER
HDTRA1-07-1-0012

5c. PROGRAM ELEMENT NUMBER

6. AUTHOR(S)
Patrick Sislian and Panagiotis D. Christofides

5d. PROJECT NUMBER

5e. TASK NUMBER

5f. WORK UNIT NUMBER

7. PERFORMING ORGANIZATION NAME(S) AND ADDRESS(ES)
University of California, Los Angeles
UCLA Office of Contract & Grant Admin
10920 Wilshire Blvd. Suite 1200
Los Angeles, CA 90024-1406

8. PERFORMING ORGANIZATION REPORT NUMBER

9. SPONSORING/MONITORING AGENCY NAME(S) AND ADDRESS(ES)
DTRA/BE-BCR
8725 John J. Kingman Road
MSC 6201
Fort Belvoir, VA 22060-6201

10. SPONSOR/MONITOR'S ACRONYM(S)

11. SPONSORING/MONITORING AGENCY REPORT NUMBER

12. DISTRIBUTION AVAILABILITY STATEMENT

13. SUPPLEMENTARY NOTES

14. ABSTRACT

Neutralization of bacterial aerosol releases is critical in countering bioterrorism. We investigate the mechanical instabilities of the bacterial cell envelope as the bacteria pass through aerodynamic shocks. To carry out this fundamental investigation, a novel experimental impactor system is built to simultaneously create a controlled shock and to collect the bacteria after they pass through the shock. Experimental measurements of the pressure in the impactor system compare well with computational fluid dynamics simulations used to characterize the aerodynamic shocks.The bacteria experience relative deceleration because of sharp velocity changes in the aerodynamic shock created in the impactor system. Computational model results indicate that vegetative E. coli cells require a critical acceleration of 3.0x10^8 m/s^2 compared to 3.9-16x10^9 m/s^2 for B. atropheus spores to breakup. Computed accelerations in the impactor system reach 5.9x10^9 m/s^2 which predict breakup of both vegetative cells and spores. Experimentally, aerosolized E. coli cells and B. atropheus spores that pass through aerodynamic shocks created in the experimental impactor system are an order of magnitude less likely to retain viability than those that pass through the impactor at conditions which do not lead to the generation of an aerodynamic shock.

15. SUBJECT TERMS

Bacterial aerosol, airborne bacteria, aerodynamic shocks, impactor, computational modeling, bacterial break-up, particle motion, aerosol sampling, aerosol collection, collection efficiency

16. SECURITY CLASSIFICATION OF:
a. REPORT U
b. ABSTRACT U
c. THIS PAGE U

17. LIMITATION OF ABSTRACT
UU

18. NUMBER OF PAGES

19a. NAME OF RESPONSIBLE PERSON
Panagiotis D. Christofides

19b. TELEPONE NUMBER ***(Include area code)***
310-794-1015

Standard Form 298 (Rev. 8-98)
Prescribed by ANSI-Std Z39-18

Chapter 1

Executive Summary

1.1 Significant Contributions

Neutralization of bacterial aerosol releases is critical in countering bioterrorism. As a possible bacterial aerosol neutralization method that avoids the use of chemicals, we investigate the mechanical instabilities of the bacterial cell envelope in air as the bacteria pass through aerodynamic shocks. To carry out this fundamental investigation, a novel experimental impactor system is designed and built to simultaneously create a controlled and measured shock and to collect the bacteria after they pass through the shock. In the impactor system, the aerosol flows through a converging nozzle, perpendicular to a collection surface that has an orifice through which the shocked bacteria enter a deceleration tube. Both experimental measurements of the pressure in the impactor system at multiple points and computational fluid dynamics simulations are used to characterize quantitatively the shocks created in the impactor. Specifically, the developed computational model describes the evolution of both the gas and particle velocity and temperature in the impactor system to determine the forces exerted on the bacterial aerosol as they pass through the shock. The results indicate that the developed computational model predictions compare well with the experimental pressure measurements.

The bacteria experience relative deceleration because of sharp velocity changes in the aerodynamic shock created in the experimental impactor system. Computational model results indicate that vegetative *E. coli* cells require a critical acceleration of 3.0×10^8 m/s^2 compared to $3.9 - 16 \times 10^9$ m/s^2 for *B. atropheus* spores to break-up. Computed accelerations in the impactor system reach 5.9×10^9 m/s^2 which predict break-up of both vegetative cells and spores. Experimental findings demonstrate that aerosolized *E. coli* cells and *B. atropheus* spores that pass through aerodynamic shocks created in the experimental impactor system are an order of magnitude less likely to retain viability than those that pass through the impactor at conditions which do not lead to the generation of an aerodynamic shock, and therefore, do not reach the critical acceleration required for break-up. However, *B. atropheus* spores that do not break-up have a higher likelihood to remain live compared to *E. coli*.

The novel impactor system is introduced in Chapter 2 of Appendix A. Specifically, the advantages of using the impactor system are highlighted in relation to studying the effects of aerodynamic shocks: simultaneous collection and control of

Contents

shock strength. The gas dynamics of the impactor system is studied with both experimental measurements and computational model simulations. The Mach number of the aerodynamic shock is shown to be a function of the operating conditions as well as the geometry of the impactor. The experimental measurements verify the computational gas dynamics model which is used in Chapter 3 of Appedix A.

Chapter 3 of Appendix A explores the motion of the bacteria as they travel through the impactor system: specifically, the deceleration forces that act on the bacteria as they passe through the aerodynamic shock. These forces are computed for the different geometries and operating conditions of the impactor system and are compared to the Rayleigh-Taylor break-up model. Knowing the critical Rayleigh-Taylor accelerations needed to break-up a cell and the decelerations achieved in the impactor system, we are able to make predictions on which cells survive.

In Chapter 4 of Appendix A, the predictions obtained from the previous chapters are tested by passing aerosolized *E. coli* vegetative cells through the experimental impactor system. Furthermore, a stochastic random walk model is used to determine the collection efficiency at different experimental operating conditions. The model developed in Chapter 3 of Appendix A is confirmed with the experimental viability measurements obtained using a fluorescence flow cytometer.

Chapter 5 of Appendix A provides more experimental data to confirm the computational predictions using *B. atropheus* spores which is a more relevant test aerosol for defense applications.

Chapter 6 of Appendix A summarizes the main conclusions of the dissertation (Appendix A).

Pages vi through xvii of Appendix A contains a list of figures with descriptions.

1.2 List of Contributors

Panagiotis D. Christofides	Professor Department of Chemical and Biomolecular Engineering University of Califonia, Los Angeles
Patrick R. Sislian	Ph.D. Graduate Department of Chemical and Biomolecular Engineering University of Califonia, Los Angeles
Lutz Mädler	Professor Department of Production Engineering University of Bremen
Minghen Li	Associate Professor Department of Chemical and Materials Engineering California State Polytechnic University, Pomona
Xinyu Zhang	Ph.D. Candidate Department of Chemical and Biomolecular Engineering University of Califonia, Los Angeles
David Pham	Ph.D. Student Department of Production Engineering University of Bremen
Jesse Rau	Undergraduate Student Department of Chemical and Biomolecular Engineering University of Califonia, Los Angeles

1.3 Publications

1. Sislian, P. R., J. Rau, X. Zhang, D. Pham, M. Li, L. Mädler and P. D. Christofides. Bacterial Aerosol Neutralization by Aerodynamic Shocks Using an Impactor System: Experimental Results for *B. atropheus* Spores. *Chemical Engineering Science*, 65, 4803-4815, 2010.

2. Sislian, P. R., D. Pham, X. Zhang, M. Li, L. Mädler and P. D. Christofides. Bacterial Aerosol Neutralization by Aerodynamic Shocks Using an Impactor System: Experimental Results for *E. coli* and Analysis. *Chemical Engineering Science*, 65, 1490-1502, 2010.

3. Sislian, P. R., X. Zhang, D. Pham, M. Li, L. Mädler and P. D. Christofides. Bacterial Aerosol Neutralization by Aerodynamic Shocks Using a Novel Impactor System: Design and Computation. *Chemical Engineering Science*, 64, 1953–1967, 2009.

Appendix A

P. Sislian Dissertation

The appendix contains the dissertation of Patrick Sislian which was submitted to the University of Calfornia, Los Angeles on June 2 of 2010. The dissertation includes ther required information needed in the final technical report including a description of the equipment, experimental procedures and computational codes.

Section 2.2 describes the novel impactor system design and includes a drawing of the parts.

Section 2.3.1 outlines the Pitot experimental pressure measurements used to measure the Mach number in the impactor system. Sections 4.2 and 5.2 describe the experimental procedures and setup used to assess the effect of an aerodynamic shock on *E. coli* vegetative cells and *B. atropheus* spores, respectively.

Section 2.3.2 details the gas dynamic equations and the code framework used to solve these equations. Section 3.2 describes the equations of motion for and their computational implementation. Section 4.3.3 describes the stochastic particle tracking model used in FLUENT to calculate the collection efficiency of the bacterial cells. Sample codes are included in Appendix B.

UNIVERSITY OF CALIFORNIA

Los Angeles

Neutralization of Bacterial Aerosols by Aerodynamic Shocks in a Novel Impactor System: An Integrated Computational and Experimental Study

A dissertation submitted in partial satisfaction of the
requirements for the degree Doctor of Philosophy
in Chemical Engineering

by

Patrick Sislian

2010

This page is intended blank and should not be used in the submission of the thesis.

It has the purpose of making the next page, the signature page, page ii.

The dissertation of Patrick Sislian is approved.

William C. Hinds

Gerassimos Orkoulas

Harold Monbouquette

Panagiotis D. Christofides, Committee Chair

University of California, Los Angeles

2010

Contents

List of Figures

List of Tables

ACKNOWLEDGEMENTS

Without the support of my advisors, colleagues and family this work would not have been possible. I want to first mention Prof. Sheldon K. Friedlander, whose passion for aerosol technology drove me to continue my education in Chemical Engineering and pursue my Ph.D. He was a great mentor who always encouraged me to have the confidence to come up with new ideas; including the ideas presented in this work. It was a joy and privilege to be around him if only for a short time. I also greatly appreciate Mrs. Friedlander's continued interest in the work and her hospitality at various family events.

My advisor, Prof. Panagiotis D. Christofides, has led by example. One only needs to ask his students about him to know his true character. He pushed to always do what is right and focus on the fundamentals of the work regardless of hype or others' personal opinions. My hardest times were when I missed a deadline he set because I knew he never missed his: he did not have to say anything. Without his support funding for this work would have been discontinued. He ventured into experimental work and took a big risk with me. Thank you Professor for all the advice on the plane rides back from Washington D.C.

Lutz Mädler whose friendship and advice during the difficult times has been a major reason for staying the course. The coffee walks around campus and the many lunches were always great. The runs around campus made me realize I was out of shape (relative to Lutz that is). This was in addition to the great theoretical and experimental insight he provided in this work. Even after moving to Germany, he had the time to make weekly group meetings and provide constructive and challenging feedback.

Mingheng Li spent countless hours helping us with our computational models from the very beginning. My colleagues Xinyu Zhang and David Pham always challenged me with their work ethic and even on the basketball court once or twice. Jesse Rau's help during the last two quarters was very important. I believe we are only as good as the people we surround ourselves with. I consider myself lucky to be surrounded by not only outstanding professionals but also outstanding individuals in their personal lives.

I also want to thank Raffi and Nazig for all the weekends spent at their house away from the everyday and for making Los Angeles a home away from home.

Finally, I will never be able to summarize my family's support in a paragraph: my mom Sylva, my dad Raffi and my brother Sevag. You made it easy: I never had to look outside of this circle to find a role model to emulate. Everyday, I had live examples of how to take tough decisions and survive through the good and bad. It is easy, with you around, to focus on my work. For your love and support I am and will be forever grateful.

Chapter 2 is a version of Sislian, P. R., X. Zhang, D. Pham, M. Li, L. Mädler and P. D. Christofides. Bacterial Aerosol Neutralization by Aerodynamic Shocks Using a Novel Impactor System: Design and Computation *Chemical Engineering Science*, 64, 1953–1967, 2009.

Chapter 3 is a version of Sislian, P. R., X. Zhang, D. Pham, M. Li, L. Mädler and P. D. Christofides. Bacterial Aerosol Neutralization by Aerodynamic Shocks Using a Novel Impactor System: Design and Computation *Chemical Engineering Science*, 64, 1953–1967, 2009.

Chapter 4 is a version of Sislian, P. R., D. Pham, X. Zhang, M. Li, L. Mädler and P. D. Christofides. Bacterial Aerosol Neutralization by Aerodynamic Shocks Using an Impactor System: Experimental Results for *E. coli* and Analysis. *Chemical Engineering Science*, 65, 1490–1502, 2010.

Chapter 5 is a version of Sislian, P. R., J. Rau, X. Zhang, D. Pham, M. Li, L. Mädler and P. D. Christofides. Bacterial Aerosol Neutralization by Aerodynamic Shocks Using an Impactor System: Experimental Results for *B. atropheus* Spores. *Chemical Engineering Science*, submitted, 2010.

VITA

September 17, 1982	Born, Beirut, Lebanon
2004	Associate Engineer Amgen Inc., Thousand Oaks, California
2005	Bachelor of Science, Chemical Engineering Bachelor of Science, Biochemistry University of California, Los Angeles
2005	Visiting Researcher Delft University of Technology, The Netherlands
2006–2010	Teaching Assistant and Associate Department of Chemical and Biomolecular Engineering University of California, Los Angeles
2007–2008	UC Toxic Substance Research and Training Grant Department of Chemical and Biomolecular Engineering University of California, Los Angeles
2007–2010	Defense Threat Reduction Agency, Basic Research Grant Department of Chemical and Biomolecular Engineering University of California, Los Angeles
2009	Dissertation Year Fellowship Department of Chemical and Biomolecular Engineering University of California, Los Angeles
2009	Chemical and Biological Defense Conference Scholarship Department of Chemical and Biomolecular Engineering University of California, Los Angeles

PUBLICATIONS AND PRESENTATIONS

1. Sislian, P. R., J. Rau, X. Zhang, D. Pham, M. Li, L. Mädler and P. D. Christofides. Bacterial Aerosol Neutralization by Aerodynamic Shocks Using an Impactor

System: Experimental Results for *B. atropheus* Spores. *Chemical Engineering Science*, submitted, 2010.

2. Sislian, P. R., D. Pham, X. Zhang, M. Li, L. Mädler and P. D. Christofides. Bacterial Aerosol Neutralization by Aerodynamic Shocks Using an Impactor System: Experimental Results for *E. coli* and Analysis. *Chemical Engineering Science*, 65, 1490-1502, 2010.

3. Sislian, P. R., X. Zhang, D. Pham, M. Li, L. Mädler and P. D. Christofides. Bacterial Aerosol Neutralization by Aerodynamic Shocks Using a Novel Impactor System: Design and Computation. *Chemical Engineering Science*, 64, 1953–1967, 2009.

4. Sislian, P. R., D. Pham, X. Zhang, M. Li, L. Mädler and P. D. Christofides. Bacterial Aerosol Neutralization by Aerodynamic Shocks in a Novel Impactor: An Integrated Computational and Experimental Study. *Chemical and Biological Defense Science and Technology*, Dallas, TX, 2009.

5. Sislian, P. R., D. Pham, X. Zhang, M. Li, L. Mädler and P. D. Christofides. Bacterial Aerosol Neutralization by Aerodynamic Shocks in a Novel Impactor: An Integrated Computational and Experimental Study. *AIChE Annual Meeting*, Nashville, TN, 2009.

6. Sislian, P. R., L. Mädler, D. Pham, M. Li, X. Zhang and P. D. Christofides. Bacterial Aerosol Neutralization by Shock Waves Using a Novel Impactor: De-

sign, Computation and Experiments. *AIChE Annual Meeting*, Philadelphia, PA, 2008.

7. Sislian, P. R., L. Mädler. Nanoparticle Synthesis and Characterization: Application to Bacterial Cell Uptake. *UC TSR&TP Annual Symposium*, Riverside, CA, 2008
8. Sislian, P. R., L. Mädler, S. K. Friedlander and P. D. Christofides. A Study Of Bacterial Aerosol Neutralization By Shock Waves Using A Novel Impactor. *AIChE Annual Meeting*, Salt Lake City, UT, 2007.
9. Sislian, P. R., L. Mädler. Nanoparticle Synthesis and Characterization: Application to Bacterial Cell Uptake. *UC TSR&TP Annual Symposium*, Santa Cruz, CA, 2007

ABSTRACT OF THE DISSERTATION

Neutralization of Bacterial Aerosols by Aerodynamic Shocks in a Novel Impactor System: An Integrated Computational and Experimental Study

by

Patrick Sislian

Doctor of Philosophy in Chemical Engineering
University of California, Los Angeles, 2010
Professor Panagiotis D. Christofides, Chair

Neutralization of bacterial aerosol releases is critical in countering bioterrorism. As a possible bacterial aerosol neutralization method that avoids the use of chemicals, we investigate the mechanical instabilities of the bacterial cell envelope in air as the bacteria pass through aerodynamic shocks. To carry out this fundamental investigation, a novel experimental impactor system is designed and built to simultaneously create a controlled and measured shock and to collect the bacteria after they pass through the shock. In the impactor system, the aerosol flows through a converging nozzle, perpendicular to a collection surface that has an orifice through which the shocked bacteria enter a deceleration tube. Both experimental measurements of the pressure in the impactor system at multiple points and computational fluid dynamics simulations are used to characterize quantitatively the shocks created in the impactor. Specifically, the developed computational model describes the evolution of both the gas and particle velocity and temperature in the impactor system to determine the forces exerted on the bacterial aerosol as they pass through the shock. The results indicate that the developed computational model predictions compare well with the experimental pressure measurements.

The bacteria experience relative deceleration because of sharp velocity changes in the aerodynamic shock created in the experimental impactor system. Computational model results indicate that vegetative *E. coli* cells require a critical acceleration of 3.0×10^8 m/s^2 compared to $3.9 - 16 \times 10^9$ m/s^2 for *B. atropheus* spores to break-up. Computed accelerations in the impactor system reach 5.9×10^9 m/s^2 which predict break-up of both vegetative cells and spores. Experimental findings demonstrate that aerosolized *E. coli* cells and *B. atropheus* spores that pass through aerodynamic shocks created in the experimental impactor system are an order of magnitude less likely to retain viability than those that pass through the impactor at conditions which do not lead to the generation of an aerodynamic shock, and therefore, do not reach the critical acceleration required for break-up. However, *B. atropheus* spores that do not break-up have a higher likelihood to remain live compared to *E. coli*.

Chapter 1

Introduction

1.1 Background on bacterial aerosol neutralization by aerodynamic shocks

Natural bacterial aerosol is present both in indoor and outdoor environments at background concentrations. The suspended bacterial particles usually range in size from 1 μm (single cells) to 10 μm (multiple cells or cells associated with debris) [58]. With respect to bioaerosol concentrations, the comparison of concentration data from different environments is, in general, very difficult. For outdoor environments, the reported literature values of bioaerosol concentration range from 80 cfu/ml in rural areas [5, 27, 47, 57] to 850 cfu/ml in urban areas [5, 15, 39, 41], where cfu refers to colony forming units. Indoor environments usually contain less bioaerosol. Different sources contribute to the background in different environments such as soil, water, plants and human activity (anthropogenic aerosol). In addition to bioaerosols present in indoor and outdoor environments at background concentrations, intentionally produced anthropogenic bacterial aerosols can potentially be used as bioterrorism agents, which are added to natural background concentrations.

Characteristics of a bacterial cell, such as degree of hydration, growth medium (e.g., agar vs. broth), Gram stain (+ve vs. -ve), and metabolic state (vegetative vs. spore) affect its survival [54, 55]. Survival rates of different bacterial cells are also affected by exposure to different air environments [54, 55]. Temperature, relative humidity, ultraviolet light, and atmospheric pollutants are some factors that contribute to cell viability loss. These environmental factors minimally injure spores compared to both Gram-negative and Gram-positive vegetative cells. Intentionally disseminating spores such as *Bacillus anthracis* (anthrax) can cause much greater harm than their vegetative forms because of their extended survival in air. Consequently, it is critical to study the effectiveness of neutralization techniques on spores for defense applications.

With respect to sensing, different approaches for biological aerosols have been studied and can be classified into four categories: (1) Nucleic Acid-based, (2) structure-based, (3) chemistry-based and (4) function-based [58]. Assuming the detection of these agents is possible, current methods are not effective in neutralizing the aerosol cloud at its source and mostly include containment of the aerosol release in order to minimize human exposure. These methods are limited to indoor environments and employ techniques such as high efficiency particulate air (HEPA) filtration, electrostatic precipitation, steam condensation, ultraviolet (UV) inactivation as well as diverting airflows [58].

The use of aerodynamic shocks holds promise as an alternative way to neutralize the bacterial aerosol at the source. The shock can be applied at the point of release both in indoor and outdoor air with the advantage of avoiding chemicals. Some experimental data exist in the literature [25, 40, 56] on the use of shock waves to neutralize bacteria; however, these studies are limited to bacterial liquid suspensions or powders and do not assess the effects of a shock in the aerosol phase. We aim at understanding the fate of the bioaerosol particles when exposed to shocks of different velocity, temperature and pressure gradients in air.

Although detailed data for the effect of shocks on bioaerosol particles are lacking, aerodynamic shocks have been shown to cause lysis of bacteria suspended in the liquid phase [40, 56]. Teshima et al. (1995) [56] studied the biomechanical effects on *E. coli* by attaching a test tube with the bacterial suspension at the end of a shock tube. The peak pressure of the shock was varied from 3 MPa to 14 MPa with 100 pulses and bacterial lysis was quantified by measuring leaked phenylalanine dehydrogenase activity [56]. At 14 MPa, 15% of the *E. coli* cells were destroyed [56]. The researchers mentioned the importance of the pulse width but failed to account for its effect [56]. In earlier studies, Lundbeck et al. (1963) [40] used a shock peak pressure of ≈ 6 MPa with variable number of pulses to neutralize bacteria suspended in the liquid phase.

The shocks were produced using a piston fitted to a stainless steel tube filled with suspension. The study showed a loss of viability of *E. coli* vegetative cells but did not show any significant effect on *B. subtilis* spores [40]. The authors also demonstrated that an increase in concentrations results in an increase of bacterial viability. Our approach to shock bioaerosol particles in an impactor system avoids concentration effect because individual cells pass through the shock; this allows understanding the mechanism of single bacterial lysis by an aerodynamic shock.

More recently, Horneck et al. (2001) [25] showed that only 0.01% of dried *B. subtilis* powder (mounted between two quartz plates) survived a shock peak of 32 GPa with 1 pulse. However, the temperature of the cells in the sample reached 250 °C [25] and it was not possible to separate the effect of the shock from that of temperature.

The aerodynamic shock represents a sharp change in fluid properties (velocity, temperature, pressure). Due to its inertia, a bacterial particle suspended in air will not be able to immediately adjust to a sharp drop in gas velocity and will therefore experience a relative deceleration. Rayleigh-Taylor instabilities in the bacterial membrane arise if the bacterial particle is accelerated (or decelerated) in a perpendicular direction to the bacteria-gas interface [7, 28]. We have computed the critical accelerations and Weber numbers needed for several bacterial aerosols to break-up (see Chapter 3). Higher surface tension and smaller diameter of the bacterium increase the critical accelerations needed for break-up (see Chapter 3). An impactor system has been built and modeled to achieve different bacterial accelerations through a well-defined aerodynamic shock (see Chapter 2). After passing through the shock, the bacterial aerosol is collected at low velocity (< 10 m/s) to avoid break-up at the point of impaction [53]. In the impactor system the aerosol flows through a converging nozzle, perpendicular to a collection surface. The collection surface has an orifice through which the shocked bacteria enter a deceleration tube where their velocity is reduced to avoid neutralization by impaction. The work focuses on the development of a computational gas (flow and temperature) and particle motion model for the impactor system capable of predicting the effect of the shock on the bacterial aerosols. Experimental pressure measurements provide information about the flowfield in the impactor and are compared with computational model predictions. Sharp changes in velocity, temperature and pressure across the shock induce instabilities on the bacterial membrane. The magnitude of the deceleration of the bacterial particle is calculated and is compared with theoretical values needed for the neutralization of different bacteria.

Experimental measurements of cell viability in the impactor system provide are compared to the theoretical predictions. Both vegetative cells (Chapter 4) and spores (Chapter 5) are aerosolized and collected after operating the impactor at different operating conditions. A mass balance calculation reveals the percentage of cells that break-up after the operation of the impactor.

1.2 Dissertation objectives and structure

The objective of this dissertation is to study for the first time the effect of aerodynamic shocks on bacterial aerosols. The dissertation provides a theoretical and computational framework that allows for the prediction of operating conditions and geometry of the impactor system that lead to bacterial aerosol neutralization. A detailed understanding of the mechanisms of loss of cell viability is critical for both defense applications as well as for the design of bacterial aerosol samplers. For defense applications, the results allow for the design of aerodynamic shocks that are able to neutralize specific bacterial aerosols. For the design of collection devices, the results indicate the operating conditions which will prevent break-up of cells if the goal is to collect live cells for later analysis.

The structure of this thesis is as follows: first, the novel impactor system is introduced in Chapter 2. Specifically, the advantages of using the impactor system are highlighted in relation to studying the effects of aerodynamic shocks: simultaneous collection and control of shock strength. The gas dynamics of the impactor system is studied with both experimental measurements and computational model simulations. The Mach number of the aerodynamic shock is shown to be a function of the operating conditions as well as the geometry of the impactor. The experimental measurements verify the computational gas dynamics model which is used in Chapter 3.

Chapter 3 explores the motion of the bacteria as they travel through the impactor system: specifically, the deceleration forces that act on the bacteria as they passe through the aerodynamic shock. These forces are computed for the different geometries and operating conditions of the impactor system and are compared to the Rayleigh-Taylor break-up model. Knowing the critical Rayleigh-Taylor accelerations needed to break-up a cell and the decelerations achieved in the impactor system, we are able to make predictions on which cells survive.

In Chapter 4, the predictions obtained from the previous chapters are tested by passing aerosolized *E. coli* vegetative cells through the experimental impactor system. Furthermore, a stochastic random walk model is used to determine the collection efficiency at different experimental operating conditions. The model developed in Chapter 3 is confirmed with the experimental viability measurements obtained using a fluorescence flow cytometer.

Chapter 5 provides more experimental data to confirm the computational predictions using *B. atropheus* spores which is a more relevant test aerosol for defense applications.

Chapter 6 summarizes the main conclusions of this dissertation.

Chapter 2

Impactor System: Design and Aerodynamics

2.1 Introduction

Aerodynamic shocks are created in an impactor system described in detail in this chapter. The impactor geometry offers various advantages over other systems where aerodynamic shocks are created. First, the impactor allows for simultaneously passing the bacterial aerosol through an aerodynamic shock and achieving their collection. Second, the impactor system isolates the neutralization effect of the aerodynamic shock from that of impaction, dehydration and temperature. These two advantages allow for detailed experimental analysis of various bacterial aerosols (see Chapters 4 and 5). A computational fluid dynamics model is developed in this chapter which will be used in the break-up model of the bacterial particles in Chapter 3.

2.2 Design of the impactor system

The impactor system consists of a plate designed for the collection of the bacterial aerosol (see Fig. 2.1; parts 2 & 3) which is placed perpendicular to the gas flow emerging from a converging nozzle (see Fig. 2.1; part 1). Isentropic flow theory of an ideal gas predicts a critical downstream (P_1) to upstream (P_0) pressure ratio below which the flow at the exit of the nozzle is sonic [38, 48], according to the following equation:

$$\chi_{crit} = P_1/P_0 = [2/(\gamma+1)]^{\gamma/(\gamma-1)}, \tag{2.1}$$

where γ is the heat capacity ratio ($\gamma = 1.4$; $\chi_{crit} = 0.53$ for air). The generated impinging flow on a plate from a converging nozzle operating under sonic conditions results in the creation of a standoff shock whose properties can be changed by varying impactor geometry and operating conditions [2, 13, 14, 29, 42]. In traditional impactors [21, 22], the aerosol is collected by impaction on a flat surface. Stewart et al. (1995) [53] showed that bacteria collected by impaction are injured [53]; therefore, assessing damage induced by the standoff shock is impossible using current impactor designs. To avoid loss of viability by impaction, the flat surface of the developed impactor system has an opening (see Figure 2.1; part 2) that acts as a virtual surface through which the bacteria enter a stagnant gas deceleration tube (see Figure 2.1;

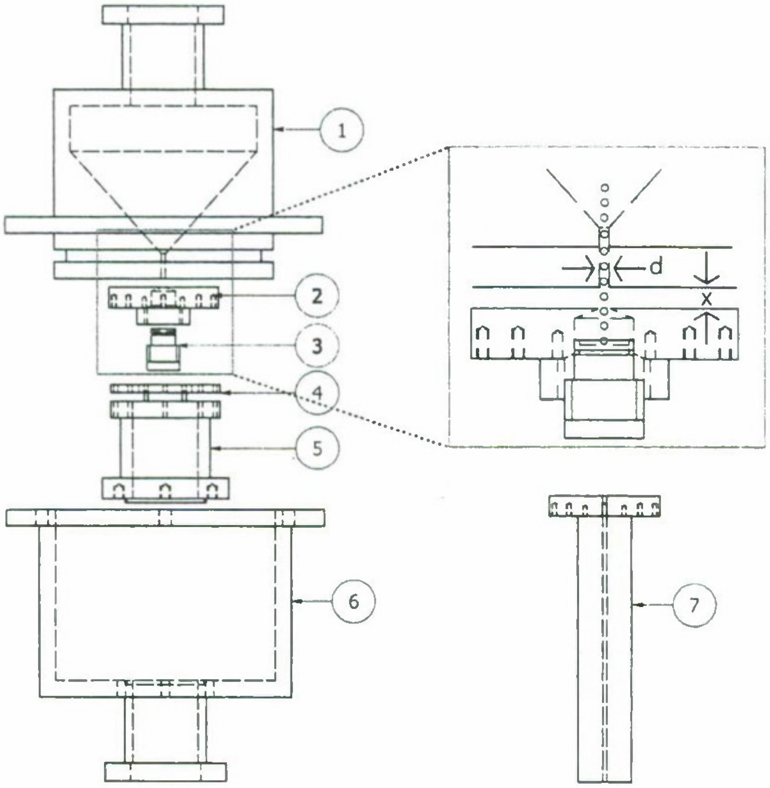

Figure 2.1: Schematic of the impactor system. (1) Converging nozzle with an exit diameter of either 0.5 mm or 1 mm, (2) and (3) a flat surface with a 0.5 mm or 1 mm hole combined with a screw that accommodates the collection substrate make up the deceleration tube (these parts can be replaced with a Pitot tube to measure the stagnation pressure), (4) spacers allow variation of the plate to nozzle distance from 0 mm to 2 mm, (5) support holding the deceleration tube and flat surface at fixed distance from the nozzle, (6) exit chamber, and (7) Pitot tube which can replace parts 2 and 3 for stagnation pressure measurements.

parts 2 and 3). Biswas and Flagan (1988) have designed a similar tube to prevent particle reentrainement [4]. The final velocity of the bacterium is related to the length of the tube (δl) and is calculated, assuming that the air in the deceleration tube is stagnant, using a force balance of the form:

$$m_p \frac{dv_p}{dt} = m_p v_p \frac{dv_p}{dx} = F_D + m_p g, \tag{2.2}$$

the drag force F_D is given by Stokes-Cunningham law as follows:

$$F_D = \frac{-3\pi\mu d_p v_p}{C_c}, \tag{2.3}$$

where m_p is the bacterium mass, v_p is the bacterium velocity, d_p is the bacterium diameter, x is the axial coordinate, g is the gravitational constant, and μ is the dynamic viscosity of the gas. C_c, the Cunningham slip correction factor, accounts for non-continuum effects (for 1 μm particles $C_c = 1.164$ [18]). The length of the deceleration tube ($\delta l = (C_c m_p v_p|_x)/(3\pi\mu d_p)$) is obtained by integrating Eq. 2.2 (neglecting the effect of gravity) between the tube inlet ($x' = x$) and the impaction surface at the end of the deceleration tube ($x' = \delta l + x$). The length of the tube, δl, varies between 1 mm to 4 mm in the impactor design of Fig. 2.1, which is sufficient to collect 1 μm particles entering the deceleration tube at velocities ($v_p|_x$) up to 680 m/s. The bacterium experiences deceleration both as it passes through the shock and in the boundary layer of the plate; therefore, a tube between 2 mm and 4 mm in length is sufficient to collect bacteria at negligible velocities. More detailed computational modeling of the impactor system (see Section 3.2) confirms that the bacterium velocity at the entrance of the deceleration tube ($v_p|_x$) is much smaller than $v_p|_x = 680$ m/s which is assumed in the design of the deceleration tube. A detailed solution of Eqs. 2.2 and 2.3, without the assumption of stagnant gas, reveals low impaction velocities (< 10 m/s) at the point of collection (see Section 3.2).

The deceleration tube (see Fig. 2.1; parts 2 and 3 combined) is held on a support (see Fig. 2.1; part 5). The distance between the opening of the deceleration tube and the nozzle outlet (x) can be adjusted with spacers of different thickness (see Figure 2.1; part 4). The exit chamber (see Fig. 2.1; part 6) has two outlets (see Fig. 2.1; part 7); one outlet connects to a vacuum pump and the other connects to a pressure gauge for Pitot measurements. The upstream pressure (P_0) and the downstream pressure (P_1) are measured through small orifices drilled normal to the side walls of the converging nozzle and of the exit chamber, respectively (see Fig. 2.1; part 7). A valve attached to a purge stream downstream of the impactor controls P_1, whereas a nitrogen tank with a pressure regulator controls P_0.

Depending on the method of analysis, different collection substrates can be placed on the top surface of the screw (see Fig. 2.1; part 3) to collect the shocked bacteria. A silicon wafer substrate is used for scanning electron microscopy (SEM) and a copper grid is used for transmission electron microscopy (TEM). Both analysis techniques reveal qualitative structural data of the collected samples. Biochemical analysis can also be carried out by placing a black polycarbonate filter on the top surface of the screw (see Fig. 2.1; part 3), which is stained during post processing using a LIVE/DEAD®*Bac*Light^{TM} (cat. number L7012; Life Technologies Corporation) to assess the viability of the collected bacteria, both quantitatively and qualitatively. Experimental results and analysis of the collected bacteria are discussed in detail in Chapters 4 and 5.

Parts 2 & 3 can be replaced with a Pitot tube that has the same diameter opening as the deceleration tube (0.5 mm or 1.0 mm). The Pitot tube extends beyond the support and exit chamber (see Fig. 2.1) and is connected to a pressure gauge that measures the stagnation pressure. The alternate Pitot setup, similar to the ones used in previous studies [16, 45], allows experimental characterization of the standoff shock (see Section 2.3.1 below). The developed system therefore has the advantage of passing the bacteria through a controlled and measured aerodynamic shock and simultaneously collecting them on various substrates for further analysis. The simultaneous collection eliminates the need to sample the bacterial aerosol compared to shock tube geometries, thereby reducing sampling errors. Both the operating pressures (P_0 and P_1) and the geometry of the impactor (nozzle diameter, d, and plate to nozzle distance, x) affect the properties of the aerodynamic shock [13, 14]. Their effect will be quantitatively studied below.

2.3 Experimental and computational studies of the impactor system

The velocity, pressure, and temperature of the gas in the impactor system for different geometric and operating conditions are important parameters in determining the forces that act on a bacterium as it passes through the aerodynamic shock. Experimental measurements are compared with computational fluid dynamics (CFD) model predictions. CFD calculations provide velocity, pressure and temperature data at every point in the impactor system which are not accessible in the experimental impactor system. The CFD profiles are also used to predict the particle velocity and temperature in the impactor system (see Chapter 3). Therefore, comparison of the experimental and computational data provides realistic predictions of the eventual fate of different bacterial particles as they pass through the shock and are collected in the system.

2.3.1 Experimental results: Pitot pressure measurements

One of the directly measured variables in the experimental impactor system of Fig. 2.1 (see Section 2.2) is the Pitot stagnation pressure (P_p) after the shock. While a detailed CFD model has been developed for the experimental impactor system (see Section 2.3.2 below), in order to be able to compare our experimental measurements with results available in the literature, we first develop an impactor model based on appropriate simplifying assumptions to estimate the Mach number before the shock (M_1) using the Pitot pressure measurement (P_p) along with that of upstream (P_0) and downstream (P_1) pressures.

Specifically, the gas is considered to be thermally perfect (i.e., the enthalpy (h) is only a function of temperature; $h = h(T)$) and calorically perfect (i.e., the heat capacity (c_p) at constant pressure is not a function of the temperature; $c_p \neq c_p(T)$). Along the center streamline, the flow before and after the shock is assumed to be one dimensional, steady-state and isentropic (i.e., adiabatic and frictionless). These conditions lead to $p_{01} \approx P_0$ and $p_{02} \approx P_p$, where p_{01} and p_{02} are the stagnation (or total) pressures before and after the shock, respectively. Both P_0 and P_p are experimentally measured in our system (see Section 2.2). The flow through a shock is non-isentropic ($p_{01} \neq p_{02}$; i.e., not in equilibrium). Assuming that the shock is infinitely thin and normal to the center streamline, the following equation can be used to relate the stagnation pressures to the Mach number before the shock [38, 48]:

$$\frac{P_p}{P_0} \approx \frac{p_{02}}{p_{01}} = \left[1 + \frac{2\gamma}{\gamma+1}({M_1}^2 - 1)\right]^{-1/(\gamma-1)} \cdot \left[\frac{(\gamma+1){M_1}^2}{(\gamma-1){M_1}^2 + 2}\right]^{\gamma/(\gamma-1)}, \tag{2.4}$$

where γ denotes the heat capacity ratio and M_1 is the Mach number before the shock. The Mach number after the shock (M_2) can also be calculated using M_1 under the above flow assumptions using the following formula [38, 48]:

$${M_2}^2 = \frac{1 + \frac{\gamma-1}{2}{M_1}^2}{\gamma {M_1}^2 - \frac{\gamma-1}{2}}, \tag{2.5}$$

Although the experimental pressure measurements do not provide a detailed picture of the flow-field in the impactor, one can use the Mach number before the shock as a measure of the velocity change ($M_1 - M_2$) over the thickness of the shock which can be estimated to be on the order of one mean free path (λ) of the gas, which is given by [9]:

$$\lambda = 2.15\mu T_{01}^{1/2}/P_{01}, \tag{2.6}$$

where T_{01} and P_{01} are the static temperature and pressure before the shock, respectively. The Mach number combined with the shock thickness is important in determining the forces exerted on the bacterial particles (see Sections 3.2 and 3.3).

The flow-field assumptions used in the derivation of Eqs. 2.4 and 2.5 give rise to errors in determining the actual shock Mach number. Detailed CFD simulations (see Section 2.3.2) can be used to compute a better estimate of the Mach number and will therefore be used in the development of a bacterial particle break-up model (see Section 3.3). Nonetheless, the experimental Pitot measurements constitute a basis for comparison with both experimental data found in the literature and with the CFD simulations. The experimental impactor systems found in the literature are geometrically different from the impactor system of Figure 2.1 [16, 42, 45]. Although, impactor system geometry is an important factor that affects the flow characteristics of the impinging jet, a comparison is still useful if the objective is to determine whether the two sets of measurements (Pitot pressure) or calculations (Mach number) fall within the same range. Therefore, even when the operating conditions are the same, we do not expect the measurements and calculations to agree perfectly.

Specifically, Powell calculated an oscillating Mach number as a function of the distance between the nozzle and the Pitot tube, x/d [42]. Measurements with the current system (see Fig. 2.1) were carried out to mimic Powell's operating conditions ($P_0 = 3.72$ atm and $P_1 = 1$ atm) (Fig. 2.2). However, the geometries differ as follows: (1) $d = 7.9$ mm in Powell's setup [42] compared with $d = 0.5$ mm in the impactor

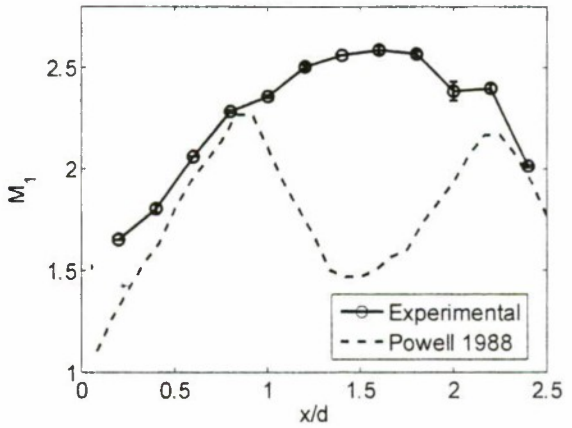

Figure 2.2: Experimental Mach number before the shock (M_1) calculated using Eq. 2.4 compared to measurements from Powell [42]. M_1 is plotted as a function of x/d. The operating conditions are the same for both sets of measurements with $P_0 = 3.72$ atm and $P_1 = 1$ atm ($P_1/P_0 = 0.27$). The geometries are different.

system of Fig. 2.1, and (2) a Pitot tube of unspecified geometry without the flat plate is used in Powell's case [42], thereby avoiding impinging flow. Due to this fact, in the experimental x/d range shown in Figure 2.2, Powell's data have two maxima and one minimum whereas in the experimental measurements of the impactor system such behavior is not observed. Both measurements though predict Mach numbers that are in the same range, i.e. M_1 is between 1 and 2.75 (see Figure 2.2).

In the experimental impactor system of Fig. 2.1, more measurements were done with geometries of varying plate to nozzle distance ($0.2 < x/d < 2.4$; limited only by the spacer thicknesses) at different upstream (1.0 atm$< P_0 <$ 8.9 atm) and downstream pressures (0.12 atm$< P_1 <$ 0.9 atm). We compared measurements of P_p/P_0 at constant P_1/P_0 for different upstream and downstream pressures. In Figure 2.3, the P_p/P_0 measurements are identical for equal P_1/P_0 with different upstream pressures.

These results indicate that the main variable determining the ratio, P_p/P_0, is the upstream to downstream pressure ratio instead of the absolute values of the pressures. CFD results further confirm these observations (see Section 2.3.2 below).

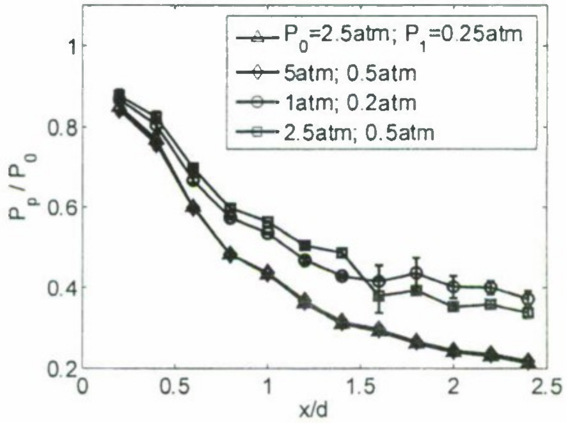

Figure 2.3: Two sets of two Pitot pressure measurements in the developed impactor system presented as a function of x/d for different upstream and downstream pressures; the ratio, P_1/P_0, remains fixed. (Set 1) $P_1/P_0 = 0.1$ with $(P_0(atm), P_1(atm)) = \{(2.5, 0.25), (5.0, 0.50)\}$, and (set 2) $P_1/P_0 = 0.2$ with $(P_0(atm), P_1(atm)) = \{(1.0, 0.20), (2.5, 0.50)\}$.

Fig. 2.4 shows the variation of the Mach number (M_1) with x/d for different P_1/P_0. The Mach number increases with decreasing P_1/P_0 and this trend is more pronounced at higher x/d $(x/d > 1)$ which is observed in the computational results shown in Section 2.3.2 below (see Fig. 2.9-a). Fig. 2.4 reenforces the findings of Fig. 2.3 in that measurements made with the same P_1/P_0 but different P_0 and P_1 yield similar curves. Specifically, the calculated M_1 for $P_1/P_0 = 0.05$ is identical for two upstream pressures $P_0 = 8.5$ atm and 5 atm. The highest Mach number, calculated using Equation 2.4, with the current setup was $M_1 = 3.93 \pm 0.01$ at $P_0 = 8.93 \pm 0.01$ atm.

$P_1 = 0.41 \pm 0.01$ atm ($P_1/P_0 = 0.05$) and $x/d = 2.4$. The errors in the measurements are computed using the standard deviation of 3 independent Pitot measurements and are on the order of 0.01 atm. These measurements, along with the CFD predictions, are essential in understanding the key parameters that influence bacterial aerosol neutralization.

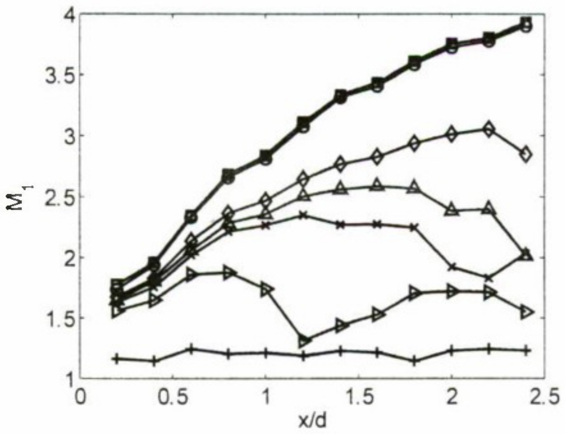

Figure 2.4: Experimental Mach number before the shock (M_1) in the impactor system of Fig. 2.1 calculated using Eq. 2.4 as a function of x/d. Curves represent different operating conditions, represented by the downstream to upstream pressure ratio, P_1/P_0. $[P_1/P_0, P_0, P_1]$ = (□) 0.05, 8.5 atm, 0.4 atm (○) 0.05, 5 atm, 0.25 atm (◇) 0.16, 2.5 atm, 0.4 atm (△) 0.27, 3.72 atm, 1 atm (×) 0.25, 1 atm, 0.25 atm (▷) [0.32, 1 atm, 0.32 atm] (+) 0.50, 1 atm, 0.5 atm.

2.3.2 Computational results: gas flow and thermal fields

For the two-phase aerosol flow (air-bacteria) present in the impactor system, the equations for gas and particle dynamics are coupled. At low aerosol concentrations, however, the particle dynamics can be assumed to have no effect on the gas flow field [18], and the equations of particle velocity and temperature can be decoupled from those of the gas phase. The gas dynamics can therefore be solved independently and the results are then used to determine the particle trajectories (see Section 3.2 below). An Eulerian approach is used to solve the gas flow field. Because the flow is turbulent, a full solution to the Navier-Stokes equations requires computationally intensive Direct Numerical Simulation (DNS). In this work, the Reynolds-averaged Navier-Stokes (RANS) equations are solved so that the small-scale turbulence fluctuations do not have to be simulated directly. In Reynolds averaging, variables such as velocity, pressure and energy are decomposed into a mean and fluctuating components as follows:

$$\phi = \overline{\phi} + \phi', \text{ with } \overline{\phi} = \frac{1}{\Delta t}\int_{t_0}^{t_0+\Delta t} \phi \, dt, \text{ and } \overline{\phi}' = 0, \tag{2.7}$$

where ϕ is a scalar property of the fluid (e.g., velocity magnitude, pressure, temperature, energy ...), and $\overline{\phi}$ is the time-averaged component of ϕ with the corresponding fluctuating component ϕ'. If we substitute the above form for the flow variables into the instantaneous Navier-Stokes equations and take a time average, we obtain the equations that describe the gas flow field. For simplicity and to provide an idea of the terms included in these equations, we provide below the general form of these equations in Cartesian tensor form (after dropping the overbars):

$$\frac{\partial \rho}{\partial t} + \frac{\partial}{\partial x_j}(\rho v_j) = 0, \tag{2.8}$$

and

$$\begin{aligned}&\frac{\partial}{\partial t}(\rho v_i)+\frac{\partial}{\partial x_j}(\rho v_i v_j)\\&=-\frac{\partial p}{\partial x_i}+\frac{\partial}{\partial x_j}\left[\mu\left(\frac{\partial v_i}{\partial x_j}+\frac{\partial v_j}{\partial x_i}-\frac{2}{3}\delta_{ij}\frac{\partial v_l}{\partial x_l}\right)\right]+\frac{\partial}{\partial x_j}(-\rho\overline{v_i'v_j'}),\quad i=1,2,3,\end{aligned}\tag{2.9}$$

where ρ is the density, v is the velocity, p is the static pressure, δ is the Kronecker delta, μ is the viscosity, and i, j, and l are the indices. To close the form in Eq. 2.9, the Reynolds stress term $-\rho\overline{v_i'v_j'}$ is calculated using the Boussinesq hypothesis [24]:

$$-\rho\overline{v_i'v_j'}=\mu_t\left(\frac{\partial v_i}{\partial x_j}+\frac{\partial v_j}{\partial x_i}\right)-\frac{2}{3}\left(\rho k+\mu_t\frac{\partial v_l}{\partial x_l}\right)\delta_{ij},\tag{2.10}$$

where μ_t is the turbulent viscosity and k is the turbulent kinetic energy. Different turbulence models were employed and compared giving similar results (see Remark 1). Neglecting the effect of gravity, the turbulence model used is the standard $k-\epsilon$ model which is given by

$$\frac{\partial}{\partial t}(\rho k)+\frac{\partial}{\partial x_i}(\rho v_i k)=\frac{\partial}{\partial x_j}\left[(\mu+\frac{\mu_t}{\sigma_k})\frac{\partial k}{\partial x_j}\right]+G_k-\rho\epsilon-Y_M,\tag{2.11}$$

and

$$\begin{aligned}
&\frac{\partial}{\partial t}(\rho\epsilon) + \frac{\partial}{\partial x_i}(\rho v_i \epsilon) \\
&= \frac{\partial}{\partial x_j}\left[(\mu + \frac{\mu_t}{\sigma_\epsilon})\frac{\partial \epsilon}{\partial x_j}\right] + C_{1\epsilon}\frac{\epsilon}{k}(G_k + C_{3\epsilon}G_b) - C_{2\epsilon}\rho\frac{\epsilon^2}{k}, \\
&\mu_t = \rho C_\mu \frac{k^2}{\epsilon}, \\
&C_{1\epsilon} = 1.44,\ C_{2\epsilon} = 1.92,\ C_\mu = 0.09,\ \sigma_k = 1.0,\ \sigma_\epsilon = 1.3,
\end{aligned} \tag{2.12}$$

where ϵ is the rate of dissipation, and G_k is the generation of turbulent kinetic energy due to mean velocity gradients. σ_k and σ_ϵ are the turbulent Prandtl numbers. Y_M is the dilatation dissipation term, which represents the contribution of the fluctuating dilatation in compressible turbulence to the overall dissipation rate. Y_M is given by

$$Y_M = 2\rho\epsilon M_t^2 \tag{2.13}$$

where M_t is the turbulent Mach number, defined as

$$M_t = \sqrt{k/a^2} \tag{2.14}$$

where a ($= \sqrt{\gamma RT}$) is the speed of sound and γ ($=c_p/c_v$) is the ratio of specific heat. The final conservation law solved is the energy equation for the gas which is given, in Cartesian tensor form, as follows:

$$\begin{aligned}&\frac{\partial}{\partial t}(\rho E)+\frac{\partial}{\partial x_i}[v_i(\rho E+p)]\\&=\frac{\partial}{\partial x_j}\left[\alpha c_{p_g}(\mu+\mu_t)\frac{\partial T}{\partial x_j}+v_i(\mu+\mu_t)\left(\frac{\partial v_j}{\partial x_i}+\frac{\partial v_i}{\partial x_j}-\frac{2}{3}\delta_{ij}\frac{\partial v_l}{\partial x_l}\right)\right],\end{aligned}\tag{2.15}$$

where E is the internal energy, α is the thermal diffusivity, c_{p_g} is the heat capacity at constant pressure, and T is the static temperature.

A numerical solution program was written within FLUENT®, a CFD software, to solve the above equations for the computational domain shown in Fig. 2.5. Because the impactor is axisymmetric, a cross sectional grid that covers half of the impactor system is used. A different mesh is created for different distances between the nozzle and the impactor wall (x/d). The distance shown in Fig. 2.5 is $x/d = 4.0$ with a nozzle diameter of 0.5 mm. The grid is more dense (0.01 mm without adaption; 0.0025 mm with adaption) in the area between the nozzle outlet and the deceleration tube inlet in order to capture the details of the shock. Both the inlet and outlet boundaries are defined by stagnation pressures fixed at the pressures shown in Table 2.1 below and temperatures fixed at 300 K with the gas considered to be ideal. The walls are defined by zero heat flux (adiabatic) and no-slip boundary conditions. As for the centerline, we use axisymmetric boundary conditions. Full multi-grid (FMG) initialization is used with the first-order upwind scheme to obtain a convergent solution to the momentum equation. Next, the energy and turbulence equations are solved with a first-order scheme followed by a second-order upwind scheme to obtain convergent solutions with residuals of continuity, velocity, k and ϵ of less than 10^{-4} and energy residual of less than 10^{-6}. Subsequently, three grid adaptation steps are applied to refine the mesh in areas with high pressure gradients, specifically in the area between the nozzle exit and the deceleration tube inlet. Li et al. [34, 37, 35, 36] used a similar approach to solve for a high velocity oxygen-fuel (HVOF) thermal spray process involving a converging-diverging nozzle. A parametric study with different upstream and downstream pressures (see Table 2.1) is conducted to compare with the experimentally calculated Mach numbers (see Figs. 2.8 and 2.9) as well as to understand the effects of shocks with different properties on the bacterial aerosol. Cases 1 and 4 in Table 2.1 have different upstream pressures as boundary conditions; however, the ratio P_1/P_0 is constant. Case 5 is for comparison with experimental conditions that are similar to Powell's [42].

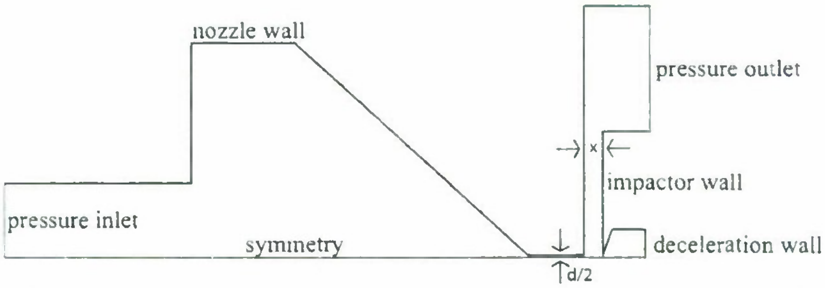

Figure 2.5: Computational domain and boundary conditions.

Theoretical and experimental observations indicate the presence of instabilities in the flow structure of the impinging jets in the presence of an impaction plate [2, 29, 42]. Understanding of the properties of an under-expanded free (absence of impaction plate) jet is essential for the study of instabilities for an impinging jet [42]. In a free jet,

Table 2.1: Inlet and outlet pressure conditions for parametric analysis of the impactor system with variable nozzle to plate distance (x/d). $(x/d)_c$ refers to the value of x/d where instabilities in the flow arise. x/d values are represented as: (min : increment : max).

Case	x/d	P_0 (atm)	P_1 (atm)	P_1/P_0	$(x/d)_c$
1 (base)	(0.2 : 0.1 : 4.0)	1.00	0.14	0.14	1.5
2	(0.2 : 0.1 : 2.4)	1.00	0.25	0.25	0.9
3	(0.2 : 0.1 : 2.4)	1.00	0.32	0.32	0.9
4	(0.2 : 0.1 : 2.4)	5.00	0.70	0.14	1.6
5 (for comparison)	(0.2 : 0.1 : 2.4)	3.72	1.00	0.27	-

as the flow emerges from the nozzle, it expands and accelerates to supersonic velocities creating a shock after which the gas velocity is subsonic [42]. The subsonic flow expands further to regain sonic velocity thereby matching the nozzle conditions [42]. The aerodynamic cell length is defined as the length of the region between the nozzle exit and the point where the free jet flow regains a near nozzle state. Instabilities in the flow structure (e.g., recirculation bubbles) arise when an impingement plate is placed at a distance equal to an aerodynamic cell length from the nozzle [42]. Jurcick et al. (1989) [29] computationally observed these instabilities by solving the time-dependent Navier-Stokes equations for $P_1/P_0 = 0.16$ and $x/d > 1.7$. Recirculation bubbles in the impingement zone, which lies at the center of the flow-field between the shock and the plate, are an indication of instabilities [2, 29]. Further study of the structure of the instabilities is outside the scope of this work; however, calculating the critical x/d [$(x/d)_c$] at which instabilities arise, using the developed computational fluid dynamics model, is important in analyzing the particle motion in the impactor system (see Section 3.2 below). Further analysis of the flow structure for $P_0 = 1$ atm

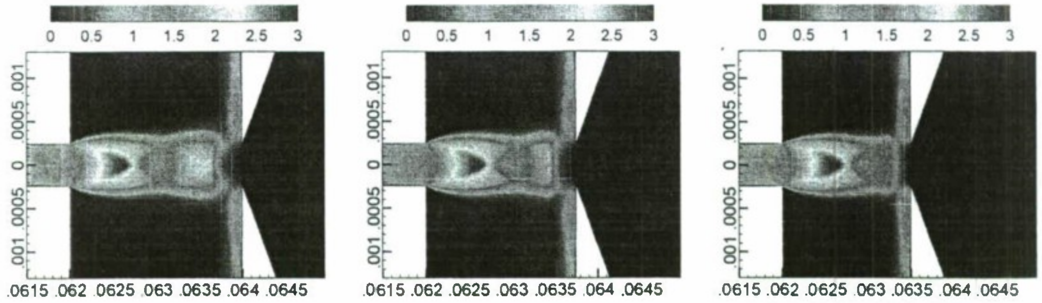

(a) x/d=4.0 (b) x/d=3.5 (c) x/d=3.0

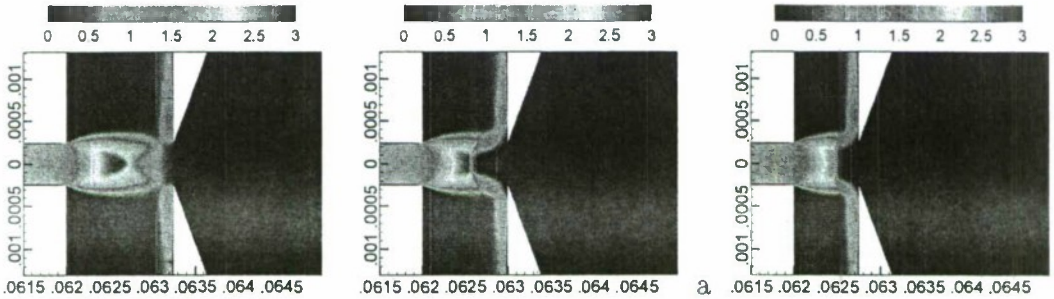

(d) x/d=2.5 (e) x/d=2.0 (f) x/d=1.5

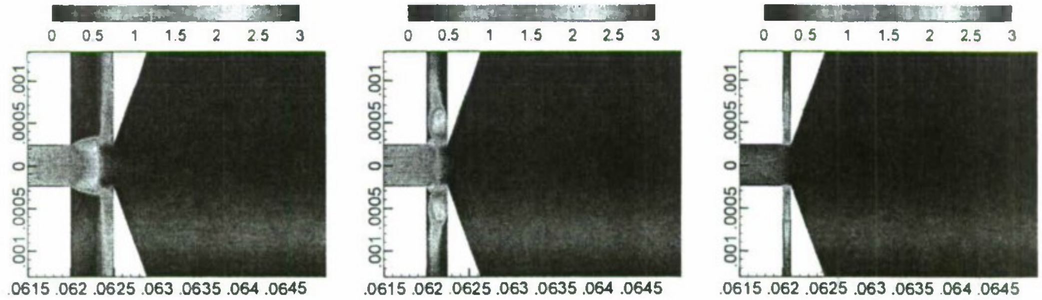

(g) x/d=1.0 (h) x/d=0.5 (i) x/d=0.2

Figure 2.6: Contour plots of the Mach number at different x/d for $P_0 = 1$ atm and $P_1 = 0.14$ atm. The x-axis is the distance along the centerline from the nozzle outlet and is given in meters.

and $P_1 = 0.14$ atm ($P_1/P_0 = 0.14$) reveals the appearance of recirculation bubbles at $x/d > 1.5$, which is consistent with the range $x/d > 1.7$ reported by Jurcick et al. (1989) [29]. The recirculation bubble velocities increase as x/d increases. As P_1/P_0 decreases recirculation bubbles form at lower x/d with lower velocities. Furthermore, as can be seen in Fig. 2.6, the shock structure evolves from shocks forming away from the centerline, to stand-off shocks, to diamond shock. At $x/d \leq 0.5$, the shocks form away from the centerline along the impactor walls because the nozzle area is not the critical flow area. As x/d increases, a stand-off shock forms perpendicular to the centerline with increasing Mach numbers. For $x/d > 2.0$, a shock diamond forms with a subsequent second shock. For the different operating conditions, our study will focus on $0.5 < x/d < (x/d)_c$ where the shock is stable and along the path that the particle follows to settle in the deceleration tube. Table 2.1 refers to the $(x/d)_c$ values where instabilities arise for all the operating conditions studied.

The centerline properties of the fluid are typical of the flow-field that a particle experiences before settling on the collection plate for analysis. In Section 3.2 the particle is released at the centerline. Therefore, the study will focus on the centerline properties of the complex flow field that develops in the experimental impactor of Fig. 2.1. Fig. 2.7 shows both the contour and centerline temperature, pressure and Mach numbers for $x/d = 1.5$, $P_0 = 1$ atm and $P_1 = 0.14$ atm. As the gas exits the nozzle at $x = 0.062$ m, it expands reaching supersonic velocities before the shock. Correspondingly the static temperature and pressure decrease as the gas expands. In Figure 2.7, the shock at 0.0625 m, is observed as a sharp change in the fluid properties, which is responsible for the forces experienced by the bacteria (see Sections 3.2 and 3.3 below). In the contour plots of Mach, temperature and pressure, a standoff shock perpendicular to the direction of the flow can be observed. The Mach contour pattern

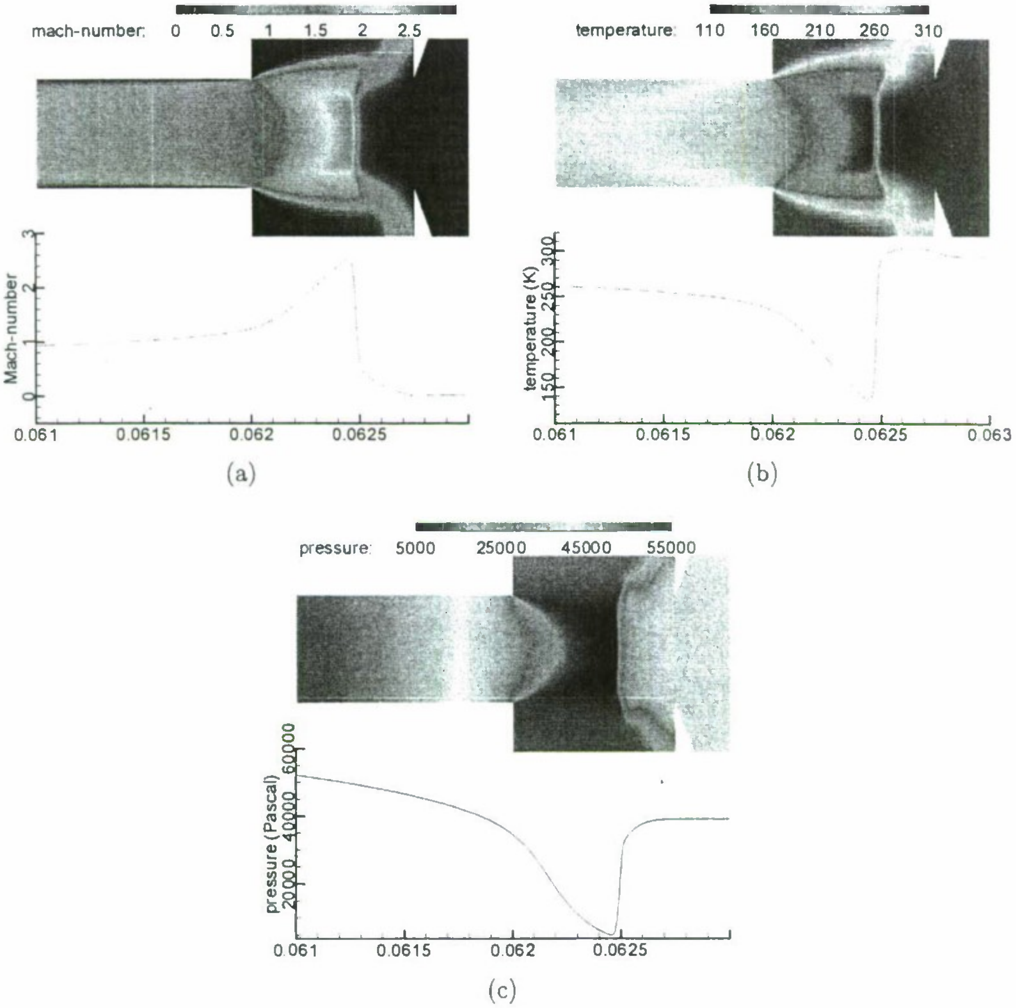

(a)

(b)

(c)

Figure 2.7: Contour plots (top plots) and centerline fluid properties (bottom plots) for (a) Mach number, (b) static temperature and (c) static pressure. The x-axis is the distance along the centerline from the nozzle outlet and is given in meters. The impactor is simulated at $x/d = 1.5$ with $P_0 = 1$ atm and $P_1 = 0.14$ atm.

is similar to the ones observed in experimental shadowgraphs and wave diagrams in the literature [2, 29].

In the CFD model, the Pitot pressure is the centerline static pressure at the end of the deceleration tube (see Remark 3). The CFD calculations are made using idealized assumptions, discussed above, such as perfect gas, axisymmetric flow, and frictionless walls. Whereas, in the experimental Pitot measurements these assumptions are not made and the pressure is measured directly. Therefore, we expect differences in the measured and computed values of the Pitot pressure. In Fig. 2.8-a, the computational results yield higher Pitot pressures. However, the extracted maximum centerline Mach numbers represent a more accurate picture of the gas dynamics; specifically, at $x/d < 0.5$. Equation 2.4 is for supersonic Pitot pressure measurements and does not account for subsonic conditions. At $x/d < 0.5$ the flow along the centerline is

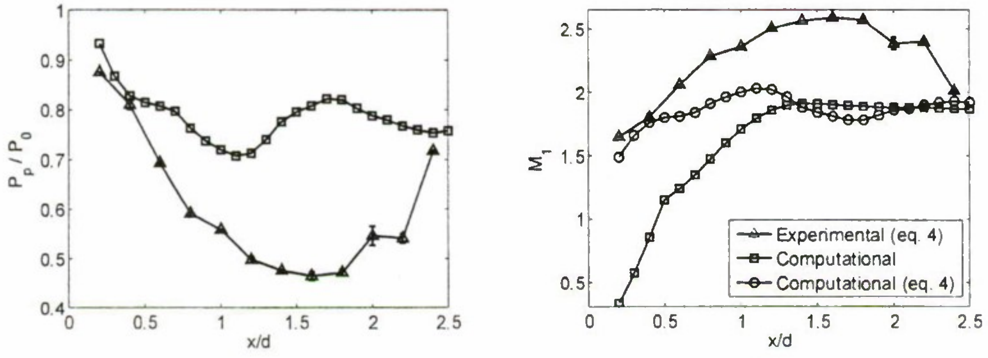

(a) (b)

Figure 2.8: (a) Pitot pressure versus x/d at $P_0 = 3.72$ atm and $P_1 = 1$ atm using both experimental and computational data of the experimental impactor system. It can be seen that the Pitot pressures are in agreement for very short distances but diverge as x/d increases. (b) Mach number versus x/d for the same conditions. (□) Maximum centerline Mach number extracted from computational gas dynamic field, (○) Mach number calculated using Eq. 2.4 and computational Pitot pressure data, (△) Mach number calculated using experimental Pitot pressure measurements.

subsonic as discussed above (see Fig. 2.6). Therefore, Eq. 2.4, which yields Mach numbers > 1 at $x/d < 0.5$, is not accurate. Eq. 2.4 also does not take into account the formation of two shocks (see Fig. 2.6) after certain x/d giving rise to additional errors at higher x/d.

Even though a perfect match is not expected as discussed above, the trends in the computational maximum centerline Mach numbers are similar to the experimental results calculated using Eq. 2.4 as shown in Fig. 2.9-a. The Mach number increases with decreasing P_1/P_0 and the effect is more pronounced after x/d of about 1. For the same upstream to downstream pressure ratio with different absolute values for the pressures, the maximum centerline Mach number is identical (see Fig. 2.9-b). This fact is also confirmed for Mach numbers calculated from the experimental Pitot measurements of Fig. 2.3 as well as the Mach numbers shown in Fig. 2.4.

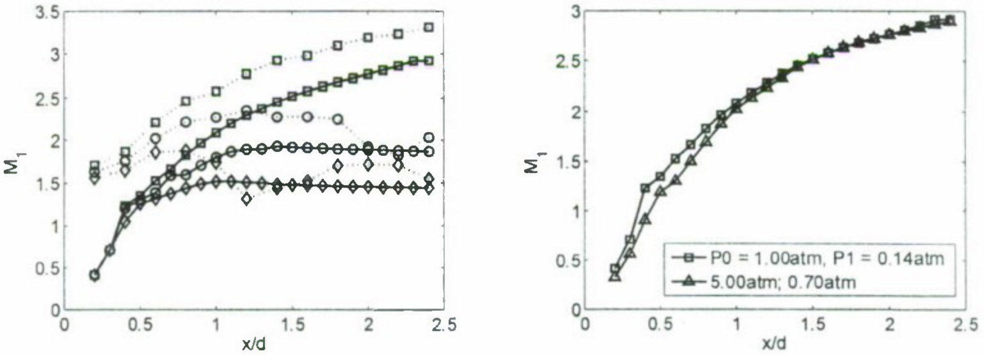

(a) (b)

Figure 2.9: (a) Computational (solid) vs. experimental (dotted) maximum centerline Mach number (M_1) at different P_1/P_0: (□) $P_1/P_0 = 0.14$ (solid) and 0.15 (dotted), (○) 0.25, (◇) 0.32. All the upstream pressures, P_0, are equal to 1. (b) Computational M_1 vs. x/d at constant $P_1/P_0 = 0.14$ for different upstream and downstream pressures.

Although temperature effects will not be considered in the discussion of the forces experienced by the particle (see Section 3.3 below), we acknowledge that this effect exists and will be the focus of further study. The minimum temperature on the centerline decreases as P_1/P_0 increases (see Fig. 2.10). For constant P_0/P_1, the minimum temperature is identical, mimicking the Mach trend of Fig. 2.9.

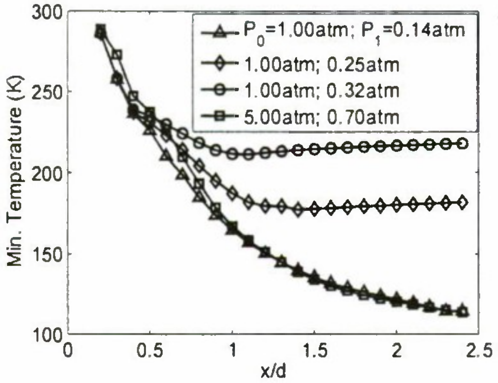

Figure 2.10: Minimum centerline temperature of the gas as a function of the normalized distance between the nozzle and the plate (x/d) for the 4 different (P_0, P_1) pairs.

In summary, the computational and experimental gas flow-field analysis yield similar trends as discussed above. The absolute values differ because of the assumptions in calculating the Mach number employed in the developed models. The more detailed CFD model will be used in determining the forces exerted on the bacterial particles as they travel through the experimental impactor system of Fig. 2.1.

Remark 1 *The centerline stagnation pressures at the end of the deceleration tube (Pitot pressures) were compared using Spalart-Allmaras, standard $k-\epsilon$, RNG $k-\epsilon$, and Realizable $k-\epsilon$ models and the results were found to have a maximum deviation of* 4%. *The operating conditions for the comparison were $x/d = 0.6$, $P_0 = 5.48$ atm and $P_1 = 0.08$ atm. Based on these results, the standard $k-\epsilon$ model was chosen in all the simulations discussed in the study.*

Remark 2 *As noted in Section 2.3.1, the shock thickness is on the order of the mean free path* (λ) *of the gas. In the simulation results shown in Fig. 2.7, the centerline velocity drop occurs over a range of about* $42\ \mu m$ *from a maximum Mach number of 2.52 to less than 1. The maximum mean free path along the centerline is* $0.51\ \mu m$ *which is much less than the distance over which the Mach number decreases. CFD comparisons are based on flow equations based on the assumption of continuity and are therefore not able to capture non-continuum shock properties such as the shock thickness. However, this has a minimal effect on computing the forces acting on the bacterium as can be seen in Section 3.2 below.*

Remark 3 *All the reported computational Pitot pressures are extracted from static pressure data along the centerline and at the end of the deceleration tube. A new mesh was also created to capture the length of the Pitot tube (7 cm) of Fig. 2.1-7. Calculations using the new Mesh at* $P_0 = 3.72$ *atm,* $P_1 = 1$ *atm and* $x/d = 1.6$ *reveal a Pitot pressure equal to that at the end of the deceleration tube* ($P_p = 3.00$ *atm*)*. The Pitot pressures are also equal by comparing the centerline pressure to the average pressure at the bottom of the deceleration tube. Therefore, reporting the centerline static pressure at the end of the deceleration tube is sufficient.*

2.4 Conclusions

An impactor system was developed capable of simultaneously passing the bacterial aerosols through a controlled shock and collecting them at low velocities. The Mach number of the aerodynamic shock can be varied by changing the operating conditions (P_1,P_0 and P_1/P_0) and the geometry (x/d) of the impactor system. A maximum Mach number of 3 is possible with the current design. Both experimental measurements and detailed computational fluid dynamics models were used to analyze the Mach number of the shock with close agreement. The computed Mach numbers using experimental Pitot measurements were in good agreement with Powell's experimental work [42], given the geometrical differences between the two systems.

Chapter 3

Bacterial Motion and Break-up

3.1 Introduction

Understanding the forces acting on the bacterial membrane as a vegetative cell or spore passes through the aerodynamic shock is critical and determines whether the bacterium will remain viable. Therefore, a model is needed to assess whether the force the bacterium experiences as it goes through the impactor is sufficient to cause loss of viability. In Chapter 2 we developed a computational model to understand the gas dynamics and this model, will be used in this chapter to compute the deceleration experienced by the bacterium as it passes through the shock.

In developing a model to understand the effect of the shock, we assume that break-up of the cell is needed to achieve cell neutralization; although this is a more stringent requirement than loss of viability. The critical force needed to break-up a cell is calculated using the Rayleigh-Taylor instability model which is compared to values from the bacterial motion model to provide predictions.

3.2 Bacterial motion in the impactor system

The bacterial motion in the impactor system is computed in Lagrangian coordinates utilizing the gas flow and temperature fields calculated using the CFD model of Section 2.3.2. Due to the very low bacterium loading, the coupling between the gas phase and the bacterial (particulate) phase can be considered to be one-way, i.e., the gas flow field solution is obtained by neglecting the presence of bacteria and is subsequently used unmodified in the calculation of the bacterium trajectories. In the bacterium model development, it is also reasonable to assume that coagulation is negligible and that particle size does not change during flight.

The particle motion in the impactor system is governed by Newton's second law and is given by

$$m_p \frac{dv_p}{dt} = \sum_i F_i, \tag{3.1}$$

where m_p is the particle mass, v_p is the particle velocity, t is the time, and F_i are the different forces that can act on the particle including the drag force, thermophoretic force, gravitational force, the basset history term, etc. For typical impactor operating conditions, the major force acting on a bacterial particle is the drag force, and the other forces can be neglected. As a result, the force balance of Equation 3.1

applied to bacterial particles traveling through the developed impactor system takes the following form:

$$m_p \frac{dv_p}{dt} = \frac{1}{2} C_D \rho_g A_p (v_g - v_p)|v_g - v_p|, \tag{3.2a}$$

$$\frac{dx}{dt} = v_p, \tag{3.2b}$$

where v_p and v_g are the velocity of the bacterial particle and gas, respectively, ρ_g is the density of the gas, A_p is the projected area of the bacterium on the plane perpendicular to the flow direction, and C_D is the drag coefficient. In the supersonic flows occurring in the impactor system, compressibility and non-continuum effects have to be considered in the evaluation of the drag coefficient C_D. Specifically, C_D is a function of both particle Reynolds ($Re_p = \rho_g d_p |v_g - v_p| / \mu_g$) and particle Mach ($Ma_p = |v_p - v_g|/s$; s is the speed of sound) numbers. For the simple case where the ratio of particle to gas absolute temperature, T_p/T_g, is approximately unity, data for $C_D = f(Re_p, Ma_p)$ is given in Clift, Grace and Weber [9]. At each grid point the Re_p and Ma_p are computed and a corresponding value for C_D is evaluated.

The bacterial particle is assumed to be spherical at all times. The density (ρ_p) of bacterium is 1 g/ml [59]. The dimension of bacterial particles varies depending on the species and the state of the individual bacterium. *B. subtilis*, for example, has a width of $0.7 - 0.8$ μm and a length of $2 - 3$ μm [33]. Most bacteria diameters are in the micrometer range, and we will therefore assume that they are spheres of $d_p = 1$ μm for simplicity. The effect of particle size is discussed in Section 3.3 below.

It is also reasonable to assume that the bacterial particles are heated with negligible internal resistance and that the internal bacterial temperature gradient can be ignored due to the small Biot number (ratio of heat transfer coefficient due to the boundary layer versus the internal heat conductance; see Remark 4 for a detailed analysis of this issue.). The mass of the particle, m_p, is constant. Therefore, we can model the evolution of the bacterial temperature accounting for the heat transfer between the particle and the gas with the following first-order ordinary differential equation:

$$m_p c_{p_p} \frac{dT_p}{dt} = hA'_p(T_g - T_p), \tag{3.3}$$

where c_{p_p} is the particle heat capacity at constant pressure and A'_p is the surface area of the particle. The heat transfer coefficient (h) is computed using the Ranz and Marshall correlation [43, 44]

$$h = \frac{k_g}{d_p}[2 + 0.6Re_p^{1/2}Pr^{1/3}], \tag{3.4}$$

where k_g is the thermal conductivity of the gas and Pr is the Prandtl number ($Pr = c_{p_g}\mu_g/k_g$). The thermodynamic properties of the bacterium are extracted from Datta [12].

A fifth order Runge-Kutta method is used in numerically integrating Equations 3.2a, 3.2b and 3.3 using the gas velocity and temperature fields obtained from the computational model of Section 2.3.2. The particle velocity and temperature are calculated every 10^{-7} m along the centerline of the impactor. These solutions are calculated for all conditions shown in Table 2.1, including flow-fields where instabilities are seen (see Remark 5).

Compared to the maximum gas Mach (M_1) shown in Figure 2.9-a, the maximum particle Mach number ($Ma_p = \max|v_p - v_g|/s$; s is the speed of sound) does not exhibit a clear trend versus x/d (see Figure 3.1-a). Ma_p is approximately equal for all operating conditions up to $x/d \approx 0.8$. There is a peak that occurs for $P_0 = 1.00$ atm and $P_1 = 0.25$ atm at $x/d \approx 1.1$. This might be because of the effect of the instabilities (see Remark 5 for a discussion on this issue). At higher x/d, the pressure pairs (P_0, P_1) = (1.00 atm,0.14 atm) and (5.00 atm,0.70 atm) have higher particle Mach numbers similar to the gas Mach number; however, these are at x/d values that exhibit instabilities. The minimum centerline particle temperature variation versus x/d of Figure 3.1-b is similar to the temperature variation of the gas phase in Figure 2.9-b. For equal ratio of P_1/P_0 the centerline particle temperature drop is higher for higher P_0. Therefore, although the gas flow and temperature are constant at constant P_1/P_0, the different absolute values of P_0 and P_1 affect the bacterial motion and temperature in the impactor system. Figures 3.2 and 3.3 show the particle and gas velocity profiles as well as the mean free path as a function of the distance from the nozzle (x) for different operating conditions. In Figure 3.2, x/d and P_0 are held constant at 1 and 1 atm, respectively, while P_1 assumes two values 0.14 atm and 0.25 atm. The mean free path is expected to be lower for $P_1 = 0.25$ atm and can be seen by comparing

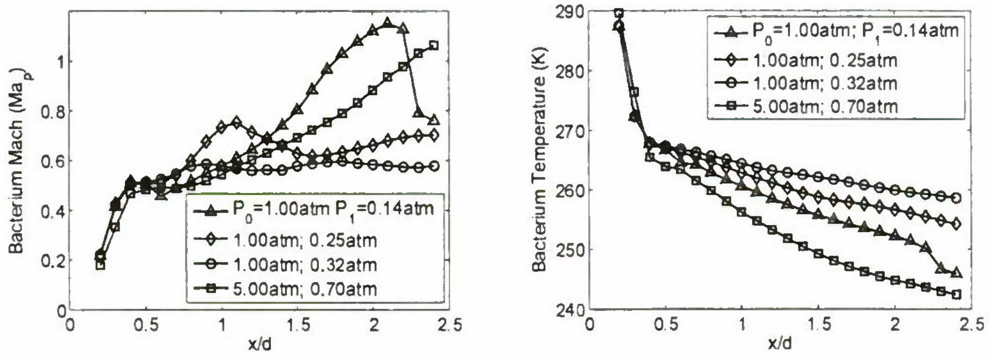

(a) (b)

Figure 3.1: (a) Maximum centerline Mach number and (b) minimum centerline temperature of the particle, as a function of the normalized distance between the nozzle and the plate (x/d) for four different (P_0, P_1) pairs.

Figures 3.2-c and 3.2-d. The instabilities in the flow can be seen in Figure 3.2-b where the centerline gas velocity assumes a negative velocity because of the recirculation bubble. The particle stops at the point where the gas velocity is zero (see Remark 5 for more details). In Figure 3.3, x/d and P_1/P_0 are held constant at 1.4 and 0.14, respectively, while P_0 assumes two values 1 atm and 5 atm. Although the maximum centerline Mach numbers were the same for both cases (see Figure 2.9-a), the gas velocity drop and mean free path are different. The drop from maximum gas velocity to 100 m/s occurs over a length of 150 μm and 240 μm for $P_0 = 1$ atm and $P_0 = 5$ atm, respectively. This will affect the forces experienced by the bacterial particles as they go through the impactor system (see Section 3.3 below).

Remark 4 *The computational analysis of the impactor revealed a maximum Biot number of 0.31 (x/d = 0.5, P_0 = 5 atm and P_1 = 0.7 atm) using the following*

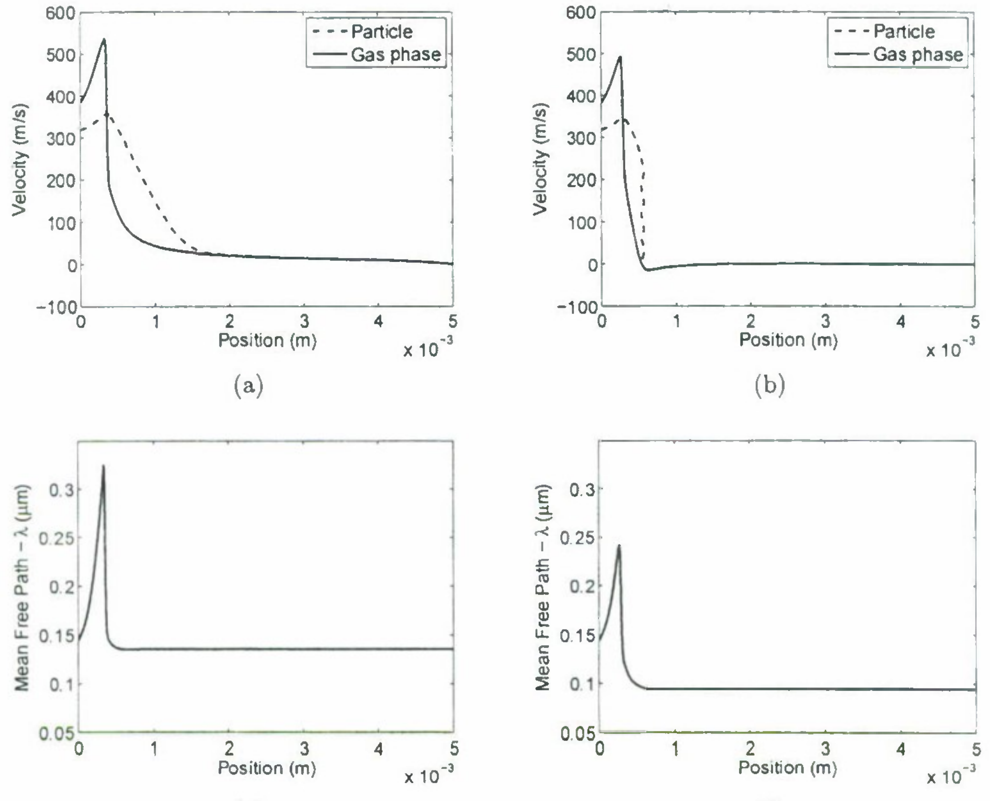

(a) (b)

(c) (d)

Figure 3.2: (a, b) Centerline particle and gas velocity as a function of the distance from the nozzle. (c, d) Mean free path of the gas molecules as a function of distance along the centerline with 0m marking the exit of the nozzle. Conditions: (a, c) $x/d = 1.0$, $P_0 = 1$ atm and $P_1 = 0.14$ atm, (b, d) $x/d = 1.0$, $P_0 = 1$ atm and $P_1 = 0.25$ atm.

formula [26]

$$Bi = \frac{hd_p}{6k_p}, \tag{3.5}$$

where k_p is thermal conductivity of the bacterium and is given by Datta to be 0.44 *W/m K [12]. Although the maximum Biot in the parametric study is greater than 0.1, it is still well less than 1, and thus, equation 3.3 is a good approximation since the internal resistance to heat transfer is well less than the external one.*

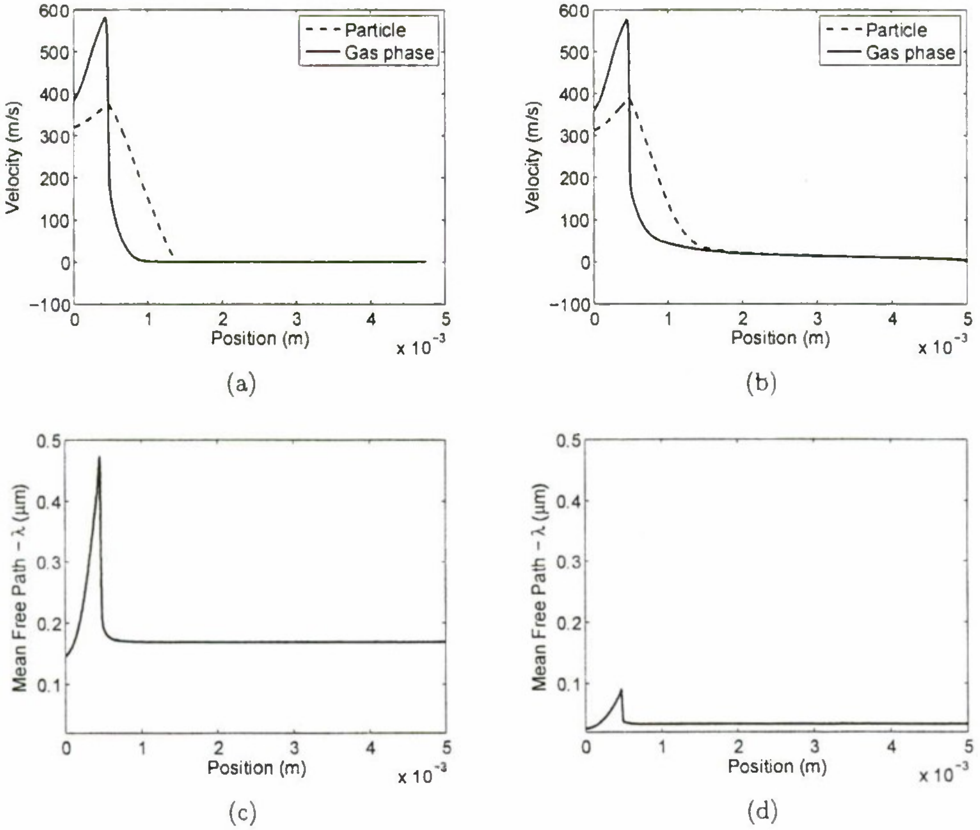

Figure 3.3: (a, b) Centerline particle and gas velocity as a function of distance from the nozzle. (c, d) Mean free path of the gas molecules as a function of distance along the centerline with 0 m marking the exit of the nozzle. Conditions: (a, c) $x/d = 1.4$, $P_0 = 1$ atm and $P_1 = 0.14$ atm, (b, d) $x/d = 1.4$, $P_0 = 5$ atm and $P_1 = 0.70$ atm.

Remark 5 *In the unstable flow conditions (i.e., presence of recirculation bubbles in the flow-field) discussed in Section 2.3.2, the use of Equations 3.2a and 3.2b does not capture the particle behavior in the experimental impactor system. Specifically, in this case, the computations reveal that the particles stop before reaching the collection plate and in some cases before entering the deceleration tube. This type of behavior arises because of the negative velocities of the gas on the centerline caused by the recirculation bubble. Furthermore, the particle motion Equations 3.2a and 3.2b do not account for* *forces such as gravity, Brownian motion, and turbulent dispersion which may need to be included to improve the accuracy of the particle motion trajectories calculations at unstable flow conditions. The effects of Brownian motion and turbulent dispersion on the particle trajectories and accelerations will be the subject of future work. To study these forces more detailed simulations are necessary where a cloud of particles is released from the centerline and average properties are calculated.*

3.3 Bacterial envelope instability

Instabilities in the bacterial membrane arise if the bacterial particle is accelerated (or decelerated) in a perpendicular direction to the bacteria-gas interface (direction parallel to the centerline x-direction) and are referred to as Rayleigh-Taylor instabilities [7, 28]. The relative acceleration creates waves in the surface of the bacteria with characteristic wavelengths. These waves can grow uncontrollably if not for the stabilizing effect of surface tension. However, once a critical wavelength is reached, surface tension cannot compensate for the growth of waves on the bacterial surface and the bacterium breaks up. This phenomenon has been studied extensively by Chandrasekar [7] and Joseph [28]. Specifically, a bacterium is predicted to break up if

$$d_p > \lambda_c = 2\pi\sqrt{\frac{\sigma}{\rho_p a_c}} \tag{3.6}$$

where λ_c is the critical wavelength and is directly related to the critical bacterial acceleration a_c. In Equation 3.6, σ is the surface tension, ρ_p is the particle density and d_p is the particle diameter. Other conditions, which have to be satisfied for the critical acceleration to cause a break-up, are expressed in terms of two dimensionless numbers [28]. Specifically,

$$We > We_c = 12(1 + 1.077Oh^{1.6}) \tag{3.7a}$$

where

$$We = \frac{\rho_g (v_{p_x} - v_{g_x})^2 d_p}{\sigma} \tag{3.7b}$$

and

$$Oh = \frac{\mu_p}{(\rho_p d_p \sigma)^{1/2}} \tag{3.7c}$$

where We is the Weber number, which is the ratio between the inertial force exerted on the bacterial particle and the particle surface tension force. Oh refers to the Ohnesorge number, which is the ratio between the viscous forces and the surface tension force. v_{p_x} and v_{g_x} are the particle and gas velocity in the x-direction, respectively. We can therefore infer bacterial membrane break-up by computing the relative velocity $(v_{p_x} - v_{g_x})$ of the bacterium, as well as the maximum acceleration achieved. Since the particle grid and the gas grid do not coincide, the gas velocity is linearly interpolated to obtain data at the specific positions where the particle velocity is calculated. Specifically, the relative velocity is then numerically differentiated with respect to time to give the maximum acceleration as follows:

$$v_{g_{x_j}} = \frac{v_{g_{x_i}} - v_{g_{x_{i+1}}}}{t_i - t_{i+1}}(t_j - t_i) + v_{g_{x_i}}, \quad \forall \; t_j \in [t_i, t_{i+1}], \tag{3.8a}$$

and

$$a_{max} = \max_j \left| \frac{(v_{g_{x_{j+1}}} - v_{p_{x_{j+1}}}) - (v_{g_{x_j}} - v_{p_{x_j}})}{t_{j+1} - t_j} \right|, \tag{3.8b}$$

where i and j are the indices of gas and particle grid points, respectively, and t_i and t_j are the times at the grid point i and j, respectively. Only grid points between the nozzle exit and the deceleration tube entrance are considered in the calculation of the maximum acceleration in the x-direction.

Table 3.1: Biological cell diameter and surface tension [61] (not limited to bacteria)

Cell	d_p (μm)	σ (N/m)
E. coli	1	7.5×10^{-3}
D. carota	60	4.5×10^{1}
M. hungatei	0.44	$3.5 - 5$
C. eugametos	16	3.8×10^{1}
B. Emersonii	20	3.2×10^{1}

Table 3.2: Critical shock properties needed to induce bacterial break-up for different biological cells. The maximum Weber number is calculated for 1 μm particles (see Remark 6)

Cell	a_c (m/s^2)	Oh	We_c	We_{max}
E. coli	3.0×10^{8}	3.7×10^{-1}	1.4×10^{1}	2.9×10^{1}
D. carota	4.9×10^{8}	6.1×10^{-4}	1.2×10^{1}	3.0×10^{-1}
M. hungatei	$0.7 - 1.0 \times 10^{12}$	$2.1 - 2.5 \times 10^{-2}$	1.2×10^{1}	$2.0 - 2.8 \times 10^{-2}$
C. eugametos	5.9×10^{9}	1.3×10^{-3}	1.2×10^{1}	9.4×10^{-2}
B. Emersonii	3.2×10^{10}	1.3×10^{-3}	1.2×10^{1}	1.4×10^{-1}

Figure 3.4 shows the acceleration of the bacterial particles relative to the gas stream. The bacterial envelope becomes unstable at a critical acceleration ($a_c = (4\pi^2\sigma)/(\rho_p {d_p}^2)$) which depends on the surface tension, density and diameter of the bacterium. The values of a_c for different bacteria are shown in Table 3.1 along with the Weber and Ohnesorg numbers. If the maximum calculated Weber number in the impactor system (We_{max}), exceeds the critical Weber number We_c, then conditions are satisfied to achieve bacterial break-up at the critical accelerations (a_c). Spores (i.e., properties similar to *M. hungatei*) have a higher surface tension (lower We_{max} and higher a_c) than vegetative cells (i.e., *E. coli*) and hence, they are more difficult to damage mechanically. Table 3.1 indicates that all of the cells except *E. coli*, does not satisfy the critical Weber number requirement; basically, the cells do not achieve the energies needed for break-up. The computational results shown in Figure 3.5

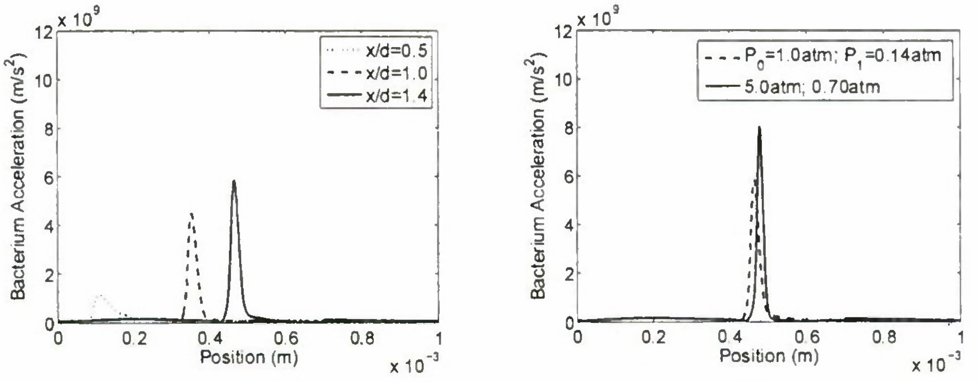

(a) (b)

Figure 3.4: Bacterial particle acceleration (relative to gas flow) as a function of distance from the nozzle outlet. (a) The operating conditions are constant for all three curves at $P_0 = 1$ atm and $P_1 = 0.14$ atm. The x/d varies for each case from 0.5 to 1.4. (b) The x/d is held constant at 1.4 as well as P_1/P_0 at 0.14. The acceleration is higher for the case where $P_0 = 5$ atm.

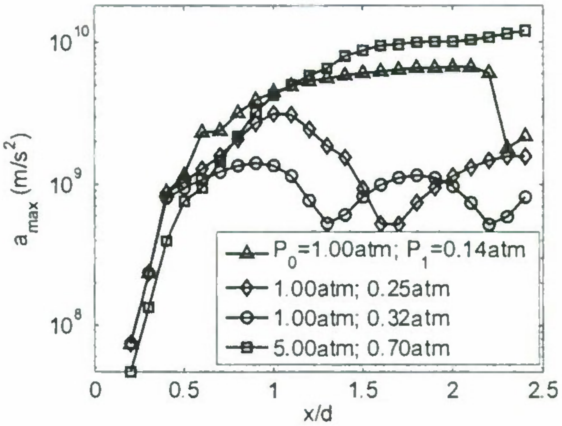

Figure 3.5: Maximum centerline acceleration of the particle as a function of normalized distance between the nozzle and the plate (x/d) for four different (P_0, P_1) pairs.

indicate that the maximum accelerations achieved in the developed experimental impactor system are on the order of $10^9 - 10^{10}$ m/s^2 including data for a wide range of x/d values. Comparing this data with the critical accelerations in Table 3.1, we can predict the possibility of break-up of certain bacterial particles in the experimental impactor system. For example, *E. coli*, a vegetative gram-negative bacterium, requires an acceleration of 3.0×10^8 m/s^2 and we, therefore, predict that the experimental impactor is capable of neutralizing this bioaerosol. On the other hand *M. hugatei*, an archaea, (see Chapter 5 for *B. atropheus* data) requires an acceleration of 1.0×10^{12} m/s^2 which can not be achieved by the developed experimental impactor system.

Remark 6 *Particle size affects the relative velocity between the bacterial particle and the gas, which leads to a change in the Weber number. In this work, the Weber number of a* 0.5 μm *bacterial particle was compared to that of a* 1.0 μm *bacterial particle at*

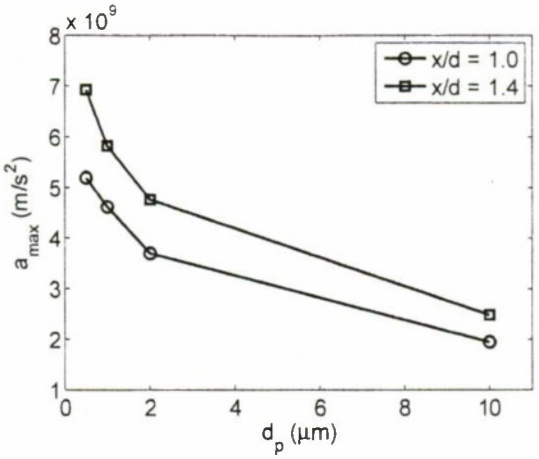

Figure 3.6: Maximum centerline acceleration of the particle as a function of the particle size in impactor system operated at $P_0 = 1$ atm and $P_1 = 0.14$ atm for two values of x/d.

$P_0 = 1$ atm, $P_1 = 0.14$ atm and $x/d = 1.4$. The difference in value was $\approx 5\%$, which is not significant considering that the maximum Weber number of M. hungatei ($d_p = 0.44$ μm) is much smaller than the critical one (see Table 3.1). The a_{max} values also change with different particle sizes as shown in Figure 3.6. However, these changes are not significant since they are of the same order of magnitude.

3.4 Conclusions

The computational fluid dynamics model of the experimental impactor system of Figure 2.1 developed in Chapter 2 was used to predict the evolution of both the gas and particle velocity and temperature profiles in the impactor system. For this chapter these profiles were used to compute the critical acceleration needed to break-up different bacterial aerosols using the Rayleigh-Taylor instability equations. Our models predict that the bacterial accelerations achieved in the impactor system of Figure 2.1 are on the order of $10^9 - 10^{10}$ m/s^2 for various conditions of x/d, P_0 and P_1. Certain bacterial aerosols which have critical accelerations less than the ones computed in the impactor system are predicted to break-up.

Chapter 4

Effect of Aerodynamic Shock on *E. coli*

4.1 Introduction

The computational model developed in Chapter 3 predicts the break-up of *E. coli* vegetative cells in the impactor system. In order to validate our computational model, *E. coli* cells are aerosolized and passed through the experimental impactor system. Different operating conditions are used in order to validate both break-up and no break-up predictions in the system. Measurements of viability are carried out on dye labeled cells using fluorescence flow cytometry [49].

4.2 Experimental materials and methods

4.2.1 Experimental setup

The impactor system discussed in Chapter 2 was used in the experimental setup and is shown in Fig. 4.1. The bacterial suspension (see Section 4.2.2) is aerosolized using a capillary nebulizer (TR-30-A1, Meinhard Glass Products) at a gas (N_2) critical flow rate of 0.2 L/min (see Fig. 4.1; parts 1 and 2). The impactor (see Fig. 4.1; parts 3 thru 8) operates at a critical flow rate of 2.3 L/min at shock conditions. As shown in Fig. 4.1, a high efficiency particulate air (HEPA) filter is installed between the nebulizer (part 2) and the impactor system (part 3) to allow particle-free air to compensate for the higher impactor flow rate, thereby maintaining the upstream impactor pressure at 1 atm.

Nebulization

The phosphate buffered saline (PBS) (BP2438-4, Fisher Scientific) suspension containing the *E. coli* cells (see Section 4.2.2) is fed via a syringe pump (KDS410, Kd Scientific) at a liquid flow rate $Q = 0.05$ mL/min for 20 min. The liquid is fed at a specified bacterial concentration (see Section 4.2.2) determined by the optical density measurement at $600nm$ (OD_{600}). Nitrogen is supplied to the nebulizer at a pressure P_n via a pressurized tank. When the liquid is mixed with the air in the annular region of the nebulizer tip, droplets containing bacterial cells are formed. The bacterial aerosol concentration and droplet size can be adjusted by changing: Q, OD_{600} and P_n. Increasing Q and decreasing P_n increases the average droplet diameter (and volume). Increasing OD_{600} increases the number of cells per volume of liquid nebulized. Collectively, increasing Q and OD_{600} and decreasing P_n, increases the number of cells per droplet. Q and OD_{600} also increase the number of cells input into the system in a given time. In all the experiments, the nebulizer was operated at $Q = 0.05$ mL/min, $OD_{600} = 0.1$, and $P_n = 2$ atm. The cell concentration at $OD_{600} = 0.1$, as measured using fluorescence flow-cytometry (see Section 4.2.3), was $2.66 \pm 0.28 \times 10^7$ cells/mL. The expected average nebulized droplet size is 10 μm, which translates to about 1 cell in every 1000 droplets assuming that no aggregates are formed in the suspension.

In previous liquid suspension shock studies, it has been shown that an increase in cell concentration results in an increase in bacterial viability [40]. The controlled bacterial nebulization process produces individual cells suspended in air that can pass isolated through the shock, thereby avoiding the concentration effect seen in liquid suspension studies.

Impactor system

The impactor system consists of a plate designed for the collection of the bacterial aerosol (see Fig. 4.1; parts 4 and 5) which is placed perpendicular to the gas flow emerging from a converging nozzle (see Fig. 4.1; part 3). Isentropic flow theory of an ideal gas predicts a critical downstream (P_1) to upstream (P_0) pressure ratio below which the flow at the exit of the nozzle is sonic [38, 48], according to the following equation:

$$\chi_{crit} = (P_1/P_0)_{crit} = [2/(\gamma+1)]^{\gamma/(\gamma-1)}, \tag{4.1}$$

where γ is the heat capacity ratio ($\gamma = 1.4$; $\chi_{crit} = 0.53$ for N_2). The generated impinging flow on a plate from a converging nozzle operating under sonic conditions results in the creation of a standoff shock whose properties can be changed by varying impactor geometry (distance between nozzle and plate x and diameter of nozzle d) and operating conditions [2, 13, 14, 29, 42, 51]. In traditional impactors [21, 22], the aerosol is collected by impaction on a flat surface. Stewart et al. (1995) showed that bacteria collected by impaction are injured [53]; therefore, assessing damage induced by the standoff shock is impossible using current impactor designs. To avoid loss of viability by impaction, the flat surface of the developed impactor system has a central opening (see Fig. 4.1; part 4) that acts as a virtual surface through which the bacteria enter a stagnant gas deceleration tube (see Fig. 4.1; parts 4 and 5). Biswas and Flagan (1988) have designed a similar tube to prevent particle reentrainement [4]. Computational results (see Chapters 2 and 3) indicate that the bacteria are collected at low impact velocities (< 10 m/s) in the deceleration tube and consequently will not be injured due to impaction. The distance between the opening of the deceleration tube and the nozzle outlet (x) can be adjusted with spacers of different thickness (see Fig. 4.1; part 6). In the current experimental study, the spacer is 1.4 mm thick. A valve attached to a purge stream downstream of the impactor, controls P_1, whereas

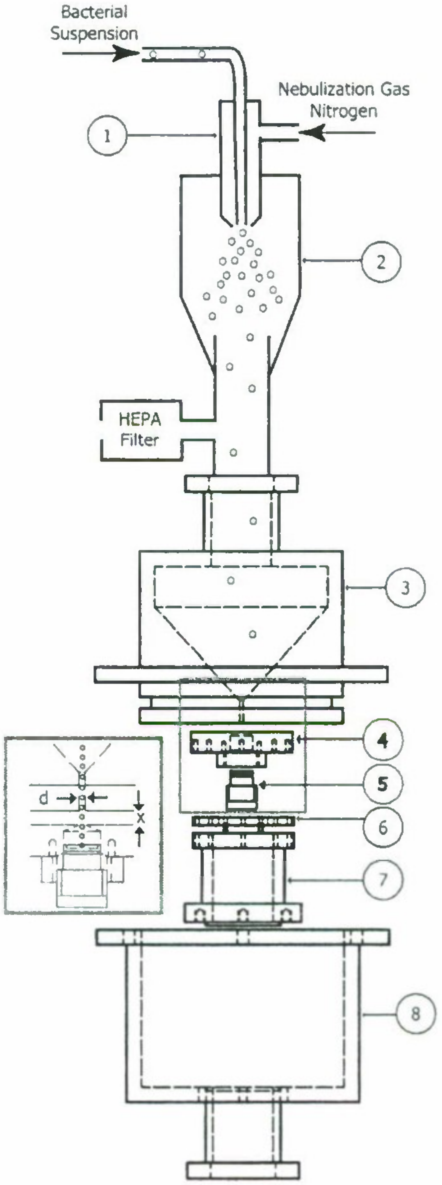

Figure 4.1: Schematic of the experimental system. (1) Meinhard nebulizer with a concentric nozzle mixing a liquid bacterial suspension feed and a dispersion gas (N_2), (2) Nebulization chamber to collect large droplets, (3) Converging nozzle with an exit diameter of $d = 0.5$ mm, (4) and (5) a flat surface with a 0.5 mm hole combined with a screw that accommodates the collection substrate make up the deceleration tube, (6) 1.4 mm spacer fixes the spacing x between the impactor and nozzle to 0.6 mm, (7) support holding the deceleration tube and flat surface at fixed distance from the nozzle, and (8) exit chamber.

the upstream is left at ambient pressure (1 atm).

The deceleration tube is filled with 600 μL of PBS, which keeps the liquid level to about 4 mm away from the entrance of the deceleration tube. The PBS provides a hydration environment for the collected cells and ensures that the collected cells do not lose viability because of drying (this has been experimentally verified). The impactor system with $x/d = 1.2$ was operated for 20 min at three pressure ratios: $\chi = 0.11, 0.50$ and 0.98. As a control to test any low-pressure effects, 600 μL of bacterial suspension (see Section 4.2.2) at $OD_{600} = 0.01$ was placed in the deceleration tube and the impactor was run with particle-free air for 20 min at the three operating pressures. We experimentally found that cells retain their viability under low pressure conditions when compared with the starting bacterial suspension.

4.2.2 Bacterial cell culture preparation

E. coli K-12 wild-type strain (MG1655) was used as a standard bacterial aerosol to study the effect of aerodynamic shocks on vegetative bacterial cells in the impactor system. All cell cultures were initiated from a stock *E. coli* suspension (80% glycerol solution) stored at −20 °C. 5 mL of Luria Bertani (LB) broth (Fisher) was inoculated with 3 μL of stock suspension in a test tube. The culture was incubated in a shaker (Excella E24, New Brunswick Scientific) at 37 °C at 200 rpm for approximately 16 hrs. Subsequently, 2 mL of culture was centrifuged at 4400 rpm for 5 min (Centrifuge 5702, Eppendorf) and washed ($3X$) with 4 mL PBS. After washing, the optical density of the suspension was measured at a wavelength of 600 nm (OD_{600}) using a visible light spectrophotometer (Genesis 20, Thermo Scientific). The cell suspension was diluted to $OD_{600} = 0.1$ to be used in the experiments described in Section 4.2.1. Another dilution at $OD_{600} = 0.01$ was prepared for suspension flow cytometry measurements, but not nebulized.

Positive and negative controls were prepared and carried out before the start of every experiment. The negative control is the cell suspension in PBS diluted to $OD_{600} = 0.01$ as described above. The negative control serves as the starting point for viability measurements. It is the measurement with most viable cells. The positive control was prepared by centrifuging 2 mL of the cell culture at 4400 rpm and washing with 4 mL 70% ethanol. The ethanol-washed cells were incubated for 15 min at room temperature. The suspension was then centrifuged at 4400 rpm and washed (2×) with 4 mL PBS. The positive control was then diluted to $OD_{600} = 0.01$. The effect of aerodynamic shock was then compared to a standard ethanol disinfection method (positive control) used in liquid suspension.

4.2.3 Bacterial viability analysis

Bacterial viability is determined using LIVE/DEAD®*Bac*Light^{TM} (cat. number L7012; Life Technologies Corporation) [3, 32]. The assay contains two components: (A) 3.34 mM STYO 9, a green-fluorescent nucleic acid stain, in dimethyl sulfoxide (DMSO) and (B) 20 mM propidium iodide (PI), a red-fluorescent nucleic stain, in

DMSO. STYO 9 penetrates both intact and damaged membranes, while PI only penetrates damaged membranes. A stock dye solution is prepared at the start of every experiment by mixing 5 μL of each of components A and B with 10 μL PBS. All controls and experimental samples mentioned in Sections 4.2.1 and 4.2.2 were stained with the stock dye solution to a final concentration of 8.35 μM and 50 μM of STYO 9 and PI, respectively.

The stained samples were analyzed using a fluorescence flow cytometer (FACScan^{TM}, BD Biosciences). The cytometer was operated at 12 μL/min for 20 s with a 488 nm excitation laser. Red fluorescence was measured with a high pass filter at 630 nm (FLH-2) and green fluorescence was measured at a bandpass of 520 nm (FLH-1). The forward scatter (FSC) and side scatter (SSC) were also measured for the particles passing the laser. Photomultiplier tubes were used to amplify the optical signal for FLH-1, FLH-2 and SSC at 850, 800 and 375 volts, respectively. A photodiode was used to detect the FSC signal.

4.2.4 Mass balance analysis

A 0.2 μm black polycarbonate filter (Millipore) was placed in an in-line 25 mm filter holder inserted after the nebulization chamber and before the HEPA filter of the experimental setup shown in Fig. 4.1. After running the experiment for 20 min, the filter was placed in a Millipore filter holder and 1 mL of STYO 9 stock was passed through the filter staining all cells. After staining, the filter was placed on a microscope slide and 5 μL of mounting oil (cat. number L7012; Life Technologies Corporation) was added to the surface of the filter, and covered with a glass slip. Images of the filter were taken with a fluorescence microscope at an objective lens magnification of 40× (Zeiss). Each image represents a filter area of 3.8×10^4 μm^2. Images of 10 randomly selected areas on the filter were taken to get an average cell count per image area, which was then multiplied by the total area of the filter to get the total number of cells collected on the in-line filter. A total of 7 independent experiments with different starting cell cultures were carried out. The cells collected on the filter were assumed to be equal to the cells entering the impactor system. Fig. 4.2-b shows a sample image of bacterial aerosol collected on a filter before the impactor entrance and stained with STYO 9. Fig. 4.2-a is an image from OD_{600} = 0.01 PBS *E. coli* suspension and is shown for comparison. We can see that both

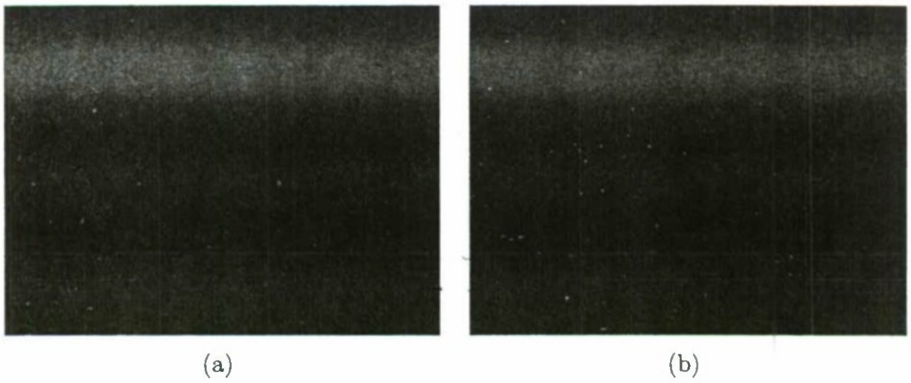
(a) (b)

Figure 4.2: Fluorescence microscopy images taken at 40X objective lens with an area of 3.8×10^4 μm^2. The cells are stained with STYO 9 dye which penetrates both live and dead cells. The images are taken for counting purposes and not for determination of cell viability. (a) image of *E. coli* from cell suspension in PBS at OD_{600} = 0.01 on a polycarbonate filter. (b) image of nebulized *E. coli* collected on an inline filter between the nebulizer and the entrance of the impactor system operated at a flowrate of 2.3 L/min for 20 min.

Fig. 4.2-a and b have a single layer of cells and can be therefore easily be counted.

4.3 Computational results

4.3.1 Gas flow field and particle dynamics

For the two-phase aerosol flow (air-bacteria) present in the impactor system, the equations for gas and particle dynamics are one-way coupled at low aerosol concentrations [18]; the existence of aerosol has little effect on the gas while the aerosol flow is determined by the gas velocity. Therefore, the gas dynamics are solved independently using the Reynolds time-averaged Navier-Stokes equations shown in Cartesian tensor form:

$$\frac{\partial \rho}{\partial t} + \frac{\partial}{\partial x_j}(\rho v_j) = 0, \tag{4.2}$$

and

$$\begin{aligned} &\frac{\partial}{\partial t}(\rho v_i) + \frac{\partial}{\partial x_j}(\rho v_i v_j) \\ &= -\frac{\partial p}{\partial x_i} + \frac{\partial}{\partial x_j}\left[\mu\left(\frac{\partial v_i}{\partial x_j} + \frac{\partial v_j}{\partial x_i} - \frac{2}{3}\delta_{ij}\frac{\partial v_l}{\partial x_l}\right)\right] + \frac{\partial}{\partial x_j}(-\rho\overline{v_i' v_j'}), \quad i = 1, 2, 3, \end{aligned} \tag{4.3}$$

where ρ is the density, v is the velocity, p is the static pressure, δ is the Kronecker delta, μ is the viscosity, and i, j, and l are the cartesian indices. To close the form in Eq. 4.3, the Reynolds stress term $-\rho\overline{v_i' v_j'}$ is calculated using the Boussinesq hypothesis [24]. A standard $k - \epsilon$ turbulence model is used in the gas flow equations.

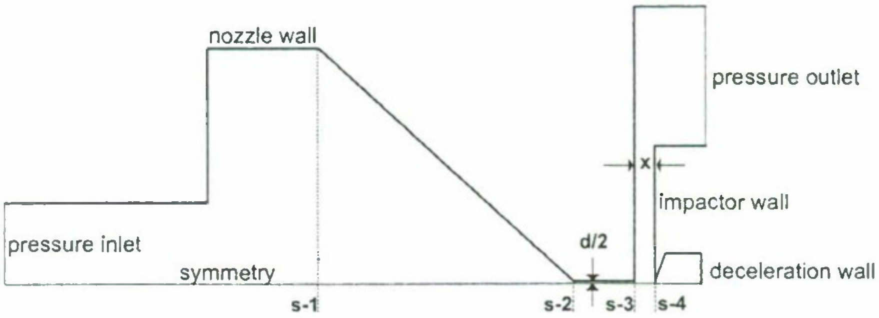

Figure 4.3: Computational domain of the impactor. The dashed lines indicate different virtual surfaces. These surfaces are used to calculate the particle distribution at various cross-sections of the impactor shown as S-1, S-2, S-3 and S-4.

The computational model details used to solve both gas and particle dynamics (flow and temperature) for the computational domain shown in Figure 4.3 are discussed in Chapter 2 and 3 [51]. In this Chapter, temperature effects are not analyzed. After obtaining the gas flow field, the particle trajectory is solved using Newton's second law:

$$m_p \frac{dv_p}{dt} = \frac{1}{2} C_D \rho_g A_p (v_g - v_p) |v_g - v_p|, \tag{4.4a}$$

$$\frac{dx}{dt} = v_p, \tag{4.4b}$$

where v_p and v_g are the velocity of the bacterial particle and gas, respectively, m_p is the mass of the particle, ρ_g is the density of the gas, A_p is the projected area of the bacterium on the plane perpendicular to the flow direction, and C_D is the drag coefficient. The thermophoretic, gravitational, and Basset history term are neglected in Eq. 4.4a. The drag force is assumed to be the major force acting on the bacterial particle which is typical for impactor systems. The bacterium is simulated as a 1 μm sphere with a density ρ_p of 1 g/mL which is representative of values reported in literature [33, 59]. All calculations are made to mimic the experimental conditions in the study with the $x/d = 1.2$ and both shock ($\chi = P_1/P_0 = 0.11, 0.50$) and non-shock ($\chi = 0.98$) conditions. The detailed conditions are shown in Section 4.3.3. The computational results provide predictions for bacterial envelope instability (see Section 4.3.2) and the collection efficiency of the impactor system at different operating conditions (see Section 4.3.3).

4.3.2 Bacterial envelope instability

The acceleration (or deceleration) of a bacterium relative to the gas phase creates instabilities in the bacterial envelope and break-up of the particle [7, 28, 51]. Specifically, waves are created on the bacterial surface perpendicular to the direction of acceleration (x-direction) which are stabilized by the bacterial surface tension. Under the assumption of viscous potential flow around a spherical cell, an estimate of the critical acceleration needed to overcome the stabilizing effect of surface tension can be computed using the derivation in [28] (see also Chapter 10 of [7]) as follows:

$$a_c = 4\pi^2 \frac{\sigma}{\rho_p d_p^2} \tag{4.5}$$

where σ is the surface tension, ρ_p is the particle density and d_p is the particle diameter. Other sufficient conditions, which have to be satisfied for the critical acceleration to cause a break-up, are expressed in terms of two dimensionless numbers [28]. Specifically,

$$We > We_c = 12(1 + 1.077Oh^{1.6}) \tag{4.6a}$$

where

$$We = \frac{\rho_g (v_{p_i} - v_{g_i})^2 d_p}{\sigma} \tag{4.6b}$$

and

$$Oh = \frac{\mu_p}{(\rho_p d_p \sigma)^{1/2}} \tag{4.6c}$$

where We is the Weber number, which is the ratio between the inertial force exerted on the bacterial particle and the particle surface tension force. Oh refers to the Ohnesorge number, which is the ratio between the viscous forces and the surface tension force. v_{p_i} and v_{g_i} are the particle and gas velocity in the x-direction (i.e. direction of flow along centerline), respectively. We can therefore infer bacterial membrane break-up by computing the relative velocity $(v_{p_i} - v_{g_i})$ of the bacterium, as well as the maximum acceleration achieved (see Chapter 3). The criteria that both deceleration and Weber number have to be above the critical values are sufficient for the bacterial cell to break-up as they pass through the shock. However, if only the Weber number is above its critical value the cells may experience membrane vibrations, boundary layer stripping, or even break-up [28]. Furthermore, the model does not account for loss of viability without break-up which is a more stringent requirement than other mechanisms.

Bacterial cells with a lower surface tension and larger diameters require lower

Table 4.1: Biological cell properties [61] (not limited to bacteria) and critical shock properties needed to induce bacterial break-up.

Cell	d_p (μm)	σ (N/m)	a_c (m/s^2)	Oh	We_c
E. coli	1	7.5×10^{-3}	3.0×10^{8}	3.7×10^{-1}	14
D. carota	60	4.5×10^{1}	4.9×10^{8}	6.1×10^{-4}	12
M. hungatei	0.44	$3.5 - 5$	$0.7 - 1.0 \times 10^{12}$	$2.1 - 2.5 \times 10^{-2}$	12
C. eugametos	16	3.8×10^{1}	5.9×10^{9}	1.3×10^{-3}	12
B. Emersonii	20	3.2×10^{1}	3.2×10^{10}	1.3×10^{-3}	12

accelerations to break-up. It is important to note that the surface tension values reported in Table 4.1 are derived from the turgor pressure [61]. However, the surface tension can vary with deformation generated by fluid flow over the cell membrane. Such a variation of the cell surface tension under fluid flow may limit the accuracy of the critical acceleration predictions of Table 4.1. In such a case, more accurate models of the variation of cell surface tension under stress generated by the fluid flow (similar to the works of [30, 31, 52, 60]) should be utilized and combined with the fluid flow and particle motion models developed here to make accurate critical acceleration predictions. We also note that previous work [31] has demonstrated for the first time the use of inertial forces (expressed in terms of the Weber number and acceleration) in achieving cell break-up in the context of a high-pressure homogenization system. As shown in Table 4.1, vegetative cells represented by *E. coli* require critical accelerations (a_c) of 3.0×10^8 m/s^2. On the other hand, spores represented by *M. hungatei*, an archea, require accelerations of about four orders of magnitude more than vegetative cells. In our previous parametric study of the impactor system [51] where P_1, P_0 and x/d were varied, it was shown that we can achieve accelerations on the order of

$10^9 - 10^{10}$ m/s^2 in our current system operating under shock conditions. Furthermore, it is possible to achieve accelerations below 10^8 m/s^2 by operating the impactor at non-shock conditions.

A shock is represented as a sharp discontinuity in fluid properties (velocity, temperature, pressure) and can be seen in Figure 4.4-a. Due to its inertia, a bacterial particle is not able to follow the sharp drop in gas velocity and will therefore experience a relative deceleration of 4.95×10^9 m/s^2 at $\chi = 0.11$ and 2.02×10^8 m/s^2 at $\chi = 0.50$ (both above the critical acceleration of *E. coli*). However, in the non-shock condition with $\chi = 0.98$ (see Figure 4.4-b) the gas properties do not experience sharp changes. In the incompressible flow the gas decelerates because of the larger area due to the expansion after exiting the nozzle. The bacterial particle is, therefore, able to adjust to the gas velocity and experience a much lower relative deceleration of 3.89×10^6 m/s^2. The deceleration of the bacterial particle in the non-shock case is not large enough ($< 3.0 \times 10^8$ m/s^2, see Table 4.1) to cause the break-up of the cell envelope. Figures 4.4-c and d show the acceleration of the bacterial particle as a function of the distance from the exit of the nozzle. In the shock case with $\chi = 0.11$, the peak acceleration lasts for a short distance and is 3 orders of magnitude larger than the non-shock case. We therefore operated the impactor system at both the shock ($\chi = 0.11, 0.50$) and non-shock ($\chi = 0.98$) conditions to obtain, in addition to the computational data, experimental bacterial viability data (see Section 4.4).

Remark 7 *At* $\chi = 0.98$, *the acceleration of the bacterial particle shown in Fig-*

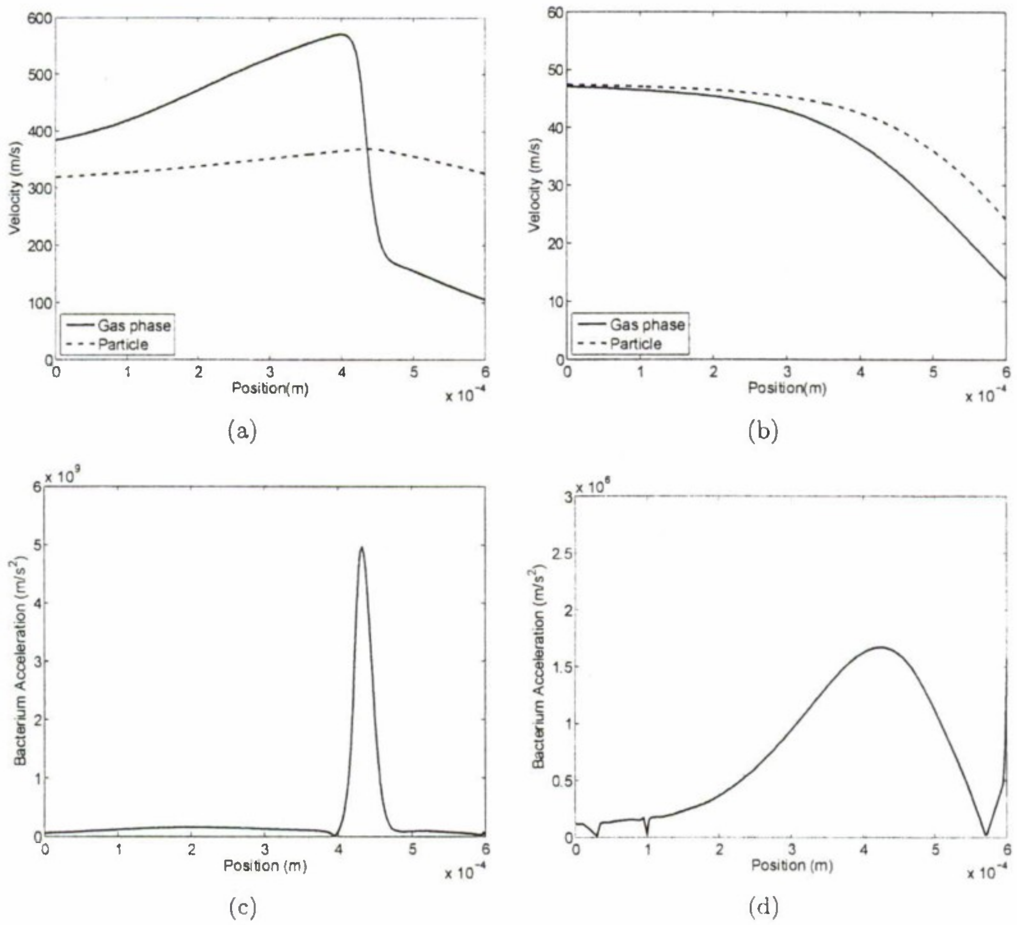

(a) (b) (c) (d)

Figure 4.4: (a, b) Centerline particle and gas velocity and (c,d) Bacterial particle acceleration (relative to gas flow) as a function of the distance from the nozzle. The entrance of the collection tube is at a distance 6×10^{-4} m from the nozzle exit. Impactor operating conditions: (a,c) $\chi = 0.11$ and (b,d) $\chi = 0.98$.

ure 4.4-d experiences a sharp change at a position greater than 0.55 *mm from the exit of the nozzle. The change is because of the stagnant gas at the entrance of the deceleration tube, especially since Brownian motion is neglected in these calculations. The maximum acceleration is calculated at a position approximately* 0.4 *mm from the nozzle.*

Remark 8 *The particle accelerations were calculated by tracking a bacterium released on the centerline of the impactor, where the aerodynamic shock has the highest Mach number. Therefore, the calculated bacterial accelerations represent a maximum in a distribution if the particle accelerations were to be calculated at all points. These off-centerline accelerations can represent values lower than the critical value of* $3.0 \times 10^8\ m/s^2$ *required to break-up the E. coli cells. In the experiments, the E. coli cells will experience the distribution of accelerations. Therefore, we do not expect all cells to lose viability, especially since they pass the shock at different points as explained in Section 4.3.3.*

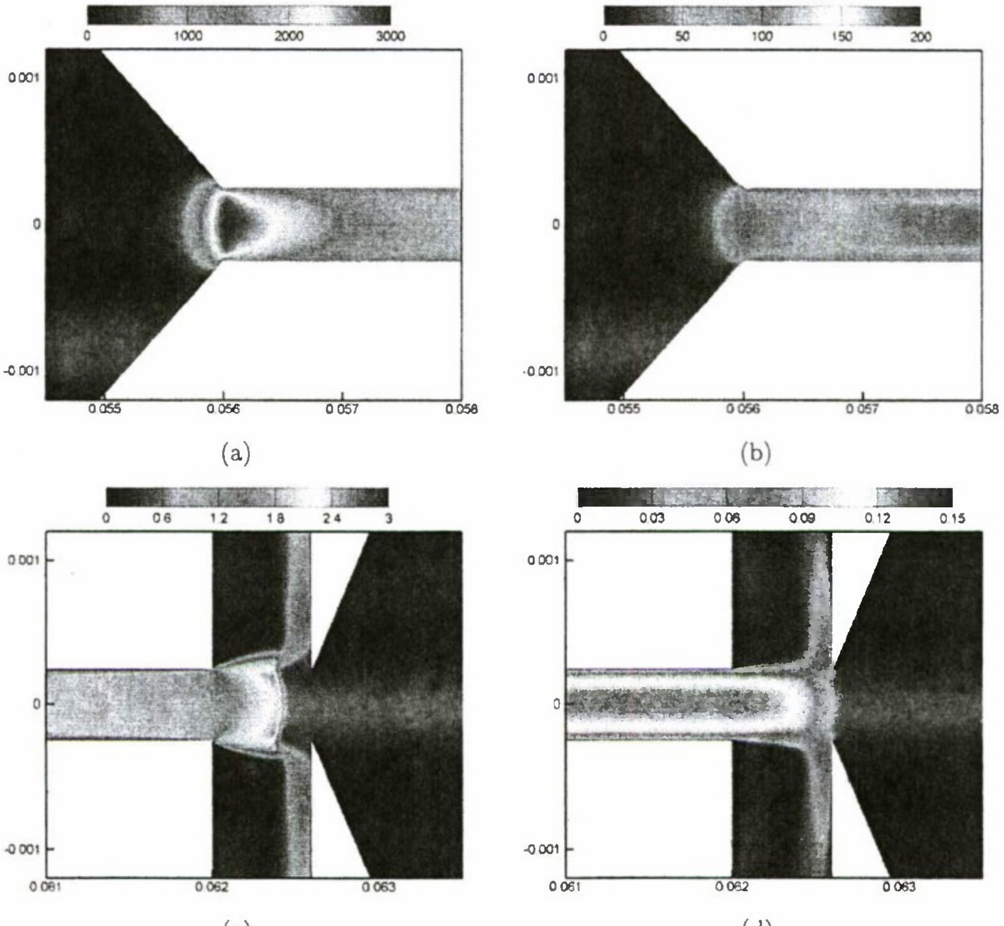

(a) (b)

(c) (d)

Figure 4.5: (a,b) Turbulent kinetic energy (m^2/s^2) contours of the gas phase in the converging region of the nozzle. A region of high turbulence can be seen in the converging part. (c,d) Mach contours at the exit of the nozzle. Conditions: (a,c) shock with $\chi = 0.11$ and (b,d) non-shock with $\chi = 0.98$. Note that the scales are different for the different conditions.

4.3.3 Bacterial collection efficiency in the impactor

The collection efficiency (η) is defined as the number of particles that pass through the collection tube entrance versus the number of particles that enter the impactor inlet. The bacterial collection efficiency (η) for all three impactor operating conditions ($\chi = 0.11, 0.50, 0.98$) are evaluated to determine the overall bacterial aerosol neutralization rate in Section 4.4. For a highly turbulent flow (see Fig. 4.5-a, b) and low-density, small-size aerosols, particle dispersion due to gas velocity fluctuations could be significant and should be accounted for in the calculation of collection efficiency. The gas dynamics, described in Section 4.3.1, is based on a turbulent model and only provides a Reynolds-averaged velocity while the velocity fluctuation terms are not explicitly described. The random walk model is employed in this work to study the effect of velocity fluctuation on bacterial aerosol with reasonable computational load. Stochastic tracking of the particles is used in order to account for the turbulence dispersion effects of the gas flow. In Section 4.3.2, the average values of the gas velocity were used to evaluate the maximum relative acceleration of the particles on the centerline. In the stochastic tracking model, however, the gas velocity is represented as an average plus a fluctuating term when calculating the particle velocity, v_p, in Equation 4.4a. The fluctuating velocity is kept constant for time intervals corresponding to the lifetime of the eddies. The following equations describe the stochastic behavior:

$$v_g = \overline{v} + v' \tag{4.7a}$$

$$v' = \zeta\sqrt{\overline{v'^2}} = \zeta\sqrt{2k/3} \tag{4.7b}$$

$$t_L = 0.15k/\epsilon \tag{4.7c}$$

$$\tau_\epsilon = -t_L log r \tag{4.7d}$$

where v_g is the instantaneous gas velocity, $\overline{v}$ is the average velocity, and v' is the velocity fluctuation term. v' is a function of ζ, a normally distributed random number, and $\overline{v'^2}$ is the local mean square of the fluctuations. $\overline{v'^2}$ is calculated based on the assumption of isotropy and is given by $\overline{v'^2} = 2k/3$, with k being the turbulence kinetic energy in the $k - \epsilon$ model. Finally, t_L is the lagrangian time interval, ϵ is the turbulence dissipation rate, τ_ϵ is the lifetime of the eddies, and r is a uniformly distributed random number between 0 and 1. Fig. 4.6 shows the path of 5 particles released from the inlet as they exit the nozzle of the impactor system for both $\chi = 0.11$ (Fig.4.6-a) and $\chi = 0.98$ (Fig.4.6-b). In calculating η, $10,000$ particles are released at the inlet of the impactor. The particles are then counted as they pass the different virtual surfaces shown in Fig. 4.3 as $s-1$, $s-2$, $s-3$ (nozzle exit) and $s-4$ (deceleration tube entrance) (see Remark 9). All the boundaries shown in Fig. 4.3, except pressure inlet and pressure outlet, are assumed to be reflection boundaries. The collection efficiency is defined as follows:

$$\eta = \frac{n'_c}{n_i} \tag{4.8}$$

where n_i is the number of particles entering the impactor (see also Remark 9) and n'_c is the number of particles that enter the collection tube. n'_c is calculated under the assumption of no break-up. η is used to determine the total number of live cells that would be collected if the shock were to have no effect (see Section 4.4.2). For different operating conditions, the collection efficiency (η) is reported in Table 4.2. The maximum acceleration (a_{max}) and Weber number (We_{max}), which enable the prediction of the experimental break-up, are also reported in Table 4.2. The critical acceleration conditions that satisfy the requirements for break-up as discussed in Section 4.3.2 are met for $\chi = 0.11$ and 0.50; however, the conditions for the Weber number are not. Increasing the upstream pressure to 5 atm will increase the We to 15 while keeping the maximum acceleration similar as shown in Table 4.2. However, as reported in Section 4.4.2, cells will still break-up under non-critical Weber number conditions. The Reynolds number at the exit of the nozzle and the maximum Mach number of the gas are also reported to give insight into the flow characteristics of the impactor. The effect of these different conditions is described in detail in Section 4.4.

Table 4.2: Critical parameters for different operating conditions with $x/d = 1.2$

P_0 (atm)	$\chi(= P_1/P_0)$	a_{max} (m/s^2)	We_{max}	M_{max}	Re	η
1.0	0.98	1.67×10^6	1.7×10^{-2}	0.13	9.9×10^2	0.35
1.0	0.50	2.02×10^8	3.5×10^0	0.96	5.8×10^3	0.72
1.0	0.11	4.96×10^9	3.1×10^0	2.36	5.4×10^3	0.51
5.0	0.11	5.98×10^9	1.5×10^1	2.32	3.2×10^4	0.38

Remark 9 *Despite the reflective boundary conditions employed in the simulations, not all* 10,000 *particles released from the inlet of the impactor are accounted for at*

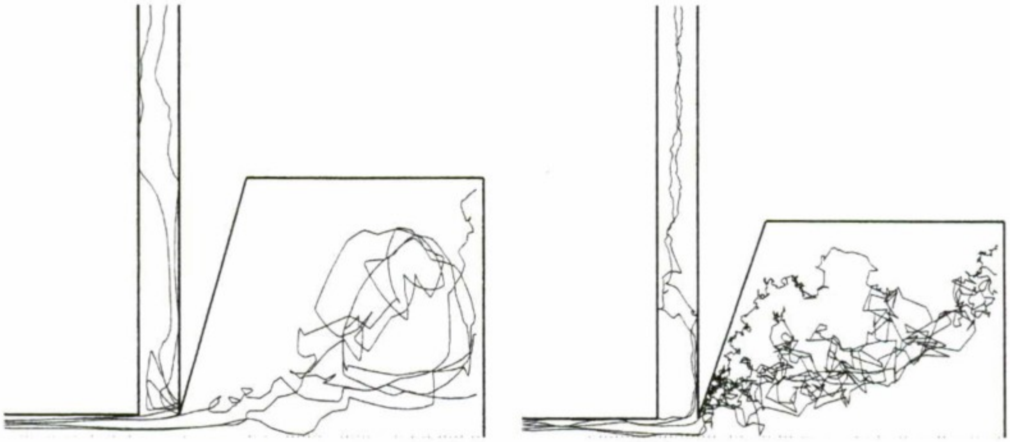

(a) (b)

Figure 4.6: Representative trajectories of 5 particles released from the inlet of the impactor for both (a) $\chi = 0.11$ and (b) $\chi = 0.98$. The collection efficiencies as measured by the number of particles entering the collection tube are 0.51 and 0.36 for $\chi = 0.11$ and $\chi = .0.98$, respectively.

the exit of the nozzle (Fig. 4.3; $s-3$*). For* $\chi = 0.11$, 0.50 *and* 0.98 *only* $7,763$, 9840 *and* 9500 *particles are counted, respectively. For* $\chi = 0.11$ *and* 0.50, 10^5 *integration steps were used to calculate the particle track. For* $\chi = 0.98$, 2×10^5 *and* 4×10^5 *integration steps were used; in the first case* 3840 *particles were counted and in the second* 9500. *Both integration steps resulted in a collection efficiency of* 0.35. *Therefore, in the calculation of collection efficiency the number of particles exiting the nozzle are assumed to be the total number of particles entering the impactor.*

Remark 10 *Fig. 4.7 shows the particle distribution at different surfaces (*$s-1$, $s-2$, $s-3$, *and* $s-4$*) of the impactor system. The particle distribution at the entrance of the collection tube is shown in Fig. 4.7 g and h, where the dotted line indicates the edge of the entrance. In the* $\chi = 0.98$ *case, the peak occurs away from the center and* *this can be expected for* $x/d < 4$ *according to Burwash et al. [6]. Similar distributions have also been observed by other researchers [1, 46]. The particle distribution in the shock condition has a peak at the center of the collection tube entrance.*

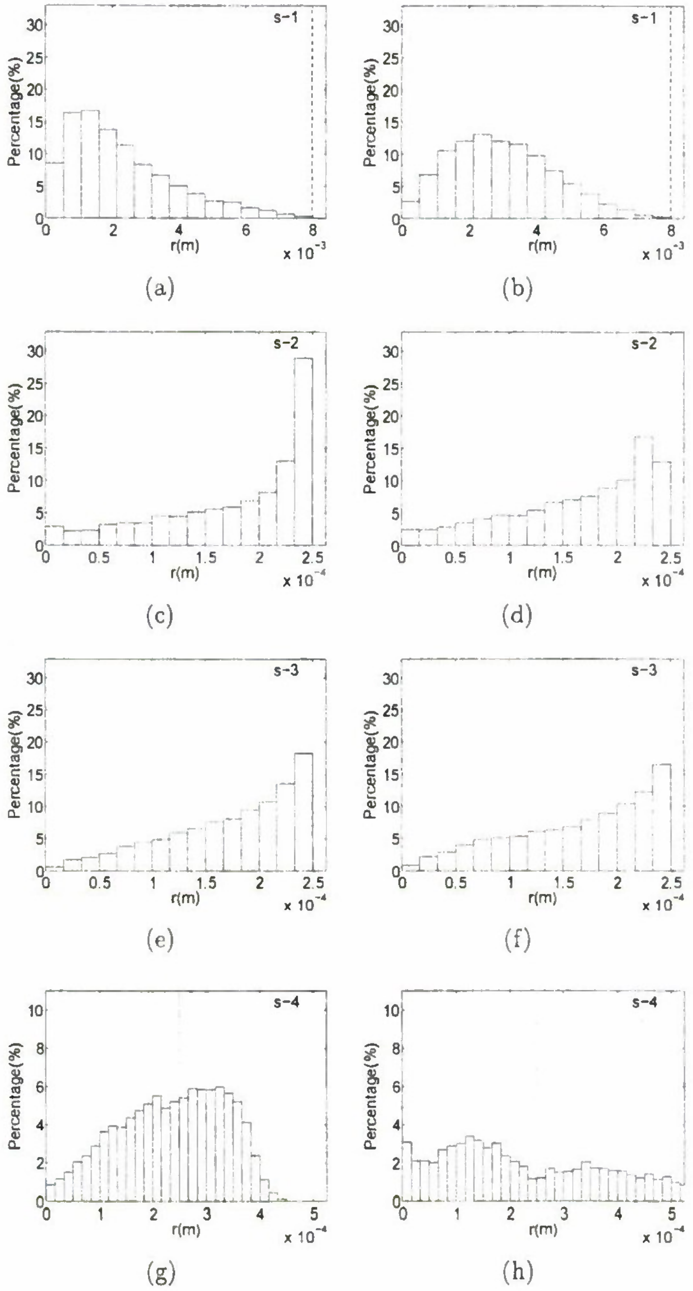

(a) (b) (c) (d) (e) (f) (g) (h)

Figure 4.7: Distribution of particles along different surfaces (s-1, s-2, s-3, s-4) labeled in Fig. 4.3. The x-axis is the distance (r) in meters from the centerline and the y-axis is the percentage of total particles released from the inlet of the impactor. The dashed and dotted lines indicate the wall of the impactor at s-1, s-2 and s-3 respectively. At s-4 the dotted line indicates the entrance of the collection tube. (left plots) Particles released under shock conditions and (right plots) particles released under non-shock conditions.

4.4 Cell viability results and discussion

Quantitative experimental measurements of cell viability were obtained via fluorescence flow cytometry (see Section 4.4.1) and fluorescence microscopy (see Section 4.2.4). Experimental data are supplemented with computational data on the collection efficiency of the impactor (see Section 4.3.3) for the different operating conditions. The goal is to assess the fraction of cells that remain alive after the effect of impactor operation (f_l):

$$f_l = \frac{n_c}{n'_c} \tag{4.9}$$

where n_c is the experimentally measured number of live cells including the break-up model and n'_c is the number of live cells that enter the collection tube under the assumption of no break-up (i.e., all cells are alive - see Eq. 4.11). f_l for the different operating conditions will be compared to assess the effect of the aerodynamic shock on the bacterial aerosol. The following sections will detail the data used to calculate f_l.

4.4.1 Fluorescence cytometry

The experimental fluorescence cytometry protocol described in Section 4.2.3 is used to obtain the data shown in Fig. 4.8. The data shown in Fig. 4.8 represents one set of experiments. A total of 15 sets of experiments were conducted, each from a different starting cell culture, to obtain statistically significant results in the calculation of f_l.

The left dot-plots in Fig. 4.8 represent the side-scatter (y-axis) and forward-scatter (x-axis) of a particle passing the laser beam in the flow cytometer. Each dot represents a particle's side and forward scatter intensities. The side scatter is a measure of the granularity and complexity while the forward scatter is related to the surface area (i.e. size) of the particle. The population of bacterial particles, enclosed in the gate denoted by G2/G3 in Fig. 4.8, is determined by running a PBS only solution to isolate the background enclosed in the gate denoted by G1. The right dot-plots shows the red fluorescence (FL2-H) versus green fluorescence (FL1-H) intensity for the gated (i.e. inside the polygon G2/G3) cell population. The analysis of the fluorescence plots provides information on the viability of the cell population. In Fig. 4.8-d the EtOH cell population can clearly be seen to lie in the top left half denoted by D. Live cells can be counted in the bottom right half denoted by L. Similar patterns have also been observed in the literature [3]. Furthermore, Berney et al. [3] indicate the presence of an intermediate state where the outer membrane in gram-negative cells is compromised. The intermediate state population can be seen as the population with the highest intensity green fluorescence in the L gate. For the purposes of the current study, the intermediate state cell population is grouped with the live population in order to make the requirements for neutralization more stringent.

The fraction of live cells (cells in bottom right half divided by total gated cells or L/(L+D)) in all analyzed samples is shown in Fig. 4.9. The error bars are the 95% confidence interval limits on the data using a normal fit. The data does not take into

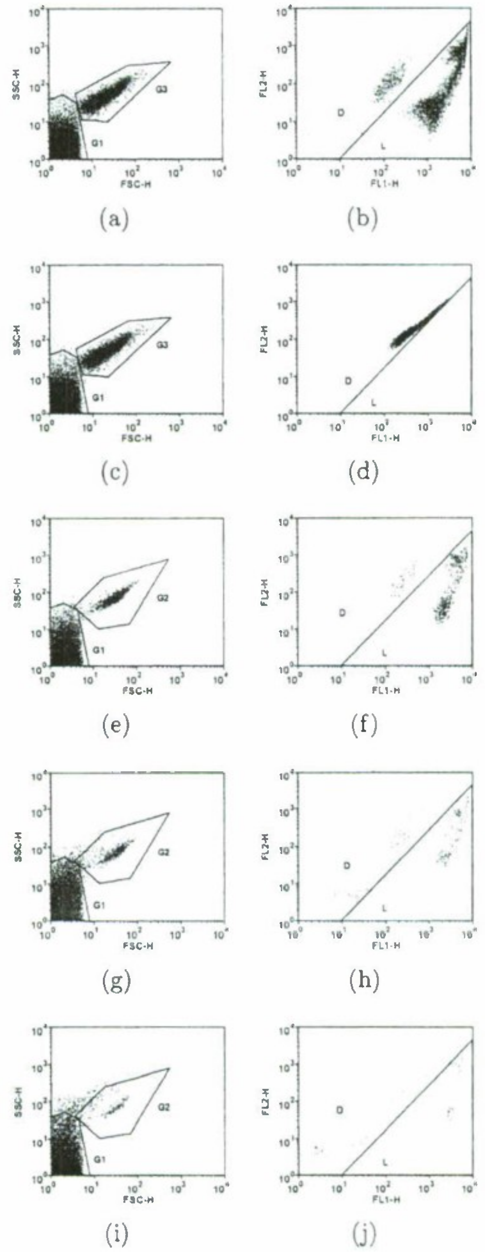

(a) (b)

(c) (d)

(e) (f)

(g) (h)

(i) (j)

Figure 4.8: (left) Side-scatter versus forward-scatter plot of all particles in the flow cytometer. The G2 gate indicates the particle sizes which represent intact cells. G1 indicates the debris population. (right) Red fluorescence (FLH-2) versus green fluorescence (FLH-1) of gated cells in the left side plots. The L gate represents the live cells and the D gate represents the dead cells. (a,b) Cell suspension in PBS, (c,d) cell suspension in EtOH, (e,f) cells collected after passing impactor operated at $\chi = 0.98$, (g,h) $\chi = 0.50$ and (i,j) $\chi = 0.11$.

account the mass balance on the system to indicate the overall neutralization rate. The data as shown in Fig. 4.9 ignores the break-up of cells since only intact cells are analyzed. Therefore, only a mass balance on the overall system can lead to the determination of the overall cell neutralization rate $(1 - f_l)$ or f_l. However, Fig. 4.9 provides raw data on the collected samples.

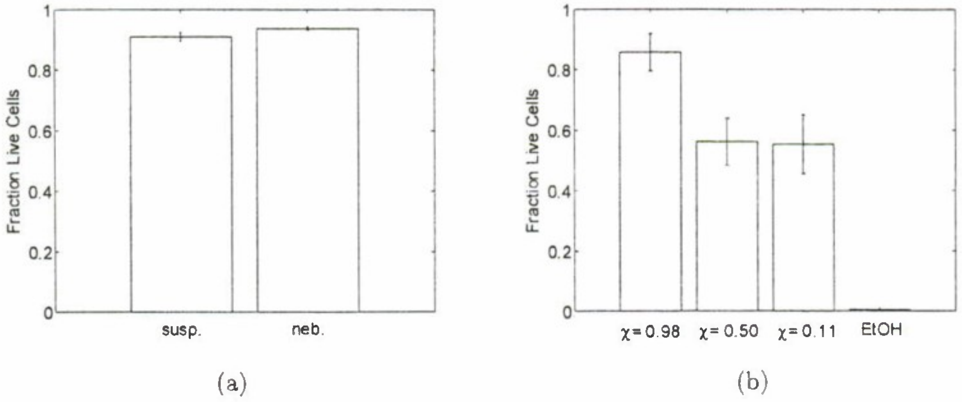

(a) (b)

Figure 4.9: Fraction of live cells in different collected samples. (a) All experiments start with a measurement of the fraction of live cells in the cell culture (susp), the negative control, and in the nebulized cells (neb). Error bars show the 95% confidence interval using a normal distribution for 5 measurements per sample. (b) The cells that pass through the impactor system and then collected in the collection tube at $\chi = 0.98$, $\chi = 0.50$, and $\chi = 0.11$ with $P_0 = 1$ atm. The ethanol (EtOH) suspension is the positive control. Error bars show the 95% confidence interval using a normal distribution for 15 measurements per sample.

The percentage of live cells in the nebulized sample can differ from that in the suspension because of the operating conditions of the nebulizer. The data in Fig. 4.9-a, represents 5 experiments with different starting cultures. The fraction of live cells in the suspension (0.910 ± 0.014) is equal to that of the nebulization (0.938 ± 0.005) with $p > 95\%$ using a two tailed t-test with unequal variance. Therefore, the effect of nebulization can be neglected in the calculation of the neutralization rate.

In Fig. 4.9-b, 15 experiments with different starting cultures were conducted for each of the operating conditions of the impactor. Both shock conditions ($\chi = 0.11$ and 0.50) have statistically equal fraction of live cells while they are lower statistically from the non-shock condition ($\chi = 0.98$). The cells exposed to ethanol (positive control) have the lowest fraction of live cells.

4.4.2 Mass balance

To evaluate the effect of particle acceleration in an aerodynamic shock a mass balance on the entire experimental system has to be done to account for all losses. Bacterial aerosol is lost to the walls of the system between the exit of the nebulizer and the entrance of the impactor. Determining the losses is important in the overall neutralization rate and is calculated as follows:

$$\phi = \frac{n_i}{n_n} \tag{4.10}$$

where n_n is the total number of cells that are nebulized and n_i is the total number of cells that enter the impactor. Experimental measurements (see Section 4.2.4) determine the actual number of particles that enter the impactor after losses in the nebulization process and in the tubes connecting the nebulization chamber to the impactor inlet. The measured ϕ is 0.088 ± 0.029 for all operating conditions of the impactor system. Losses to the walls of the nozzle after the impactor entrance are neglected. Nonetheless, not all the particles that enter the impactor are collected for analysis as detailed in Section 4.4.1. By assuming no cell break-up, we can calculate the number of live cells that enter the collection tube (n_c') as:

$$n_c' = n_{sl}\phi\eta \tag{4.11}$$

where n_{sl} is the number of live cells inputed to the system by nebulizing the suspension and is obtained experimentally by counting the cells in the lower right half (L) of Fig. 4.8-b. The collection efficiency of the impactor for the different operating conditions is listed in Table 4.2. Eq. 4.9 then becomes:

$$f_l = \frac{n_c}{n_{sl}\phi\eta} \tag{4.12}$$

where n_c is obtained by counting the number of cells in the lower right half (L) of Fig. 4.8-f or equivalent data for the different impactor operating conditions (Fig. 4.8-h, j).

4.4.3 Effect of the aerodynamic shock

By combining fluorescence cytometry, microscopy and computational collection efficiencies in Eq. 4.10, we can obtain the values for f_l for the different operating conditions in the impactor system. The data is shown in Fig. 4.10 with the 95% confidence interval on the normal fit of 15 independent experiments for each condition and using error propagation. In the experimental impactor system operating at $\chi = 0.98$, the bacterial aerosol does not experience the critical acceleration discussed in Section 4.3.2; therefore, the f_l is an order of magnitude higher than the conditions which lead to acceleration greater than the critical ($> 3.00 \times 10^8$ m/s^2). The acceleration at $\chi = 0.50$ is 2.02×10^8 m/s^2 which is approximately equal (considering experimental variation in pressure and assumptions in calculating the computational accelerations mention in Section 4.3) to the critical acceleration. In this case, a reduction in cell viability can be seen that is statistically the same as that observed for $\chi = 0.11$ with an acceleration of 4.96×10^9 m/s^2.

It is important to note that the Weber numbers in Fig. 4.10 for $\chi = 0.11$, 0.50 and 0.98 carried at $P_0 = 1$ atm are in the range $[0.0017, 3.5]$ (see Table 4.2) which is lower than the computational model-predicted critical Weber number of 14 needed for bacterial break-up. However, Fig. 4.10 clearly demonstrates that this estimate is conservative and an order of magnitude reduction in cell viability can be attained at a lower Weber number than 14 if the critical acceleration is achieved. To investigate this point further, we carried out experiments (see Remark 11) at a Weber number of 15 and an acceleration of 5.98×10^9 m/s^2 (both in the range needed for bacterial break-up) with $\chi = 0.11$ at $P_0 = 5$ atm and found no statistical difference in fraction of cells remaining live ($f_l = 0.047 \pm 0.016$ at $P_0 = 5$ atm compared to $f_l = 0.035 \pm 0.012$ at $P_0 = 1$ atm). Therefore, the sharp decelerations that the cells experience after they

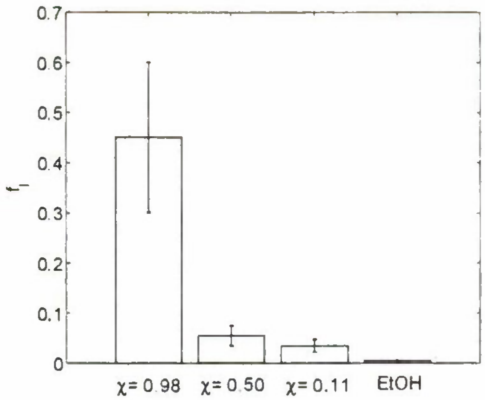

Figure 4.10: Fraction of cells that remain alive after the effect of impactor operation (f_l) and after exposure to ethanol. Live cells in these samples are compared to live cells in the negative control by accounting for losses before the impactor and for the collection efficiency of the impactor. Error bars show the 95% confidence interval using a normal distribution for 15 measurements per sample.

pass through the shock is the main reason for which they lose viability.

Remark 11 *Five experiments were carried out at a higher upstream pressure,* $P_0 = 5$ *atm* ($We = 15$)*, to investigate the influence of Weber number on cell viability. In order to run the impactor system of Fig.4.1 at an upstream pressure of* $P_0 = 5$ *atm, a high pressure chamber was designed to encase the nebulizer, and the HEPA filter was removed to avoid exposure to atmospheric pressure before the impactor. Furthermore, the nebulizer was operated at* $P_n = 10$ *atm to maintain the same* P_n/P_0 *ratio as the atmospheric pressure experiments. The bends in the tubing connecting the nebulizer to the impactor were also modified; this modification might slightly change the losses as measured by* ϕ*, however, in our calculations we assumed the losses as calculated in Section 4.4.2 stayed constant for all experiments. All other conditions were maintained as described in Section 2. The fraction of live cells in the collection* *tube in these 5 experiments was found to be* 0.332 ± 0.215 *and the corresponding* f_l *was computed to be* $f_l = 0.047 \pm 0.016$.

4.5 Conclusions

In this chapter, the computational model presented in Chapters 2 and 3 was validated by experimental viability analysis on vegetative gram-negative *E. coli* cells. The *E. coli* cells were used as a model bacterial aerosol with a computational-model predicted critical acceleration of 3.0×10^8 m/s^2 to achieve bacterial break-up. The experimental impactor system was operated under three conditions to provide maximum accelerations of 4.96×10^9 m/s^2, 2.02×10^8 m/s^2 and 1.67×10^6 m/s^2; values above, equal, and below the predicted critical acceleration for *E. coli*, respectively. The experiments show that for accelerations higher than the critical value the shock has a considerable effect, $f_l = 0.055 \pm 0.020$ for $\chi = 0.50$ and $f_l = 0.035 \pm 0.012$ for $\chi = 0.11$. Under the non-shock condition, $f_l = 0.451 \pm 0.150$ which is an order of magnitude higher survival rate than that found at higher accelerations. These results confirm the computational model predictions of Chapters 2 and 3. The computational model can therefore be used to predict the effect of an aerodynamic shock on bacterial cells given their surface tension and size.

Chapter 5

Effect of Aerodynamic Shock on *B. atropheus* spores

5.1 Introduction

In Chapter 4, Gram-negative *E. coli* vegetative cells were shown to break-up at decelerations $> 3.0 \times 10^8$ m/s^2. The impactor was operated to reach computed decelerations of 5.0×10^9 m/s^2 which predict break-up of the cells. The experimentally measured fraction of cells remaining live was 0.035 ± 0.012, confirming the computational predictions.

This Chapter focuses on the effect of aerodynamic shocks on spores which are more relevant as bioterrorism threats. In laboratory settings, *Bacillus subtilis* var *niger*, reclassified as *Bacillus atropheus* [19], is suggested as a surrogate for *B. anthracis* that emulates the spore's physical characteristics but avoids its pathogenicity [17]. The two spores have similar surface tension values [8]. Both computational and experimental methods are used to study the effect of aerodynamic shocks on *B. atropheus* spores and to obtain the fraction of cells that remain alive after the effect of impactor operation (f_i).

5.2 Experimental materials and methods

5.2.1 Experimental setup

The experimental system discussed in Chapter 4 [49] is used to determine the effect of the aerodynamic shock on *B. atropheus* spores. The details of the system (see Fig. 5.1) are described below. The vegetative *E. coli* suspension was substituted with *B. atropheus* spore suspension (see Section 5.2.2) in the nebulizer (see Section 5.2.1) [49]. The resulting aerosol travels to the impactor which was operated at different downstream to upstream pressure ratios (see Section 5.2.1) to capture both break-up and no break-up conditions. Quantitative analysis of the survival rate was carried out using fluorescence flow cytometry (see Section 5.2.3).

Nebulization

The *B. atropheus* spores suspension (see Section 5.2.2) was fed via a syringe pump (KDS410, Kd Scientific) at a liquid flow rate Q = 0.05 mL/min for 20 min to a

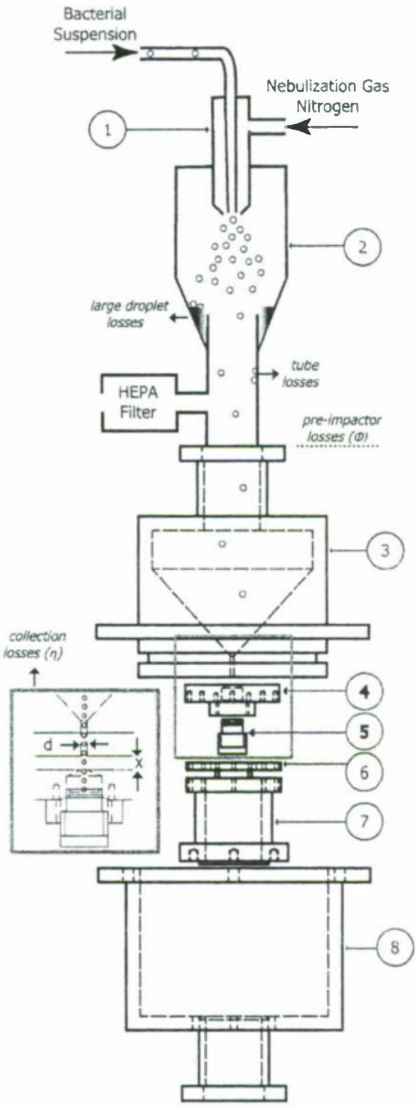

Figure 5.1: Schematic of the experimental system. (1) Meinhard nebulizer with a concentric nozzle mixing a liquid bacterial suspension feed and a dispersion gas (N_2), (2) Nebulization chamber to collect large droplets, (3) Converging nozzle with an exit diameter of $d = 0.5$ mm, (4) and (5) a flat surface with a 0.5 mm hole combined with a screw that accommodates the collection substrate make up the deceleration tube, (6) 1.4 mm spacer fixes the spacing x between the impactor and nozzle to 0.6 mm, (7) support holding the deceleration tube and flat surface at fixed distance from the nozzle, and (8) exit chamber. Major losses in the experimental system are shown in italic.

capillary nebulizer (TR-30-A1, Meinhard Glass Products). Nitrogen (N_2) gas was supplied at a critical flow rate of 0.2 L/min through the annular region. The liquid was fed at a specified bacterial concentration (see Section 5.2.2) determined by the optical density measurement at 600 nm (OD_{600}). Nitrogen was supplied to the nebulizer at a pressure P_n via a pressurized tank. In all the experiments, the nebulizer was operated at $Q = 0.05$ mL/min, $OD_{600} = 0.5$, and $P_n = 2$ atm. The spore concentration at $OD_{600} = 0.5$, as measured using fluorescence flow-cytometry (see Section 5.2.3), was $5.02 \pm 1.24 \times 10^5$ spores/mL. The average expected nebulized droplet size is 10 μm, which translates to approximately 1 cell in every 1000 droplets assuming no aggregates are formed in the droplets.

Impactor system

A detailed description of the impactor system was given in Chapters 2 and 4 [51, 49]. Briefly, the impactor system consists of a plate designed for the collection of the bacterial aerosol (see Fig. 5.1; parts 4 and 5) which is placed perpendicular to the gas flow emerging from a converging nozzle (see Fig. 5.1; part 3). Isentropic flow theory of an ideal gas predicts a critical downstream (P_1) to upstream (P_0) pressure ratio (χ_{crit}) below which the flow at the exit of the nozzle is sonic [38, 48]. For Nitrogen (N_2), χ_{crit} is 0.53 [51, 49]. The generated impinging flow on a plate from a converging nozzle operating under sonic conditions results in the creation of a standoff shock whose properties can be changed by varying impactor geometry (distance between nozzle and plate x and diameter of nozzle d) and operating conditions [2, 13, 14, 29, 42, 51]. The deceleration tube (see Fig. 5.1; parts 4 & 5) is filled with 600 μL of phosphate buffer saline (PBS) solution (BP2438-4, Fisher Scientific), which keeps the liquid level to about 4 mm away from the entrance of the deceleration tube. The plate to nozzle distance is set at $x/d = 1.2$. The impactor system is operated at an upstream pressure of $P_0 = 1$ atm with three different pressure ratios $\chi = P_1/P_0 = 0.98$, 0.50 and 0.11 for 20 min. After each experimental run the volume of PBS remaining in the deceleration tube was measured and used in mass balance calculations to determine the fraction of cells surviving the impactor operating conditions (see Section 5.4). Fig. 5.1 shows the losses, ϕ and η, of bacterial particles in different parts of the experimental system which are discussed in Sections 5.2.1 and 5.3.2.

Particle losses in experimental setup

Losses of spores to the walls of the system before entering the impactor $(1 - \phi)$ were accounted for using calculations developed Chapter 4 [49]. Specifically, vegetative *E. coli* cells were collected on an in-line filter placed before the impactor system [49]. Fluorescence microscopy images were taken to count the fluorescent bacteria on the stained filter. These images were then analyzed to calculate the fraction of cells entering the impactor (ϕ), which is defined as

$$\phi = \frac{n_i}{n_n} \tag{5.1}$$

where n_n is the total number of cells nebulized and n_i is the total number of cells entering the impactor. The parameter ϕ was calculated to be 0.088 ± 0.029 from the in-line filter counts [49]. Although the calculation was made using experimental data on *E. coli* vegetative bacteria (whose diameter is ≈ 1 μm), the same value of ϕ was used for *B. atropheus* spores (whose diameter is ≈ 0.5 μm). Two processes are responsible for losses in the system before the impactor: (1) losses of large nebulized liquid droplets on the nebulization chamber (see Fig. 5.1; part 2) walls, and (2) losses of bacterial aerosol in the tubes leading to the impactor. Losses in the tubes can either be diffusional or inertial (impaction). Diffusional losses $(1 - n_{out}/n_{in})$ were calculated for circular tubes using the following expression [23]:

$$n_{out}/n_{in} = 1 - 5.5\left(\frac{DL}{Q_g}\right)^{2/3} + 3.77\left(\frac{DL}{Q_g}\right) \tag{5.2}$$

where n_{out} and n_{in} are the number of particles exiting and entering the tube, respectively, D is the diffusion coefficient, L is the length of the tube, and Q_g is the volumetric flow rate of gas. For both 1 μm and 0.5 μm particles the ratio, n_{out}/n_{in}, is calculated to be $> 99\%$. Therefore, diffusional losses $(1 - n_{out}/n_{in})$ are negligible. To calculate the impaction losses the following relation was used [23]:

$$n_{out}/n_{in} = 1 - 2\theta\left(\frac{\rho_p d_p^2 U_g}{18\mu_g D_s}\right) \tag{5.3}$$

where ρ_p is the particle density, d_p is the particle diameter, U_g is the average gas velocity in the tubes leading to the impactor, μ_g is the gas viscosity, D_s is the tube diameter and θ is the bend angle. The term in parentheses in Eq. 5.3 is also referred to as the Stokes number. The ratio, n_{out}/n_{in}, was also $> 99\%$ for both particle sizes. Therefore, most of the losses before the impactor $(1 - \phi)$ are attributed to the identical nebulization process (see Section 5.2.1)) for ≈ 1 μm *E. coli* vegetative cells and ≈ 0.5 μm *B. atropheus* spores under identical conditions with $\phi = 0.088 \pm 0.029$.

5.2.2 Spore preparation

Bacillus atropheus (strain ATCC 9372) was used as the standard bacterial aerosol to study the aerodynamic shock effect on bacterial spores in the impactor system. In our previous study, *E. coli* was used as a test aerosol for vegetative bacterial cells [49]. The methods described in this section were adopted with minor modifications to the standard procedures for culturing and washing of *Bacillus* spores [20]. All vegetative cultures were initiated from a stock *B. atropheus* suspension (80% glycerol solution) stored at −20 °C. 5 mL of Nutrient broth (Fisher) was inoculated with 10 μL of stock suspension in a test tube. The vegetative culture was incubated in a shaker (Excella E24, New Brunswick Scientific) at 32 °C and 200 rpm for approximately 22 – 25 hrs. To start the spore culture, 1 mL of the vegetative *B. atropheus* was inoculated in 15 mL of 2×SG media that was prepared as described in standard procedures [20]. The spore culture was incubated for 12 days at 32 °C and 200 rpm, allowing time for the cells to exhaust nutrients in the medium, thereby inducing sporulation.

After the incubation period the spore culture was washed over 4 days. On day 1, the culture was centrifuged at 4400 rpm for 15 min (Centrifuge 5702, Eppendorf). Three layers were observed with the lower layer containing the free spores and the top 2 layers containing cell debris [20]. The suspension was washed 3 times with cold autoclaved deionized (DI) water, keeping all three layers and then shaking in an ice bath overnight. Similar procedures were repeated for days 2 and 3 with the exception of resuspending and decanting the top two layers instead of keeping them. Most of the cell debris layers were removed after the third day. On day 4 the suspension was centrifuged at 4400 rpm and washed 3 times using cold PBS. The optical density of the spore suspension was measured at a wavelength of 600nm (OD_{600}) using a visible light spectrophotometer (Genesis 20, Thermo Scientific) before storage at 4 °C.

To check the degree of sporulation, starting suspensions were treated with lysozyme, which breaks down the peptidoglycan outer membrane in Gram-positive vegetative cells such as *B. atropheus.* Since spores do not have an exposed peptidoglycan layer, lysozyme is expected to have no effect. The suspension was diluted to $OD_{600} = 0.05$ and lysozyme (L6876, Sigma Aldrich) was added for a solution concentration of 2.8×10^{-1} g/mL and incubated for 30min at 32 °C and 200 rpm. The lysozyme treatment was also used on vegetative *B. atropheus.* The fraction of spores was determined by comparing viability analysis (see Section 5.4.1) of the spore suspension to the vegetative cells.

At the start of each experiment, a positive and a negative control were prepared by diluting the spore suspension to $OD_{600} = 0.05$. The positive control was incubated in a water bath at 100 °C for over 2 hours to neutralize the spores [11]. The negative control was left untreated and is therefore expected to have the highest concentration of viable spores. The samples collected after the impactor operation is compared to both the positive and negative control to assess the effect of the shock (see Section 5.4.2).

5.2.3 Bacterial viability analysis

Bacterial viability is determined using LIVE/DEAD®*Bac*Light^{TM} (cat. number L7012; Life Technologies Corporation) [3, 32]. The assay contains two components: (A) 3.34 mM STYO 9, a green-fluorescent nucleic acid stain, in dimethyl sulfoxide (DMSO) and (B) 20 mM propidium iodide (PI), a red-fluorescent nucleic acid stain, in DMSO. STYO 9 penetrates both intact and damaged membranes, while PI only penetrates damaged membranes. A stock dye solution is prepared at the start of every experiment by mixing 5 μL of each of components A and B with 10 μL deionized water (DI). All controls and experimental samples mentioned in Sections 5.2.1 and 5.2.2 were stained with the stock dye solution to a final concentration of 8.35 μM and 50 μM of STYO 9 and PI, respectively.

The stained samples were analyzed using a fluorescence flow cytometer (FACScan^{TM}, BD Biosciences). The cytometer was operated at 12 μL/min for 20s with a 488 nm excitation laser. Red fluorescence was measured with a high pass filter at 630 nm (FL2-H) and green fluorescence was measured with a bandpass filter of 520 nm (FL1-H). The forward scatter (FSC) and side scatter (SSC) were also measured for the particles passing the laser. Photomultiplier tubes were used to amplify the optical signal for FL1-H, FL2-H and SSC at 730, 648 and 462 volts, respectively. A photodiode was used to detect the FSC signal.

5.3 Computational results

5.3.1 Gas flow field

At low aerosol concentrations the equations for gas and particle dynamics are one-way coupled [18]. First, the gas dynamics equations are solved and the gas velocity is used to calculate the particle dynamics. A FLUENT® computational fluid dynamics (CFD) code was developed to solve both gas and particle dynamics in the experimental impactor system of Fig. 5.1 [51]. Details of the model were described in Chapter 2. The Reynolds time-averaged Navier-Stokes equations in Cartesian tensor form are:

$$\frac{\partial \rho}{\partial t} + \frac{\partial}{\partial x_j}(\rho v_j) = 0, \tag{5.4}$$

and

$$
\begin{aligned}
&\frac{\partial}{\partial t}(\rho v_i) + \frac{\partial}{\partial x_j}(\rho v_i v_j) \\
&= -\frac{\partial p}{\partial x_i} + \frac{\partial}{\partial x_j}\left[\mu\left(\frac{\partial v_i}{\partial x_j} + \frac{\partial v_j}{\partial x_i} - \frac{2}{3}\delta_{ij}\frac{\partial v_l}{\partial x_l}\right)\right] + \frac{\partial}{\partial x_j}(-\rho\overline{v_i' v_j'}), \quad i = 1, 2, 3
\end{aligned}
\tag{5.5}
$$

where ρ is the density, v is the velocity, p is the static pressure, δ is the Kronecker delta, μ is the viscosity, and i, j, and l are the Cartesian indices. To achieve closure of Eq. 5.5, the Reynolds stress term $-\rho\overline{v_i' v_j'}$ is calculated using the Boussinesq hypothesis [24]. A standard $k - \epsilon$ turbulence model is used in the gas flow equations. A detailed computational parametric study indicated that the maximum centerline Mach number (M_{max} increases with increasing x/d and decreasing P_1/P_0) (see Chapter 2) [51]. Furthermore, at higher x/d (> 1.4) the aerodynamic shock is unstable [51]. $x/d = 1.2$ had the highest M_{max} with no flow instabilities (see Chapter 2) [51]. Operating the impactor at three different pressure ratios $\chi = 0.98$ 0.50, and 0.11 captures gas flow fields with no aerodynamic shock, at critical nozzle flow (χ_{crit}), and strong aerodynamic shock, respectively. The maximum centerline Mach number is 2.36 at $\chi = 0.11$ (see Table 5.1).

Table 5.1: Aerodynamic shock properties at different operating conditions with $x/d = 1.2$ and $P_0 = 1$ atm

χ	M_{max}	Re
0.98	0.14	9.9×10^2
0.50	0.96	5.8×10^3
0.11	2.36	5.4×10^3

5.3.2 Particle dynamics

The velocity profile of the particle motion is used for the calculation of mechanical forces induced on the particle (see Section 5.3.2). As in previous chapters, the particle trajectory is solved using Newton's second law with the gas flow field solutions from Section 5.3.1 [49, 51]:

$$m_p \frac{dv_p}{dt} = \frac{1}{2} C_D \rho_g A_p (v_g - v_p)|v_g - v_p|, \tag{5.6a}$$

$$\frac{dx}{dt} = v_p, \tag{5.6b}$$

where v_p and v_g are the velocity of the bacterial particle and gas, respectively, m_p is the mass of the particle, ρ_g is the density of the gas, A_p is the projected area of the bacterium on the plane perpendicular to the flow direction, and C_D is the drag coefficient. The thermophoretic, gravitational, and Basset history term are neglected in Eq. 5.6a. The drag force is assumed to be the major force acting on the bacterial particle which is typical for impactor systems. A high Mach number drag law is used to calculate the drag coefficient (C_D) [9]. The size of *Bacillus* spores is in the range of $0.5 - 1.2$ μm [10, 8]. The bacterium is simulated as a 0.5 μm sphere with a density ρ_p of 1g/mL which is representative of values reported in literature [33, 59]. Values for 1 μm particles were obtained from previous studies [49]. The computational simulations mimic the experimental conditions in the study with $x/d = 1.2$ under shock ($\chi = 0.11, 0.50$) and non-shock ($\chi = 0.98$) conditions. The detailed conditions are shown in Sections 5.3.2 and 5.3.2. The computational results predict the collection efficiency of the impactor system at different operating conditions (see Section 5.3.2) and bacterial envelope instability (see Section 5.3.3).

Particle acceleration

A fifth-order Runge-Kutta method is used to numerically integrate Eq. 5.6a and 5.6b using the gas velocity obtained from the computational model described in Section 5.3.1. The particle velocity is calculated every $5 \times 10^{-5} - 10^{-7}$ m (for $\chi = 0.11 - 0.98$) along the centerline of the impactor. Fig. 5.2 shows the gas and particle velocity profiles along the centerline of the impactor in the region of the shock. Under shock conditions ($\chi = 0.11$), the aerodynamic shock is observed as a sharp drop in gas velocity (see Fig. 5.2-a). Because the particle does not adjust to the gas stream velocity, it experiences a relative deceleration. For non-shock conditions ($\chi = 0.98$), the gas velocity decreases at slower rate compared to the shock allowing the particle to adjust its velocity (Fig. 5.2-c) without experiencing a relative deceleration as strong as in the shock case. Fig. 5.2-b shows the velocity profiles for $\chi = 0.50$ where the particle observes an intermediate relative deceleration.

The relative deceleration of the particle is determined by calculating the relative velocity derivative with respect to time (see Eq. 3.8b) [51]. The results of this differentiation, expressed in absolute values, are shown in Fig. 5.3. The decelerations provide a measure of the force required to neutralize bacterial aerosols (see Section 5.3.3). As

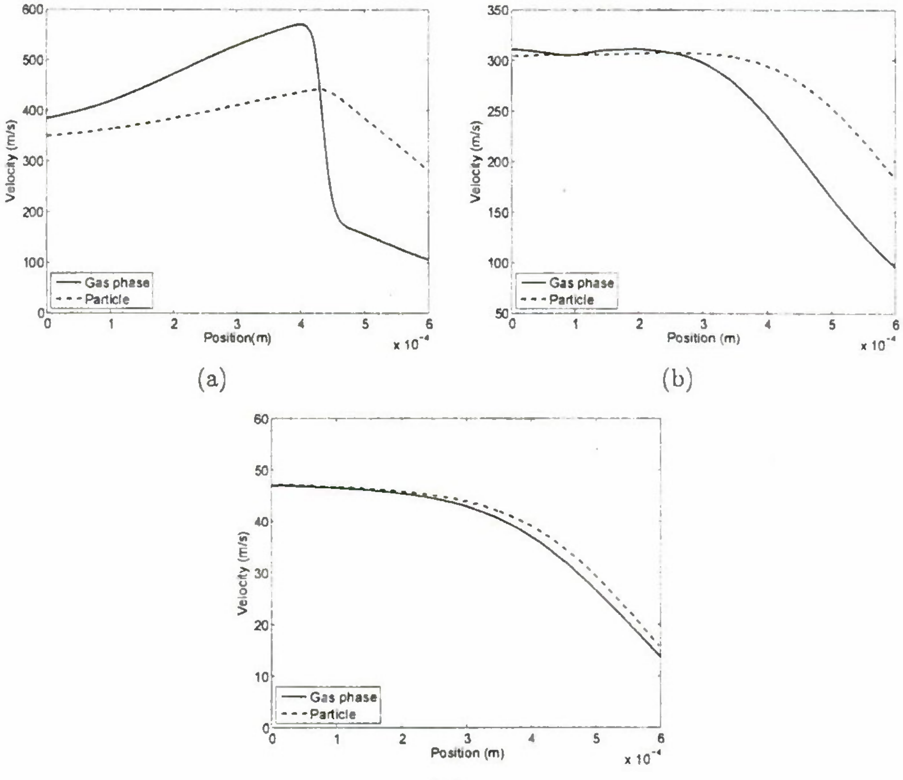

(a)

(b)

(c)

Figure 5.2: Centerline particle and gas velocity as a function of the distance from the nozzle. The entrance of the collection tube is at a distance 6×10^{-4} m from the nozzle exit. Impactor operating conditions: (a) $\chi = 0.11$, (b) $\chi = 0.5$, and (c) $\chi = 0.98$.

seen in Fig. 5.3-b and c, the absolute value of acceleration increases at 5×10^{-4} m from the nozzle exit after the main deceleration peak. Since Brownian motion and gravitational effects were neglected in Eq. 5.6a, particles artificially stop before reaching the collection tube bottom. This is manifested as a second increase in the absolute value of the acceleration at the entrance of the deceleration tube. In Chapter 4, simulations with 1 μm particles showed similar increases in the acceleration before the inlet of the deceleration tube because of assumptions in the computational model discussed in Section 5.3.2 [49].

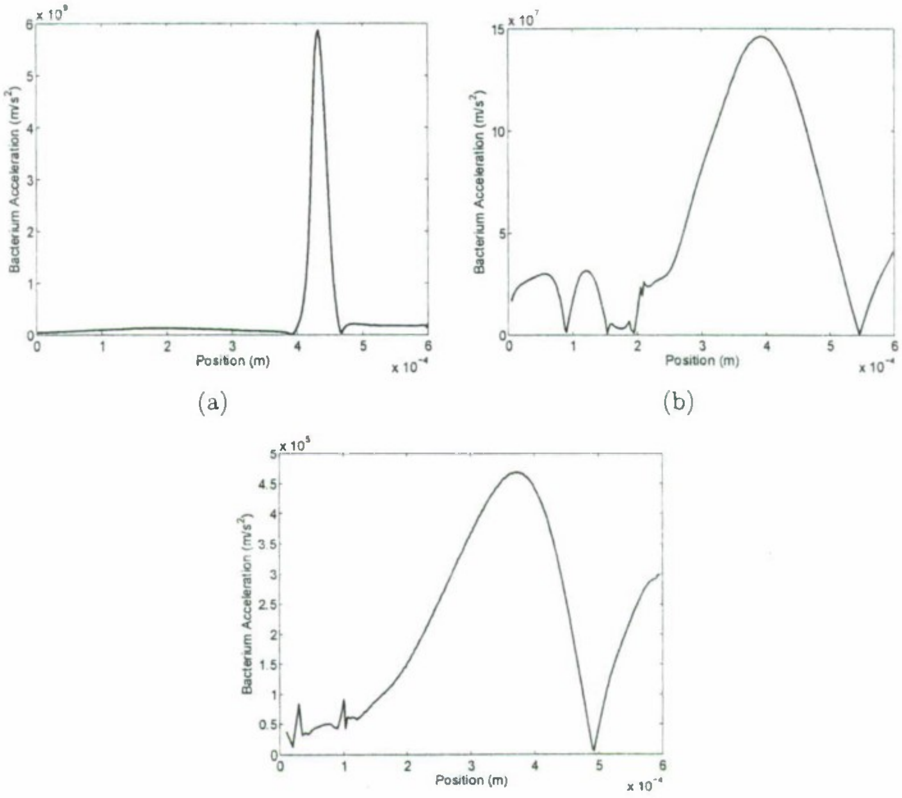

(a)

(b)

(c)

Figure 5.3: Bacterial particle acceleration (relative to gas flow) as a function of the distance from the nozzle. The entrance of the collection tube is at a distance 6×10^{-4} m from the nozzle exit. Impactor operating conditions: (a) $\chi = 0.11$, (b) $\chi = 0.5$, and (c) $\chi = 0.98$.

The maximum centerline decelerations (a_{max}) reached between the nozzle exit and deceleration tube entrance for the three different operating conditions are reported in Table 5.2. The maximum acceleration and weber number increase with decreasing χ (see Chapters 3 and 4) [49, 51]. At $\chi = 0.11$, acceleration increases with smaller particle sizes, which is a trend observed for $\chi = 0.14$ at $x/d = 1.0$ and 1.4 in Chapter 3 [51]. At $\chi = 0.98$ and 0.50, the trend is reversed as the flow transitions to subsonic velocities.

Particle collection efficiency

In Section 5.3.2 average gas velocities were used to calculate the particle acceleration. However, the collection efficiency for highly turbulent flows and low-density, small-size aerosols, depends on particle dispersion due to gas velocity fluctuations. The collection efficiency (η) is defined as the ratio of the number of particles that pass through the collection tube entrance compared to the number of particles that enter the impactor inlet. The bacterial collection efficiency (η) for all three impactor operating conditions ($\chi = 0.11, 0.50, 0.98$) are evaluated to determine the overall bacterial aerosol neutralization rate in Section 5.4. The random walk model is employed to study the effect of velocity fluctuation on bacterial aerosol with reasonable computational load. Stochastic tracking of the particles is used to account for the turbulent dispersive effects in the gas flow. In the stochastic tracking model the gas velocity is represented as an average plus a fluctuating term when calculating the particle velocity, v_p, in Eq. 5.6a. The fluctuating velocity is kept constant for time intervals corresponding to the lifetime of turbulent eddies. The following equations describe the stochastic behavior:

$$v_g = \overline{v} + v' \tag{5.7a}$$

$$v' = \zeta\sqrt{\overline{v'^2}} = \zeta\sqrt{2k/3} \tag{5.7b}$$

$$t_L = 0.15k/\epsilon \tag{5.7c}$$

$$\tau_\epsilon = -t_L \log r \tag{5.7d}$$

where v_g is the instantaneous gas velocity, $\overline{v}$ is the average velocity, and v' is the velocity fluctuation term. v' is a function of ζ, a normally distributed random number, and $\overline{v'^2}$ is the local root mean square of the fluctuations. $\overline{v'^2}$ is calculated based on the assumption of isotropy and is given by $\overline{v'^2} = 2k/3$, with k being the turbulence kinetic energy in the $k-\epsilon$ model. t_L is the lagrangian time interval, ϵ is the turbulence dissipation rate, τ_ϵ is the lifetime of the eddies, and r is a uniformly distributed random number between 0 and 1. Fig. 5.4 shows the path of 5 particles released from the

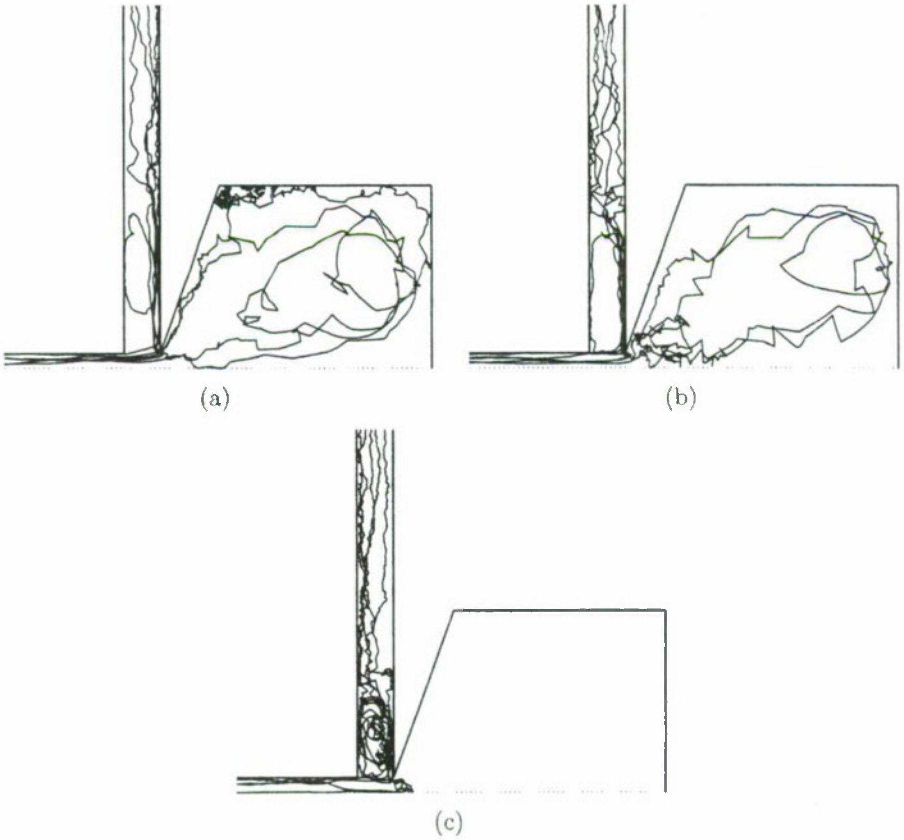
(a)

(b)

(c)

Figure 5.4: Representative trajectories of 5 particles released from the inlet of the impactor for (a) $\chi = 0.11$ (b) $\chi = 0.5$ and (c) $\chi = 0.98$. The collection efficiencies as measured by the number of particles entering the collection tube are 0.37, 0.48 and 0.26 for $\chi = 0.11$, $\chi = 0.50$ and $\chi = 0.98$, respectively.

inlet as they exit the nozzle of the impactor system for both $\chi = 0.11$ (Fig.5.4-a), $\chi = 0.50$ (Fig. 5.4-b) and $\chi = 0.98$ (Fig.5.4-c). In calculating η, 10,000 particles are released at the inlet of the impactor. The particles are then counted as they pass the virtual surfaces $s-1$ (nozzle exit) and $s-2$ (deceleration tube entrance), shown in Fig. 5.5.

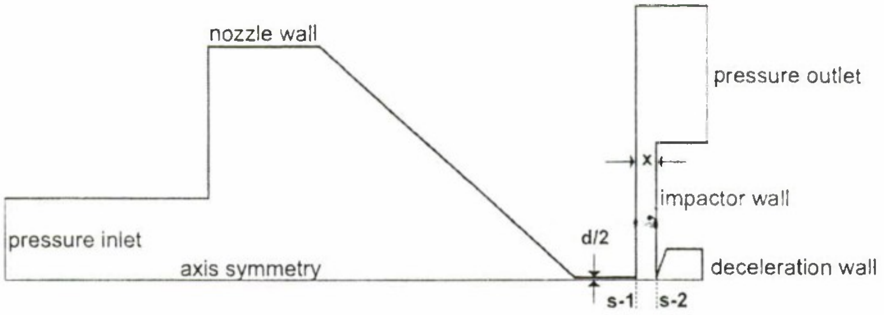

Figure 5.5: Computational domain of the impactor. The two dashed lines indicate different virtual surfaces (S-1 and S-2) where particles are counted. The collection efficiency is calculated by dividing the number of particles passing S-2 by that of S-1.

Except for the pressure inlet and outlet, all the boundaries shown in Fig. 5.5 are assumed to be reflection boundaries. The collection efficiency is defined as follows:

$$\eta = \frac{n'_c}{n_i} \tag{5.8}$$

where n_i is the number of particles entering the impactor and n'_c is the number of particles that enter the collection tube. n'_c is calculated under the assumption of no break-up. η is used to determine the total number of live cells that would be collected if the shock were to have no effect (see Section 5.4). For different operating conditions, the collection efficiency (η) for both 1 μm and 0.5 μm size particles is reported in Table 5.2. The values for 1 μm are taken from Chapter 4 [49]. η increases with diameter as the inertia of the particle increases and prevents it from following the gas streamlines [21, 22].

Table 5.2: Particle dynamics parameters at different operating conditions with $x/d = 1.2$ and $P_0 = 1$ atm for $d_p = 0.5$ and 1 μm

χ	a_{max} (m/s^2)		We_{max}		η	
	0.5 μm	1 μm	0.5 μm	1 μm	0.5 μm	1 μm
0.98	4.7×10^5	1.7×10^6	5.6×10^{-4}	1.70×10^{-2}	0.26	0.35
0.50	1.5×10^8	2.0×10^8	5.4×10^{-1}	3.5×10^0	0.48	0.72
0.11	5.9×10^9	5.0×10^9	1.7×10^0	3.1×10^0	0.34	0.51

5.3.3 Critical accelerations for *B. atropheus*

Rayleigh-Taylor instabilities are created at interface between two fluids of different density (air-bacterium) when they are at relative acceleration with respect to each other [7, 28]. As shown in Chapters 3 and 4, The acceleration induces waves on the interface which become unstable at a critical acceleration of:

$$a_c = 4\pi^2 \frac{\sigma}{\rho_p d_p^2} \tag{5.9}$$

where a_c is the critical acceleration, σ is the surface tension of the bacterium, d_p is the diameter of the bacterium, and ρ_p is the density of the bacterium. The Weber number of the bacterium should also exceed the critical Weber number [28]:

$$We > We_c = 12(1 + 1.077 Oh^{1.6}) \tag{5.10a}$$

where

$$We = \frac{\rho_g (v_{p_i} - v_{g_i})^2 d_p}{\sigma} \tag{5.10b}$$

and

$$Oh = \frac{\mu_p}{(\rho_p d_p \sigma)^{1/2}} \tag{5.10c}$$

where We is the Weber number, which is the ratio between the inertial force exerted on the bacterial particle and the particle surface tension force. Oh is the Ohnesorge number, which is the ratio between the viscous forces and the surface tension force. v_{p_i} and v_{g_i} are the particle and gas velocity in the x-direction (i.e., direction of flow along centerline), respectively. Therefore, bacterial membrane break-up is inferred by computing the relative velocity $(v_{p_i} - v_{g_i})$ of the bacterium and the maximum acceleration achieved. The critical acceleration conditions that satisfy the conditions for break-up are met for $\chi = 0.11$; however, the conditions for the Weber number are not. As reported in Sections 5.4.2 and 4.4.3 [49], cells will still break-up under non-critical Weber number conditions; which points to the conservative nature of the Weber number conditions. In this study, only the effect of Rayleigh-Taylor instabilities is considered.

Table 5.3: Cell properties for *E. coli* and *B. atropheus* [8, 61] and critical shock properties needed to induce bacterial break-up. Values are reported for both 0.5 μm and 1 μm for spores. (The Gram column refers to the Gram stain)

Cell	Gram	State	d_p (μm)	σ (N/m)	a_c (m/s^2)	We_c
E. coli	-ve	Vegetative	1	7.5×10^{-3}	3.0×10^{8}	1.4×10^{1}
B. atropheus	+ve	Spore	0.5	9.6×10^{-2}	1.6×10^{10}	1.3×10^{1}
B. atropheus	+ve	Spore	1	9.6×10^{-2}	3.9×10^{9}	1.2×10^{1}

Bacterial cells with a lower surface tension and larger diameters require lower accelerations to break-up. It is important to note that the surface tension values reported in Table 5.3 are derived from the turgor pressure [61] and contact angle [8]. However, the surface tension can vary with deformation generated by fluid flow over the cell membrane. Such a variation of the cell surface tension under fluid flow may limit the accuracy of the critical acceleration predictions of Table 5.3. In such a case, more accurate models of the variation of cell surface tension under stress generated by the fluid flow (similar to the works of [30, 31, 52, 60]) should be utilized and combined with the fluid flow and particle motion models developed here to make accurate critical acceleration predictions. Previous work [31] has demonstrated for the first time the use of inertial forces (expressed in terms of the Weber number and acceleration) in achieving cell break-up in the context of a high-pressure homogenization system.

5.4 Experimental results and discussion

5.4.1 Flow cytometry results

Fig. 5.6 shows a representative set of raw data obtained using the protocols described in Section 5.2.3. A total of 18 experiments were performed with 6 different starting spore suspensions. In the left plots, the side scatter (SSC) versus the forward scatter (FSC) (see Fig. 5.6) is a measure of the relative particle sizes. The S gate indicates the population of spores. The right plots in Fig. 5.6 show the red (FL2-H) versus green (FL1-H) fluorescence emission (see Section 5.2.3) of the spores in gate S. The negative (Fig. 5.6-a,b) and positive (Fig. 5.6-c,d) control define the live and dead cell region in the FL2-H vs. FL1-H plots. The live regions are indicated by the gate L and the dead by D. The fraction of cells live (L/S) is determined by dividing the number of spores in gate L by the total number of spores in gate S ($S = L + D$). The average value of the fraction of live cells (L/S) from all 18 experiments is shown in Fig. 5.7 and Table 5.4. L/S is not the true measure of the effect of the aerodynamic shock on bacterial aerosol since it only measures intact cells. The overall neutralization $1 - f_l$ or fraction of cells remaining intact after the effect of the impactor f_l is calculated through a mass balance on the experimental system and is discussed in Section 5.4.2.

Using a two-tailed t-test with unequal variance, the fraction of live cells for the negative control and $\chi = 0.98$ is equal with a $p > 95\%$ (see Table 5.4). However, the mean fraction of cells live are unequal for $\chi = 0.98$, $\chi = 0.50$, and $\chi = 0.11$ ($L/S_{0.98} > L/S_{0.50} > L/S_{0.11}$) with a $p > 95\%$. In Chapter 4 with *E. coli*, $L/V_{0.98} > L/V_{0.50} = L/V_{0.11}$ (where $V = L + D$ represents the vegetative cells gate) with a $p > 95\%$ [49]. The results are discussed in Section 5.4.2 in comparison to the fraction of cells that remain live after the shock (f_l), which accounts for the total mass balance in the system.

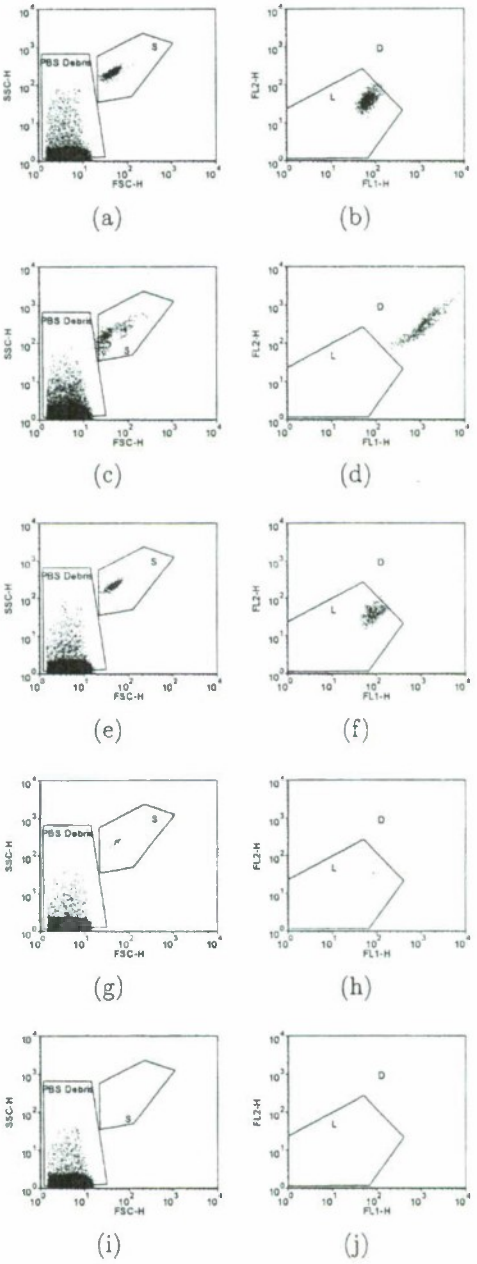

(a) (b)

(c) (d)

(e) (f)

(g) (h)

(i) (j)

Figure 5.6: (left) Side-scatter versus forward-scatter plot of all particles in the flow cytometer. The S gate indicates the particle sizes which represent intact spores. PBS debris indicates the debris population. (right) Red fluorescence (FL2-H) versus green fluorescence (FL1-H) of gated cells in the left side plots. The L gate represents the live cells and the D gate represents the dead cells. (a,b) spore suspension in PBS at $OD_{600} = 0.05$, (c,d) spore suspension after exposure to heat, (e,f) cells collected after passing impactor operated at $\chi = 0.98$, (g,h) $\chi = 0.50$ and (i,j) $\chi = 0.11$.

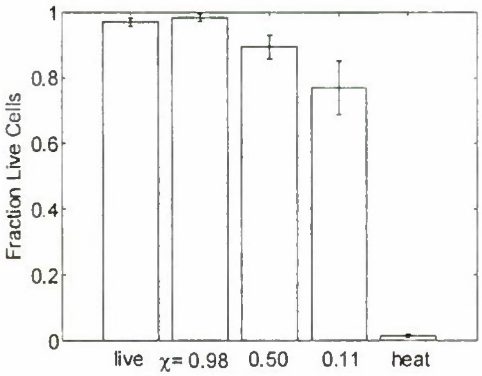

Figure 5.7: Fraction of live cells in different collected samples (L/S). All experiments start with a measurement of the fraction of live cells in the cell culture (live), and the negative control (heat). The cells that pass through the impactor system and then collected in the collection tube at $\chi = 0.98$, $\chi = 0.50$, and $\chi = 0.11$ with $P_0 = 1$ atm. Error bars show the 95% confidence interval using a normal distribution for 18 measurements per sample.

Lysozyme treatment results

The effect of lysozyme on spores (Fig. 5.8-c and d) is compared to the effect of lysozyme on vegetative *B. atropheus* cells (Fig. 5.8-g and h) in order to confirm the presence of spores in the starting suspensions. The live (L) and dead (D) gates were set by running a positive control for both spore and vegetative cells (not shown in Fig. 5.8). Ethanol is used as a positive control for vegetative cells as in Chapter 4 [49]. The V gate indicates the vegetative cell population versus the S gate for the spore population. No shift in the spore population is seen after treatment with lysozyme in Fig.5.8-a and c. For vegetative *B. atropheus* cells the forward scatter decreases (Fig.5.8-e vs. g) after lysozyme treatment indicating smaller cell sizes or lysis.

Furthermore, the vegetative cells treated with lysozyme shift to the D gate. Comparing both the scatter and fluorescence plots for spores and vegetative cells it is clear that the starting spore suspensions are not affected by lysozyme treatment. The fraction of live spore cells (L/S) after lysozyme treatment is 0.868 ± 0.253 (4 measurements) and 0.020 ± 0.114 (2 measurements) for vegetative cells (L/V) (see Fig. 5.9). These values are statistically unequal with $p > 95\%$. The mean value of L/S for the starting spore suspension and spores treated with lysozyme were statistically equal ($p > 95\%$) which suggests that most of the nebulized cells were indeed spores.

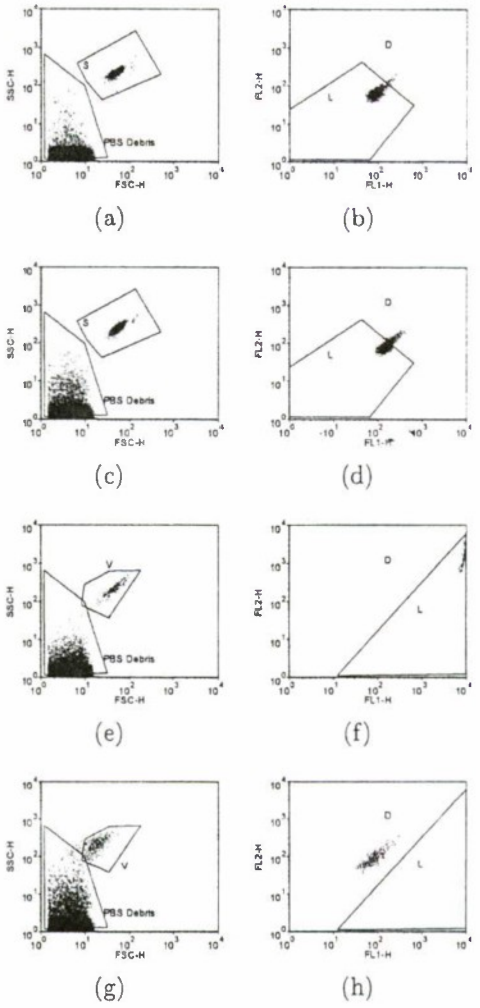

(a) (b)

(c) (d)

(e) (f)

(g) (h)

Figure 5.8: (left) Side-scatter versus forward-scatter plot of all particles in the flow cytometer. The S gate indicates the particle sizes which represent intact spores. The V gate represents the intact vegetative cells. PBS debris indicates the debris population. (right) Red fluorescence (FLH-2) versus green fluorescence (FLH-1) of gated cells in the left side plots. The L gate represents the live cells and the D gate represents the dead cells. (a,b) spore suspension in PBS, (c,d) spore suspension with lysozyme treatment, (e,f) vegetative suspension in PBS and (g,h) vegetative suspension with lysozyme treatment.

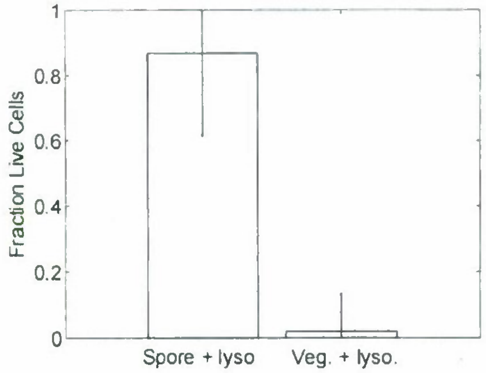

Figure 5.9: Fraction of live cells (L/S) after lysozyme treatment for both spores and vegetative cells. Error bars show the 95% confidence interval using a normal distribution for 4 measurements for spores and 2 measurements for vegetative cells.

5.4.2 Effect of the aerodynamic shock on *B. atropheus* spores

The fraction of cells that remain alive after the effect of impactor operation (f_l) provides a quantitative measure of aerodynamic shock effect when compared to the operation of the impactor under non-critical acceleration conditions. Fluorescence flow cytometry measurements (see Section 5.2.3) and computational particle tracking (see Section 5.3.2) are used to calculate f_l using the following expression [49]:

$$f_l = \frac{n_c}{n'_c} = \frac{n_c}{n_{sl}\phi\eta} \tag{5.11}$$

where n_c is the number of live cells collected after the impactor operation as measured by flow cytometry (see Section 5.4.1) and is equal to the cells in gate L multiplied by the volume of PBS remaining in the collection tube. n'_c is the number of cells live that would be collected if the impactor operation had no effect. n'_c can not be determined from direct measurements because of the aerodynamic shock effect. A mass balance accounting for the losses, shown in Fig. 5.1, has been used where ϕ is the particle loss before the impactor (see Section 5.2.1) and η is the particle collection efficiency (see Section 5.3.2). n'_c becomes $n_{sl}\phi\eta$. n_{sl} is the number of live cells in suspension as measured by flow cytometry (see Section 5.4.1) and is equal to the cells in gate L multiplied by 1 mL (volume of nebulized suspension). The particle losses before the impactor are calculated in Section 5.2.1 and are given as $\phi = 0.088 \pm 0.029$. The collection efficiency (η) for both 0.5 and 1 μm spores in the impactor system is given in Table 5.2. As seen in Fig. 5.10 and Table 5.4, f_l decreases with increasing η (see Remark 13). Both f_l values are calculated and reported in Table 5.4 and Fig. 5.10. A detailed derivation of Eq. 5.11 is shown in our previous work [49].

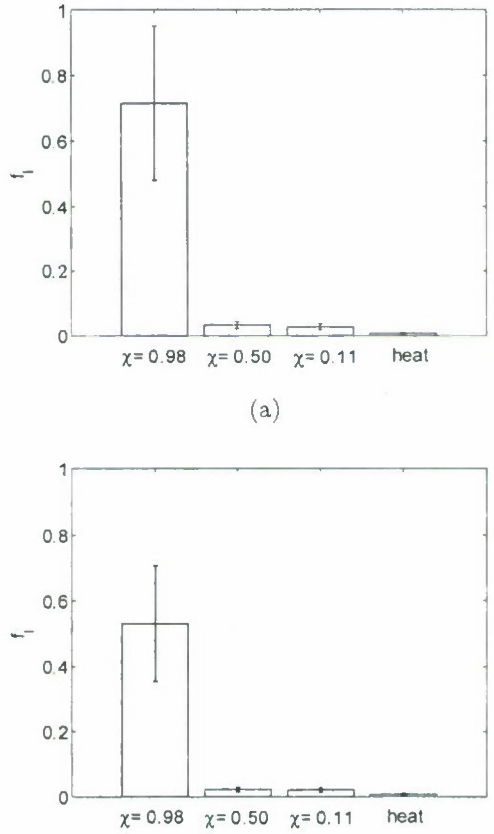

(a)

(b)

Figure 5.10: Fraction of cells that remain alive after the effect of impactor operation (f_l) and after exposure to heat. Live cells in these samples are compared to live cells in the negative control by accounting for losses before the impactor and for the collection efficiency of the impactor for (a) $d_p = 0.5$ μm and (b) $d_p = 1$ μm. Error bars show the 95% confidence interval using a normal distribution for 18 measurements per sample.

The critical acceleration (a_c) for 0.5 and 1 μm spores are 1.6×10^{10} m/s^2 and 3.9×10^9 m/s^2, respectively (see Table 5.3). At $\chi = 0.98$, the maximum computed

Table 5.4: Measured fraction of live cells (L/S) and the fraction of spores surviving the shock (f_l) for both $d_p = 0.5$ and 1 μm. The f_l for the +ve control is not size dependent but is shown under the 0.5 μm column for convenience.

Condition	L/S	$f_l(0.5\mu m)$	$f_l(1\mu m)$
-ve control	0.971 ± 0.012	-	-
$\chi = 0.98$	0.983 ± 0.011	0.715 ± 0.235	0.531 ± 0.176
$\chi = 0.50$	0.895 ± 0.036	0.033 ± 0.011	0.022 ± 0.008
$\chi = 0.11$	0.765 ± 0.082	0.030 ± 0.010	0.020 ± 0.007
+ve control (heat)	0.014 ± 0.006	0.008 ± 0.003	-

acceleration in the experimental impactor is 1.7×10^6 m/s^2 (see Table 5.2). The computed accelerations are three orders of magnitude lower than the critical accelerations required for break-up. The computational results therefore predict that break-up of spores is not achieved under these conditions. Experimental values of f_l for $\chi = 0.98$ closely match the predictions with 0.715 ± 0.235 fraction of the cells surviving the impactor operation. Additionally, for $\chi = 0.11$, where the aerodynamic shock is strongest, spores reach maximum accelerations of 5.9×10^9 m/s^2 and 5.0×10^9 m/s^2 for 0.5 and 1 μm spores, respectively (see Table 5.2). The critical acceleration for 0.5 μm spores is 63% greater (less than an order of magnitude) than the computed accelerations in the impactor. The computations provide insight into the flow structures in the impactor system and are not exact representations of the real fluid flow. Therefore, a 63% difference in value is not significant and is reflected in the experimental f_l values for $\chi = 0.11$ shown in Table 5.4 and Fig. 5.10. The same argument cannot be made for $\chi = 0.50$ where the computed a_{max} is an order of magnitude lower than a_c, yet f_l shows experimental break-up of the cells. As mentioned in Section 5.3.3, the values for surface tensions are calculated either from turgor pressure or contact angle measurements and might not reflect the actual surface tensions under shear conditions. The surface tension values of spores under shear can change the calculated critical accelerations (see Section 5.3.3). However, obtaining these values is outside the scope of this work. Therefore, the computational along with experimental results provide a framework for assessing the effect of the aerodynamic shock on the spores rather than an exact estimate. For both 0.5 and 1 μm cells, f_l at $\chi = 0.11$ is less than f_l at $\chi = 0.50$ with $p > 95\%$. For the non-shock case the f_l is significantly higher. The same trends were observed in Chapter 4 with *E. coli* [49].

As discussed in Section 5.4.1, *B. atropheus* spores that survive break-up in the impactor system and are collected in the deceleration tube are more likely to be alive than *E. coli* vegetative cells ($L/S_{0.11} > L/V_{0.50}$). The data indicates that the spore coat is more resistant to membrane damage if the particle remains intact (see Remark 12). The damage increases as the χ decreases while in vegetative experiments the damage is already at a maximum at $\chi = 0.5$ [49]. In addition, f_l is equal for both $\chi = 0.11$ and $\chi = 0.5$. Although, the same number of cells are breaking up the remaining cells are weaker as the acceleration is higher. Operating the impactor at lower χ (i.e., higher accelerations) can give more insight into the mechanism of break-up for both vegetative cells and spores. We expect f_l values to be lower as cells that currently survive the shock get weaker and break-up.

Remark 12 *The accelerations calculated in Section 5.3.2 are centerline accelera-*

tions. In reality the bacterial particles experience a distribution of accelerations with the maximum at the centerline. For $\chi = 0.5$ *the accelerations away from the centerline can be at values where the spore coat of intact cells is not affected.*

Remark 13 *In order to calculate the exact value for* f_l*, the average collection efficiency has to be calculated from the particle size distribution of the spore suspension. More measurements are required to obtain an accurate size distribution. For example, an aerosol particle size analyzer could be used. However, the focus of this study is to show the range of possible* f_l *values, instead of a very accurate value. This range is sufficient to determine the effect of the aerodynamic shock and comparing the experimental results to computational results.*

5.5 Conclusions

The aerodynamic shock was experimentally shown to cause break-up of *B. atropheus* spores at $\chi = 0.11$ and $\chi = 0.50$. The study provides a framework that yields the parameters needed to guide designs of systems that can neutralize spore aerosols at their release. The computational model predicts the break-up of the spores at $\chi = 0.11$ where accelerations in the aerodynamic shock reach values higher than the a_c ($> 3.9 \times 10^10$ m/s^2). The experimental results confirm the predictions with $f_l = 0.030 \pm 0.010$. The model also predicts the survival of spores at accelerations of 10^6 m/s^2 by operating the impactor at $\chi = 0.98$. This prediction was also confirmed experimentally with $f_l = 0.715 \pm 0.235$ [50]. The critical accelerations were computed using static calculations of surface tension. When surface tension values under shear conditions become available for *B. atropheus* spores, the predictions can be adjusted using the framework provided in this work [49, 51].

Chapter 6

Conclusions of the dissertation

It has been shown, for the first time, that aerodynamic shocks can neutralize vegetative and spore forms of bacterial aerosol. The study provides a theoretical framework to predict the decelerations experienced by a bacterial particle as it passes through an aerodynamic shock. The study considers the break-up of a particle as the mechanism of neutralization which is more stringent than loss of viability or infectivity of a cell. The model predictions can be enhanced by obtaining more accurate surface tension values for cells under fluid flow.

The computational framework developed in Chapters 2 and 3 was validated experimentally using two test bacteria. In Chapter 4, vegetative Gram-negative *E. coli* cells were found to break-up under conditions producing accelerations higher than the critical. In Chapter 5, Gram-positive *B. atropheus* spores were also found to break-up under conditions predicted by the computational model. However, spores had a higher percentage of live cells in the population of cells that did not break-up.

These results can be used in two ways. First, the shock strength of an explosive device can be designed to produce the decelerations needed for bacterial break-up in the context of defense applications. These situations can include the design of explosives that minimize collateral effects of bacterial aerosols in cases where a biological stockpile is being destroyed. Second, nozzles can be designed to avoid the break-up of cells during sampling where the collection of intact live bacteria is needed to perform subsequent analysis.

Bibliography

[1] O. Abouali and G. Ahmadi. A model for supersonic and hypersonic impactors for nanoparticles. *Journal of Nanoparticle Research*, 7(1):75–88, 2005.

[2] F. S. Alvi, J. A. Ladd, and W. W. Bower. Experimental and computational investigation of supersonic impinging jets. *AIAA Journal*, 40(4):599–609, 2002.

[3] M. Berney, F. Hammes, F. Bosshard, H. U. Weilenmann, and T. Egli. Assessment and interpretation of bacterial viability by using the live/dead baclight kit in combination with flow cytometry. *Applied and Environmental Microbiology*, 73(10):3283–3290, 2007.

[4] P. Biswas and R. C. Flagan. The particle trap impactor. *Journal of Aerosol Science*, 19(1):113–121, 1988.

[5] A. Bovallius, B. Bucht, R. Roffey, and P. Anas. Three-year investigation of natural airborne bacterial-flora at four localities in Sweden. *Applied and Environmental Microbiology*, 35(5):847–852, 1978.

[6] W. Burwash, W. Finlay, and E. Matida. Deposition of particles by a confined impinging jet onto a flat surface at Re= 10^4. *Aerosol Science and Technology*, 40(3):147–156, 2006.

[7] S. Chandrasekhar. *Hydrodynamic and Hydromagnetic Stability.* The International Series of Monographs on Physics. Clarendon Press, Oxford, 1^{st} edition, 1961.

[8] G. Chen, A. Driks, K. Tawfiq, M. Mallozzi, and S. Patil. *Bacillus anthracis* and *Bacillus subtilis* spore surface properties and transport. *Colloids and Surfaces B: Biointerfaces*, 76(2):512–518, 2010.

[9] R. Clift, J. R. Grace, and M. E. Weber. *Bubbles, Drops, and Particles.* Academic Press, New York, 1978.

[10] H. J. Conn. The identity of *Bacillus subtilis*. *The Journal of Infectious Diseases*, 46(4):341–350, 1930.

[11] D. E. Cortezzo, K. Koziol-Dube, B. Setlow, and P. Setlow. Treatment with oxidizing agents damages the inner membrane of spores of *Bacillus subtilis* and sensitizes spores to subsequent stress. *Journal of Applied Microbiology*, 97(4):838–852, 2004.

[12] A. K. Datta. *Biological and Bioenvironmental Heat and Mass Transfer.* Marcel Dekker, New York, 2002.

[13] J. F. Delamora, S. V. Hering, N. Rao, and P. H. McMurry. Hypersonic impaction of ultrafine particles. *Journal of Aerosol Science*, 21(2):169–187, 1990.

[14] J. F. Delamora, N. Rao, and P. H. McMurry. Inertial impaction of fine particles at moderate Reynolds-numbers and in the transonic regime with a thin-plate orifice nozzle. *Journal of Aerosol Science*, 21(7):889–909, 1990.

[15] C. Di Giorgio, A. Krempff, H. Guiraud, P. Binder, C. Tiret, and G. Dumenil. Atmospheric pollution by airborne microorganisms in the city of marseilles. *Atmospheric Environment*, 30(1):155–160, 1996.

[16] C. D. Donaldson and R. S. Snedeker. Study of free jet impingement .1. mean properties of free and impinging jets. *Journal of Fluid Mechanics*, 45(2):281–319, 1971.

[17] J.P. Fitch. Review of testing and evaluation methodology for biological point detectors. Technical report, The National Academies Press, 2005.

[18] S. K. Friedlander. *Smoke, Dust, and Haze: Fundamentals of Aerosol Dynamics*. Topics in Chemical Engineering. Oxford University Press, 2^{nd} edition, 2000.

[19] D. Fritze and R. Pukall. Reclassification of bioindicator strains *Bacillus subtilis* dsm 675 and *Bacillus subtilis* dsm 2277 as *Bacillus atrophaeus*. *International Journal of Systematic and Evolutionary Microbiology*, 51:35–37, 2001.

[20] C.R. Harwood and S.M. Cutting. *Molecular Biological Methods for Bacillus.* Modern Microbiological Methods. John Wiley & Sons, Chichester, 1^{st} edition, 1990.

[21] S. V. Hering, R. C. Flagan, and S. K. Friedlander. Design and evaluation of new low-pressure impactor .1. *Environmental Science and Technology*, 12(6):667–673, 1978.

[22] S. V. Hering, S. K. Friedlander, J. J. Collins, and L. W. Richards. Design and evaluation of a new low-pressure impactor .2. *Environmental Science and Technology*, 13(2):184–188, 1979.

[23] W.C. Hinds. *Aerosol technology: properties, behavior and measurement of airborne particles.* John Wiley & Sons, 2^{nd} edition, 1999.

[24] J. O. Hinze. *Turbulence.* McGraw-Hill series in mechanical engineering. McGraw-Hill, New York, 2^{nd} edition, 1975.

[25] G. Horneck, D. Stoffler, U. Eschweiler, and U. Hornemann. Bacterial spores survive simulated meteorite impact. *Icarus*, 149(1):285–290, 2001.

[26] F. P. Incropera and D. P. DeWitt. *Fundamentals of Heat and Mass Transfer.* John Wiley & Sons, 5^{th} edition, 2002.

[27] B. L. Jones and J. T. Cookson. Natural atmospheric microbial conditions in a typical suburban area. *Applied and Environmental Microbiology*, 45(3):919–934, 1983.

[28] D. D. Joseph, J. Belanger, and G. S. Beavers. Breakup of a liquid drop suddenly exposed to a high-speed airstream. *International Journal of Multiphase Flow*, 25(6-7):1263–1303, 1999.

[29] B. J. Jurcik, J. R. Brock, and I. Trachtenberg. A study of low-pressure particle impaction processes. *Journal of Aerosol Science*, 20(6):701–711, 1989.

[30] A. R. Kleinig and A. P. J. Middelberg. The correlation of cell disruption with homogenizer valve pressure gradient determined by computational fluid dynamics. *Chemical Engineering Science*, 51(23):5103–5110, 1996.

[31] A. R. Kleinig and A. P. J. Middelberg. On the mechanism of microbial cell disruption in high-pressure homogenisation. *Chemical Engineering Science*, 53(5):891–898, 1998.

[32] C. Laflamme, S. Lavigne, J. Ho, and C. Duchaine. Assessment of bacterial endospore viability with fluorescent dyes. *Journal of Applied Microbiology*, 96(4):684–692, 2004.

[33] A. I. Laskin and H. A. Lechevalier. *CRC handbook of microbiology*, volume 1. CRC Press, 1974.

[34] M. H. Li and P. D. Christofides. Modeling and analysis of HVOF thermal spray process accounting for powder size distribution. *Chemical Engineering Science*, 58(3-6):849–857, 2003.

[35] M. H. Li and P. D. Christofides. Multi-scale modeling and analysis of an industrial HVOF thermal spray process. *Chemical Engineering Science*, 60(13):3649–3669, 2005.

[36] M. H. Li and P. D. Christofides. Computational study of particle in-flight behavior in the HVOF thermal spray process. *Chemical Engineering Science*, 61(19):6540–6552, 2006.

[37] M. H. Li, D. Shi, and P. D. Christofides. Diamond jet hybrid HVOF thermal spray: Gas-phase and particle behavior modeling and feedback control design. *Industrial and Engineering Chemistry Research*, 43(14):3632–3652, 2004.

[38] H. W. Liepmann and A. Roshko. *Elements of Gasdynamics*. Dover Books on Engineering. Dover Publications, 2001.

[39] B. Lighthart and B. T. Shaffer. Increased airborne bacterial survival as a function of particle content and size. *Aerosol Science and Technology*, 27(3):439–446, 1997.

[40] H. Lundbeck and O. Skoldber. Effect of pressure waves on bacteria suspended in water. *Biotechnology and Bioengineering*, 5(3):167–184, 1963.

[41] R. L. Mancinelli and W. A. Shulls. Airborne bacteria in an urban environment. *Applied and Environmental Microbiology*, 35(6):1095–1101, 1978.

[42] A. Powell. The sound-producing oscillations of round underexpanded jets impinging on normal plates. *Journal of the Acoustical Society of America*, 83(2):515–533, 1988.

[43] W. E. Ranz and W. R. Marshall. Evaporation from drops .1. *Chemical Engineering Progress*, 48(3):141–146, 1952.

[44] W. E. Ranz and W. R. Marshall. Evaporation from drops .2. *Chemical Engineering Progress*, 48(4):173–180, 1952.

[45] S. D. Scroggs and G. S. Settles. An experimental study of supersonic microjets. *Experiments in Fluids*, 21(6):401–409, 1996.

[46] V. Sethi and W. John. Particle impaction patterns from a circular jet. *Aerosol Science and Technology*, 18(1):1–10, 1993.

[47] B. T. Shaffer and B. Lighthart. Survey of culturable airborne bacteria at four diverse locations in Oregon: Urban, rural, forest, and coastal. *Microbial Ecology*, 34(3):167–177, 1997.

[48] A. H. Shapiro. *The Dynamics and Thermodynamics of Compressible Fluid Flow*. The Ronald Press Company, New York, 1953.

[49] P. R. Sislian, D. Pham, X. Zhang, M. Li, L. Mädler, and P. D. Christofides. Bacterial aerosol neutralization by aerodynamic shocks using an impactor system: Experimental results for *E. coli* and analysis. *Chemical Engineering Science*, 65(4):1490–1502, 2010.

[50] P. R. Sislian, J. Rau, X. Zhang, D. Pham, M. Li, L. Mädler, and P. D. Christofides. Bacterial aerosol neutralization by aerodynamic shocks using an impactor system: Experimental results for *B. atropheus* spores. *Chemical Engineering Science*, submitted, 2010.

[51] P. R. Sislian, X. Zhang, M. Li, D. Pham, L. Mädler, and P. D. Christofides. Bacterial aerosol neutralization by aerodynamic shocks using a novel impactor system: Design and computation. *Chemical Engineering Science*, 64(9):1953–1967, 2009.

[52] A. E. Smith, K. E. Moxham, and A. P. J. Middelberg. On uniquely determining cell-wall material properties with the compression experiment. *Chemical Engineering Science*, 53(23):3913–3922, 1998.

[53] S. L. Stewart, S. A. Grinshpun, K. Willeke, S. Terzieva, V. Ulevicius, and J. Donnelly. Effect of impact stress on microbial recovery on an agar surface. *Applied and Environmental Microbioliogy*, 61(4):1232–1239, 1995.

[54] A. L. Stuart and D. A. Wilkening. Degradation of biological weapons agents in the environment: Implications for terrorism response. *Environmental Science &*

Technology, 39(8):2736–2743, 2005.

[55] J. W. Tang. The effect of environmental parameters on the survival of airborne infectious agents. *Journal of the Royal Society Interface*, 6:S737–S746, 2009.

[56] K. Teshima, T. Ohshima, S. Tanaka, and T. Nagai. Biomechanical effects of shock-waves on escherichia-coli and lambda-phage DNA. *Shock Waves*, 4(6):293–297, 1995.

[57] Y. Y. Tong and B. Lighthart. Diurnal distribution of total and culturable atmospheric bacteria at a rural site. *Aerosol Science and Technology*, 30(2):246–254, 1999.

[58] J. Vitko. Sensor systems for biological agent attacks: protecting buildings and military bases. Technical report, The National Academies Press, 2005.

[59] K. Willeke and P. A. Baron. *Aerosol Measurement: Principles, Techniques, and Applications*. Wiley-Interscience, New York, 2001.

[60] Z. Zhang, M. A. Ferenczi, and C. R. Thomas. A micromanipulation technique with a theoretical cell model for determining mechanical-properties of single mammalian-cells. *Chemical Engineering Science*, 47(6):1347–1354, 1992.

[61] P. V. Zinin, J. S. Allen, and V. M. Levin. Mechanical resonances of bacteria cells. *Physical Review E*, 72(6):061907.1–061907.10, 2005.

Appendix B

Fluent and Matlab Codes

The appendix contains sample FLUENT and Matlab codes used to solve the equations in Appendix A.

```
************************ Sample FLUENT code *********************************
; ----------------------
; START OF JOURNAL FILE
; ----------------------
/file/start-transcript "C:\Fluent.Inc\Work\Patrick\Sim004_Two_cases
\P0_0992_P1_0114\transcript1_build_model.trn"
yes
; ================================================================
; STEP 1: Build Model
; ================================================================
; read mesh
; ----------------------
/file/read-case "C:\Fluent.Inc\Work\Patrick\Mesh\nozzle_xd12\xd12_e_v10.msh"
yes
; -----------------------
; Scale
; -----------------------
/grid/scale
0.001
0.001
; -----------------------
; change unit of pressure
; -----------------------
/define/units
```

```
pressure
atm
; -----------------------
; define solver
; -----------------------
/define/models/solver/pressure-based
yes
; -----------------------
; axissymetric
; -----------------------
/define/models/axisymmetric
yes
; -----------------------
; use Green-Gauss Node-Based gradients
; -----------------------
/solve/set/gradient-scheme
yes
; -----------------------
; enable energy equation
; -----------------------
/define/models/energy
yes
no
no
no
yes
; -----------------------
; turbulent model
; -----------------------
/define/models/viscous ke-standard
yes
; -----------------------
; Materials
; -----------------------
/define/materials/change-create air
air
yes
ideal-gas
no
no
yes
sutherland
three-coefficient-method
1.716e-05
273.11
```

```
110.56
no
no
no
no
no
no
; ----------------------------
; operating conditions
; ----------------------------
/define/operating-conditions operating-pressure
0
/define/operating-conditions gravity
no
/define/operating-conditions reference-pressure-location
0
0
; ------------------------
; Boundary conditons
; ------------------------
/define/boundary-conditions/pressure-inlet pressure_inlet.1
no
0.992
no
0.553
no
300
no
yes
no
no
yes
1
1
; --------------------------
; Boundary conditions: outlet
; --------------------------
/define/boundary-conditions/pressure-outlet pressure_outlet.2
no
0.114
no
300
no
yes
yes
```

```
no
1
no
1
no
; --------------------
; Define centerline
; --------------------
/surface/line-surface
centerline
0.062
0
0.0671
0
; ---------------------
; Define Pitot
; ---------------------
/surface/point-surface
pitot
0.0671
0
; ----------------------
; monitor->residual
; ----------------------
/solve/monitors/surface/clear-monitors
/solve/monitors/residual/check-convergence
yes
yes
yes
yes
yes
yes
/solve/monitors/residual/convergence-criteria
0.0001
0.0001
0.0001
1e-6
0.0001
0.0001
/solve/monitors/residual/plot
yes
; ----------------------------
; Set solvers
; ----------------------------
/solve/set/p-v-coupling 1
```

```
/solve/set/under-relaxation/body-force 1
/solve/set/under-relaxation/density 1
/solve/set/under-relaxation/epsilon 0.8
/solve/set/under-relaxation/k 0.8
/solve/set/under-relaxation/mom 0.7
/solve/set/under-relaxation/pressure 0.3
/solve/set/under-relaxation/temperature 1
/solve/set/under-relaxation/turb-viscosity 1
;-----------------------------
; First-order discretization
;-----------------------------
/solve/set/discretization-scheme/density 0
/solve/set/discretization-scheme/epsilon 0
/solve/set/discretization-scheme/k 0
/solve/set/discretization-scheme/mom 0
/solve/set/discretization-scheme/pressure 10
/solve/set/discretization-scheme/temperature 0
/file/write-case "C:\Fluent.Inc\Work\Patrick
  \Sim004_Two_cases\P0_0992_P1_0114\case0.cas"
yes  ; OK to overwrite
/file/stop-transcript
/file/start-transcript "C:\Fluent.Inc\Work\Patrick
  \Sim004_Two_cases\P0_0992_P1_0114\transcript2_ini.trn"
yes
; ==============================================================
; STEP 2: fmg initialization
; ==============================================================
; -----------------------------
; initialize
; -----------------------------
/solve/initialize/compute-default/pressure-inlet pressure_inlet.1
/solve/initialize/initialize-flow
/solve/initialize/set-fmg-initialization
5
0.001
100
0.001
100
0.001
100
0.001
500
0.001
500
0.75
```

```
yes
solve/initialize/fmg-initialization
yes
; ---------------------------------
; Save for debug
; ---------------------------------
wcd "C:\Fluent.Inc\Work\Patrick\Sim004_Two_cases\P0_0992_P1_0114\ini.cas"
yes
/file/stop-transcript
/file/start-transcript "C:\Fluent.Inc\Work\Patrick
  \Sim004_Two_cases\P0_0992_P1_0114\transcript3_F0.trn"
yes
; ============================================================
; STEP 3: Solve flow equation only
; ============================================================
; ---------------------------------
; Disable energy and turbulent equation
; ---------------------------------
/solve/set/equations/ke no
/solve/set/equations/temperature no
; -------------------------------
; iterate 2000 times
; -------------------------------
/solve/iterate 2000
; --------------------------------
; save
; --------------------------------
wcd "C:\Fluent.Inc\Work\Patrick\Sim004_Two_cases\P0_0992_P1_0114\F0.cas"
yes    ; OK to overwrite?
/file/stop-transcript
/file/start-transcript "C:\Fluent.Inc\Work\Patrick
  \Sim004_Two_cases\P0_0992_P1_0114\transcript4_CP_SKE.trn"
yes
; ============================================================
; STEP 4: Solve coupled equations
; ============================================================
; ---------------------------------
; Enable energy and turbulent equation
; ---------------------------------
/solve/set/equations/ke yes
/solve/set/equations/temperature yes
;-----------------------------
; Solve
;-----------------------------
/solve/iterate 2000
```

```
;------------------------------
; Save
;------------------------------
wcd "C:\Fluent.Inc\Work\Patrick\Sim004_Two_cases
  \P0_0992_P1_0114\FO_CP_SKE.cas"
yes    ; OK to overwrite?
/file/stop-transcript
! RD "C:\Fluent.Inc\Work\Patrick\Sim004_Two_cases\P0_0992_P1_0114\SD"
! MD "C:\Fluent.Inc\Work\Patrick\Sim004_Two_cases\P0_0992_P1_0114\SD"
/file/start-transcript "C:\Fluent.Inc\Work\Patrick
  \Sim004_Two_cases\P0_0992_P1_0114\SD\transcript5_SD.trn"
yes
; ==============================================================
; STEP 5: Second-order discretization
; ==============================================================
;-----------------------------
; Second-order discretization
;-----------------------------
/solve/set/discretization-scheme/density 1
/solve/set/discretization-scheme/k 1
/solve/set/discretization-scheme/epsilon 1
/solve/set/discretization-scheme/temperature 1
/solve/set/discretization-scheme/mom 1
/solve/set/discretization-scheme/pressure 12
;-----------------------------
; Change under-relaxation factor
;-----------------------------
/solve/set/under-relaxation/body-force 1
/solve/set/under-relaxation/density 1
/solve/set/under-relaxation/epsilon 0.5
/solve/set/under-relaxation/k 0.5
/solve/set/under-relaxation/mom 0.5
/solve/set/under-relaxation/pressure 0.2
/solve/set/under-relaxation/temperature 1
/solve/set/under-relaxation/turb-viscosity 1
;------------------------------
; Solve
;------------------------------
/solve/iterate 2000
;------------------------------
; Save
; -----------------------------
wcd "C:\Fluent.Inc\Work\Patrick\Sim004_Two_cases
  \P0_0992_P1_0114\SD\FO_CP_SD.cas"
yes    ; OK to overwrite?
```

```
/file/stop-transcript
! RD "C:\Fluent.Inc\Work\Patrick\Sim004_Two_cases\P0_0992_P1_0114\AD1"
! MD "C:\Fluent.Inc\Work\Patrick\Sim004_Two_cases\P0_0992_P1_0114\AD1"
/file/start-transcript "C:\Fluent.Inc\Work\Patrick
  \Sim004_Two_cases\P0_0992_P1_0114\AD1\transcript6_AD1.trn"
yes
; ==============================================================
; STEP 6: ADAPTION
; ==============================================================
; ---------------------------------
; Adaption
; ---------------------------------
/adapt/adapt-to-gradients
pressure
space-gradient
1
no
0.7
0
no
0
0
0
yes
;-----------------------------
; iterate
;-----------------------------
/solve/iterate 2000
;-----------------------------
; Save
;-----------------------------
wcd "C:\Fluent.Inc\Work\Patrick\Sim004_Two_cases
  \P0_0992_P1_0114\AD1\F0_CP_SD_AD1.cas"
yes
/file/stop-transcript
! RD "C:\Fluent.Inc\Work\Patrick\Sim004_Two_cases\P0_0992_P1_0114\AD2"
! MD "C:\Fluent.Inc\Work\Patrick\Sim004_Two_cases\P0_0992_P1_0114\AD2"
/file/start-transcript "C:\Fluent.Inc\Work\Patrick
  \Sim004_Two_cases\P0_0992_P1_0114\AD2\transcript7_AD2.trn"
yes
; ==============================================================
; STEP 7: ADAPTION 2
; ==============================================================
rcd "C:\Fluent.Inc\Work\Patrick\Sim004_Two_cases
  \P0_0992_P1_0114\AD1\F0_CP_SD_AD1.cas"
```

```
; ----------------------------------
; Adaption
; ----------------------------------
/adapt/adapt-to-gradients
pressure
space-gradient
1
no
0.7
0
no
0
0
0
yes
;-----------------------------
; iterate
;-----------------------------
/solve/iterate 2000
;-----------------------------
; Save
;----------------------------
wcd "C:\Fluent.Inc\Work\Patrick\Sim004_Two_cases
  \P0_0992_P1_0114\AD2\FO_CP_SD_AD2.cas"
yes
/file/stop-transcript
! RD "C:\Fluent.Inc\Work\Patrick\Sim004_Two_cases\P0_0992_P1_0114\AD3"
! MD "C:\Fluent.Inc\Work\Patrick\Sim004_Two_cases\P0_0992_P1_0114\AD3"
/file/start-transcript "C:\Fluent.Inc\Work\Patrick
  \Sim004_Two_cases\P0_0992_P1_0114\AD3\transcript8_AD3.trn"
yes
; ==============================================================
; STEP 8: ADAPTION 3
; ==============================================================
rcd "C:\Fluent.Inc\Work\Patrick\Sim004_Two_cases
  \P0_0992_P1_0114\AD2\FO_CP_SD_AD2.cas"
; ----------------------------------
; Adaption
; ----------------------------------
/adapt/adapt-to-gradients
pressure
space-gradient
1
no
0.7
```

```
0
no
0
0
0
yes
;------------------------------
; iterate
;------------------------------
/solve/iterate 2000
;------------------------------
; Save
;-----------------------------
wcd "C:\Fluent.Inc\Work\Patrick\Sim004_Two_cases
  \P0_0992_P1_0114\AD3\FO_CP_SD_AD3.cas"
yes
/file/stop-transcript
; ===============
; Postprocessing
; ===============
; ============================
; Second order discretization
; ============================
; --------------------------------------
; Massflow rate across inlet and outlet
; --------------------------------------
rcd "C:\Fluent.Inc\Work\Patrick\Sim004_Two_cases
  \P0_0992_P1_0114\SD\FO_CP_SD.cas"
/report/fluxes/mass-flow
no
pressure_inlet.1
pressure_outlet.2
()
yes
"C:\Fluent.Inc\Work\Patrick\Sim004_Two_cases
  \P0_0992_P1_0114\SD\massflow_SD.flp"
no
yes
; --------------------------------------
; Maximum mach number along center line
; --------------------------------------
/report/surface-integrals/facet-max
centerline
()
mach-number
```

```
yes
"C:\Fluent.Inc\Work\Patrick\Sim004_Two_cases
  \P0_0992_P1_0114\SD\mach_SD.srp"
no
yes
; ----------------
; Pitot pressure
; ----------------
/report/surface-integrals/facet-avg
pitot
()
pressure
yes
"C:\Fluent.Inc\Work\Patrick\Sim004_Two_cases
  \P0_0992_P1_0114\SD\Pp_SD.srp"
no
yes
; ===========
; Adapt once
; ===========
; --------------------------------------
; Massflow rate across inlet and outlet
; --------------------------------------
rcd "C:\Fluent.Inc\Work\Patrick\Sim004_Two_cases
  \P0_0992_P1_0114\AD1\FO_CP_SD_AD1.cas"
yes
/report/fluxes/mass-flow
no
pressure_inlet.1
pressure_outlet.2
()
yes
"C:\Fluent.Inc\Work\Patrick\Sim004_Two_cases
  \P0_0992_P1_0114\AD1\massflow_AD1.flp"
no
yes
; --------------------------------------
; Maximum mach number along center line
; --------------------------------------
/report/surface-integrals/facet-max
centerline
()
mach-number
yes
"C:\Fluent.Inc\Work\Patrick\Sim004_Two_cases
```

```
  \P0_0992_P1_0114\AD1\mach_AD1.srp"
no
yes
; ---------------
; Pitot pressure
; ---------------
/report/surface-integrals/facet-avg
pitot
()
pressure
yes
"C:\Fluent.Inc\Work\Patrick\Sim004_Two_cases
  \P0_0992_P1_0114\AD1\Pp_AD1.srp"
no
yes
; ============
; Adapt twice
; ============
; -------------------------------------
; Massflow rate across inlet and outlet
; -------------------------------------
rcd "C:\Fluent.Inc\Work\Patrick\Sim004_Two_cases
  \P0_0992_P1_0114\AD2\FO_CP_SD_AD2.cas"
yes
/report/fluxes/mass-flow
no
pressure_inlet.1
pressure_outlet.2
()
yes
"C:\Fluent.Inc\Work\Patrick\Sim004_Two_cases
  \P0_0992_P1_0114\AD2\massflow_AD2.flp"
no
yes
; -------------------------------------
; Maximum mach number along center line
; -------------------------------------
/report/surface-integrals/facet-max
centerline
()
mach-number
yes
"C:\Fluent.Inc\Work\Patrick\Sim004_Two_cases
  \P0_0992_P1_0114\AD2\mach_AD2.srp"
no
```

```
yes
; --------------
; Pitot pressure
; --------------
/report/surface-integrals/facet-avg
pitot
()
pressure
yes
"C:\Fluent.Inc\Work\Patrick\Sim004_Two_cases
  \P0_0992_P1_0114\AD2\Pp_AD2.srp"
no
yes
; ====================
; Adapt the third time
; ====================
; -------------------------------------
; Massflow rate across inlet and outlet
; -------------------------------------
rcd "C:\Fluent.Inc\Work\Patrick\Sim004_Two_cases
  \P0_0992_P1_0114\AD3\F0_CP_SD_AD3.cas"
yes
/report/fluxes/mass-flow
no
pressure_inlet.1
pressure_outlet.2
()
yes
"C:\Fluent.Inc\Work\Patrick\Sim004_Two_cases
  \P0_0992_P1_0114\AD3\massflow_AD3.flp"
no
yes
; -------------------------------------
; Maximum mach number along center line
; -------------------------------------
/report/surface-integrals/facet-max
centerline
()
mach-number
yes
"C:\Fluent.Inc\Work\Patrick\Sim004_Two_cases
  \P0_0992_P1_0114\AD3\mach_AD3.srp"
no
yes
; --------------
```

```
; Pitot pressure
; ---------------
/report/surface-integrals/facet-avg
pitot
()
pressure
yes
"C:\Fluent.Inc\Work\Patrick\Sim004_Two_cases
  \P0_0992_P1_0114\AD3\Pp_AD3.srp"
no
yes

******************** Sample Matlab code ****************************
function [acc,acc_max] = Acceleration(data_g,data_p,interp_method,gap)
% [acc,acc_max] = Acceleration(data_g,data_p,interp_method,gap)
% Calculates maximum acceleration
%
% INPUTS:
%  data_g: returned from ReadGasPhase()
%  data_p: returned from ReadParticle()
%  interp_method: same as interp1(), e.g., 'linear','cubic'.
%  gap: a two-element vector indicating the region in which to search for
%       find maximum acceleration. Unit is meter.
%
%
time = data_p{1};
x_p = data_p{2};
u_p = data_p{5};
x_g = data_g{1};
u_g = data_g{2};

u_g_new = interp1(x_g,u_g,x_p,interp_method);
delta_u = (u_g_new - u_p);

% Acceleration calculation method #1
acc = zeros(length(u_g_new)-1,1);
for i = 1:(length(u_g_new)-1)
    acc(i) = (delta_u(i+1)-delta_u(i))/(time(i+1)-time(i));
end
acc_abs = abs(acc);

% acc_max is the maximum acceleration between the gap
index = (x_p(1:(length(x_p)-1)) > gap(1)) & (x_p(1:(length(x_p)-1)) < gap(2));
acc_max = max(acc_abs(index));
```

Appendix C

Distribution List

1. DTIC-OCP, 8725 John J. Kingman Road Suite 0944, Fort Belvoir, VA 22060-6218, two copies
2. DTRA, ATTN: NTRM, 6200 Meade Road, Ft. Belvoir, VA 22060-5264, one copy
3. DTRA, ATTN: BDCT, 6200 Meade Road, Ft. Belvoir, VA 22060-5264, one copy
4. DTRA, ATTN: BMCI, 6200 Meade Road, Ft. Belvoir, VA 22060-5264, one copy